

THE LUMINESCENCE OF NaI(Tl)

A Thesis
Submitted to
the Faculty of Graduate Studies
University of Manitoba



In Partial Fulfillment
of the Requirements for the Degree
Doctor of Philosophy

by
Roger Palser
February 1969

c1969

TO HELEN

but for whose literary criticism and correction, this thesis
could not have been read, let alone published.

ABSTRACT

An automated experimental system was constructed whereby the excitation and emission spectra of solid luminescent materials may be examined at temperatures between 71°K. and 290°K. The spectral response of the system was determined, and provision made to use a computer to correct luminescent data.

By reference to the absorption spectra of NaI(Tl), the principal excitation and emission bands are associated with the Tl⁺ monomer and (Tl⁺)₂ dimer centres. The A excitation band was found to be not singlet as previously thought, but doublet, with one component attributed to the monomer centre and the other possibly to a monomer centre perturbed by a neighbouring centre. The main emission peak of NaI(Tl) at 2.88 eV (4300 Å) contains in addition to the previously reported monomer and dimer bands, another band which may be associated with the perturbed monomer centre. An emission band at 3.31 eV (3750 Å) and its associated excitation band at 4.56 eV (2720 Å) was found to be unrelated to either of the thallos ion centres, or to a stoichiometric excess of iodine as suggested previously.

The Configurational Coordinate Model was used to determine approximate values for the vibrational frequencies of the ground and excited ³p₁ states of the thallos ion.

The efficiency of luminescence of the dimer centre was

found to be about 100 times that of the monomer centre. A new group of "alloyed dimer" luminescent materials is proposed on the basis of the above observation.

ACKNOWLEDGEMENTS

I wish to thank my supervisor Dr. I. Cooke, and my colleagues C. Watson and I. Rattray for their help during the course of this study. Also I wish to thank Mrs. A. Watson for preparing the final manuscript.

TABLE OF CONTENTS

ABSTRACT.	111
ACKNOWLEDGEMENTS.	v
TABLE OF CONTENTS	vi
CHAPTER	PAGE
I. BASIC CONCEPTS.	1
A. Introduction.	1
B. Transition Probability.	3
C. Electric Dipole Transitions	4
D. Absorption Cross Section.	6
E. Effect of the Host Material on the Luminescent Centre.	6
II. APPROXIMATIONS PERTINENT TO THE THEORY OF CENTRES	9
A. The Hartree-Fock Approximation.	9
B. The Rigid Lattice	9
C. The Vibrating Lattice	10
(1) The Born Oppenheimer or Adiabatic Approximation	10
(2) The Condon Approximation.	14
D. Comparison of the Rigid and Vibrating Lattice Models.	15
III. THE THEORY OF IDEALIZED CENTRES	17
A. The Harmonic or Linear Approximation.	17
B. The Tight Binding Approximation	24

CHAPTER	PAGE
C. The Franck-Condon Principle	29
D. Calculation of the Configurational Coordinate Diagram.	34
E. Construction of the Configurational Coordinate Diagram from Experimental Data.	36
F. Assignment of the Electronic States . .	39
IV. DATA ASSIMILATION AND CORRECTION.	46
A. Experimental Apparatus.	46
(1) Mechanical Equipment.	46
(2) Electronic Equipment.	47
B. Sample Preparation.	52
C. Experimental Procedure.	53
D. Data Correction	54
(1) Spectral Response Correction. . .	54
(2) Slit Width Correction	62
(3) Temperature Determination	64
V. EXPERIMENTAL DATA AND THEIR INTERPRETATION. .	65
A. Introduction.	65
B. Low Temperature Excitation Spectra. . .	66
C. Low Temperature Excitation Envelope Shapes.	79
D. Room Temperature Excitation Spectra . .	93
E. Room Temperature Excitation Envelope Shapes.	98

CHAPTER	PAGE
F. Temperature Dependence of the Excitation Envelopes.	106
G. Low Temperature Emission Spectra.	110
H. Low Temperature Emission Envelope Shapes.	126
I. Room Temperature Emission Spectra	139
J. Temperature Dependence of the Emission Envelopes	144
VI. CURVE FITTING	166
A. Introduction.	166
B. The Gaussian Fitting Program.	167
C. Fits to the Experimental Data	171
(1) Pure Gaussian Fits.	172
(2) Distorted Gaussian Fits	182
VII. CONCLUSIONS	187
A. General Conclusions	187
B. The Monomer Centre.	188
C. The Dimer Centre.	189
D. Additional Observations	190
REFERENCES.	191

CHAPTER I

BASIC CONCEPTS

(A) Introduction

A consistent quantum mechanical treatment of the interaction between material particles and an electromagnetic field requires as its basis the determination of the quantum equation of motion of each particle in the field. These equations would be analogous to Maxwell's Equations, which characterize the classical theory. The complexity of the treatment is commonly reduced by approximating the real interaction by one between a particle interacting quantum mechanically with a classical electromagnetic field. Such an approximation is justified (Messiah, 1966) when the total energy transfer between the particles and the radiation field is so large compared to the absorbed or emitted photon energy that the discontinuous nature of the transfer can be ignored. Equivalently, the approximation is valid for high absorption or emission intensities at low frequencies and is particularly suited to problems involving a particle in a static electromagnetic field, or one of known time dependence.

In particular, for an electron interacting with an incident radiation field, the Schrödinger wave equation describing the motion of the electron is, with conventional notation:-

$$i\hbar \frac{\partial \psi}{\partial t} = \left[\frac{-\hbar^2}{2m} \nabla^2 + \frac{ie\hbar}{mc} \mathbf{A} \cdot \text{grad} + \frac{ie\hbar}{2mc} \{\text{div } \mathbf{A}\} + \frac{e^2}{2mc^2} \mathbf{A}^2 + e\phi + V(r) \right] \psi \quad 1.1$$

where $V(r)$ is the interaction potential between the electron and its local environment: \mathbf{A} and ϕ represent the vector and scalar potentials describing the electromagnetic field.

The time dependent electron wavefunction $\psi(t)$ may be expanded in terms of a linear combination of a complete set of orthonormal eigenfunctions $\{U_n\}$ belonging to the set of eigenvalues $\{E_n\}$, setting

$$\psi(t) = \sum_n a_n(t) U_n e^{iE_n t/\hbar} \quad 1.2$$

where $\{a_n\}$ represents a set of coefficients or amplitudes.

By using time dependent perturbation theory, the set of coefficients $\{a_n\}$ may be determined, yielding:-

$$a_k(t) = \frac{e}{imc} \left[C_{km}^+ \frac{e^{i\{\omega_{km} - \omega\}t-1}}{\{\omega_{km} - \omega\}} + C_{km}^- \frac{e^{i\{\omega_{km} + \omega\}t-1}}{\{\omega_{km} + \omega\}} \right] \quad 1.3$$

where C_{km}^{\pm} are matrix elements of the gradient operator defined by:-

$$C_{km}^+ = \left(U_k \left| e^{i\mathbf{r} \cdot \mathbf{L}} \mathbf{A}_0 \cdot \nabla \right| U_m \right) \quad 1.4$$

$$C_{km}^- = \left(U_k \left| e^{-i\mathbf{r} \cdot \mathbf{L}} \mathbf{A}_0^* \cdot \nabla \right| U_m \right)$$

and

$$\omega_{km} = \{E_k - E_m\}/\hbar$$

ω is the angular frequency of the incident radiation field, \mathbf{A}_0 the polarization vector, and \mathbf{p} the propagation vector.

(B) Transition Probability

The probability of a transition from state m to state k ($m \rightarrow k$) within the time t is:

$$|a_{km}(t)|^2$$

and from Equation I.3 the transition probability is appreciable only when the denominator of either of the terms approaches zero. If $E > E_m$, large transition probabilities occur only when $E_k \approx E_m + \hbar\omega$. The first term of Equation I.3 may then be interpreted as an absorption of one quantum of energy, $\hbar\omega_{km}$, from the radiation field. Similarly the downward transition $k \rightarrow m$ is associated with the induced emission of one quantum whose frequency corresponds to that of the monochromatic radiation field.

Because of its energy dependence, the transition probability is independent of time only if the final state involved in the transition is one of a continuously distributed or very closely spaced group (Schiff, 1955). However, transitions between discrete states are of importance to optical studies and computation of the associated transition probability is desirable. For such cases, if the incident radiation is strictly monochromatic, the transition probability

per unit time is not constant but depends markedly upon the difference between ω and ω_{km} . In order to develop the theory further the assumption is made that the incident radiation field covers a range of frequencies, as in practice it usually does, and that there may be associated with the field an intensity per unit frequency range that is constant in the neighbourhood of ω_{km} (Heitler, 1954).

If the intensity in the small angular frequency range $\Delta\omega$ is $I[\omega]\Delta\omega$, then the probability of a transition that leaves the electron in a higher energy state is, from Equation I.4 :-

$$|a_k(t)|^2 = \sum_{\omega} \left(\frac{e}{mc}\right)^2 |C_{km}^+|^2 \left| \frac{e^{i\{\omega_{km}-\omega\}t-1}}{\{\omega_{km}-\omega\}} \right|^2 \quad 1.5$$

The above summation may be replaced by an integral (Schiff, 1955), and the probability per unit time (W_{km}) for both absorptive and emissive transitions may then be written as:-

$$W_{km} = \frac{4\pi^2 e^2}{m^2 c \omega_{km}^2} I[\omega_{km}] \left| \left(U_k \left| e^{i\rho \cdot \mathbf{r}} \text{grad}_A \right| U_m \right) \right|^2 \quad 1.6$$

where grad_A is the component of the gradient operator along the polarization vector A_0 .

(C) Electric Dipole Transitions

A further approximation in Equation I.6 is possible for localized atoms or centres interacting with ultraviolet

or longer wavelength radiation. Such a localized centre has a linear dimension of only a few Angstrom units so that the term $e^{i\mathbf{p}\cdot\mathbf{r}}$ may be approximated by unity. Thus the exponential may be expanded as a power series, resulting in the reduction of Equation 1.6 to :-

$$W_{km} = \frac{4\pi^2 e^2}{3\hbar c} I[\omega_{km}] |r_{km}|^2 \quad 1.7$$

where r_{km} is the mean component of the particle electric dipole moment in the direction of polarization.

The "Einstein B Coefficient" (Schiff, 1955) for induced absorption or emission is the transition probability per unit time per unit energy density, whilst the spontaneous emission probability, $1/\tau$, usually called the "Einstein A Coefficient", is given below.

$$\left(\frac{1}{\tau}\right)_{km} = \frac{4e^2 \omega_{km}^3}{3\hbar c^3} |r_{km}|^2 \quad 1.8$$

Assuming, as before, that transitions occur to one of a continuous or closely spaced set of states, the spontaneous emission probability may be written as a function of energy in the form:-

$$\omega_{km}[E] = \left(\frac{1}{\tau}\right)_{km} F_{km}^e[E] = \frac{4e^2 E_{km}^3}{3\hbar^4 c^3} |r_{km}|^2 F_{km}^e[E] \quad 1.9$$

where $F_{km}[E]$ is a narrow function of energy normalized so that

$$\int F_{km}^e[E] dE = 1$$

1.10

(D) Absorption Cross Section

The absorption cross section $\left(\sum_{m \rightarrow k}\right)$ for a given transition is defined as the energy absorbed per unit time for an incident energy flux corresponding to one photon per unit volume. Thus the total cross section integrated over the absorption line width follows from Equation 1.7 and is:-

$$\sum_{m \rightarrow k} = \frac{4\pi^2 e^2}{3c} \omega_{km} |r_{km}|^2$$

1.11

and the absorption coefficient $\left(\sigma_{mk}[E]\right)$ at a particular energy E is:-

$$\sigma_{mk}[E] = F_{mk}^a[E] \sum_{m \rightarrow k} = \frac{4\pi^2 e^2}{3\hbar c} E_{km} |r_{km}|^2 F_{mk}^a[E]$$

1.12

where $F_{mk}^a[E]$ is the absorption line shape function normalized so that:-

$$\int F_{mk}^a[E] dE = 1$$

1.13

(E) Effect of the Host Material on the Luminescent Centre

The optical properties of solid luminescent materials are characteristic not of isolated atomic systems, as treated in the previous section, but of centres embedded within a dielectric medium. The presence of the host material

necessitates certain theoretical modifications, which take a manageable form when the following conditions prevail:-

a) The concentration of luminescent centres within the host is sufficiently low that interactions between the centres may be neglected.

b) The transitions within the centre occur at energies far removed from those at which transitions occur within the host crystal. That is, the centre does not resonate with the lattice.

In general the modifications imposed upon the energy levels and wavefunctions of the isolated centre are determined by the structure and material of the host. However, Lax (1952) has shown that within the above approximations, the host dielectric medium may be characterized by its refractive index, effective field at the centre, and effective mass for charge carriers. Following his treatment, the effect of the host upon the optical properties of the luminescent centre may be represented by additional factors in the expressions for the absorption coefficient and the spontaneous emission probability. Equations I.9 and I.12 then become:-

$$\omega_{km}[E] = \left[\left(\frac{\epsilon_e}{\epsilon_o} \right)^2 n \right] \frac{4e^2}{3\hbar^4 c^3} E_{km}^3 |r_{km}|^2 F_{km}^e [E] \quad 1.14$$

and

$$\sigma_{mk}[E] = \left[\left(\frac{\epsilon_e}{\epsilon_o} \right)^2 \frac{1}{n} \right] \frac{4\pi^2 e^2}{3\hbar c} E_{km} |r_{km}|^2 F_{mk}^a [E] \quad 1.15$$

where ϵ_e is the effective field inducing the transition, ϵ_0 the average field in the dielectric medium, and n the real part of the refractive index (Brillouin, 1932).

These equations, then, together with the electronic wavefunctions and energy levels, define the optical processes characteristic of a luminescent centre surrounded by a dielectric medium. Their utilization to compute the experimentally observed optical phenomena, such as band positions, shapes and intensities, temperature and pressure dependencies, etc., of a particular material, requires the adoption of further approximations suited to the material in question. The following chapter will review this topic in more detail.

CHAPTER II

APPROXIMATIONS PERTINENT TO THE THEORY OF CENTRES

(A) The Hartree-Fock Approximation

In most atomic systems, and almost invariably in solid state physics, it is necessary to approximate the wavefunction $U(r_1, r_2, \dots, r_n)$ describing a state involving many electrons by a product wavefunction of the form $\psi_1(r_1) \psi_2(r_2) \dots \psi_n(r_n)$ where $\psi_i(r_i)$ is dependent upon the coordinates of only one electron. The Pauli exclusion principle is violated in the Hartree simplification, but this may be corrected by the use of the antisymmetric Slater-Fock determinant:-

$$U(r_1, r_2, \dots, r_n) = [N!]^{-1/2} \begin{vmatrix} \psi_1(r_1) & \dots & \psi_1(r_n) \\ \vdots & & \vdots \\ \psi_n(r_1) & \dots & \psi_n(r_n) \end{vmatrix} \quad \text{II.1}$$

where the coordinate (r_i) includes both spin and space components. The one electron approximation is discussed in detail by Reitz (1955).

(B) The Rigid Lattice

The rigid or static lattice model assumes that the optical phenomena characteristic of the isolated impurity centres result from transitions between the energy levels of electrons in a fixed potential field generated by the rigid lattice. Knowing the fixed potential, the electronic

wavefunctions and energy levels may be computed, together with the matrix elements leading to Equations I.14 and I.15. Thus an almost complete description of the optical process can be obtained, provided realistic values of the effective field ratio (Dexter, 1956; Dexter, 1956a; McClure, 1959; Herzfeld, 1961), refractive index (Dexter, 1956a), and effective mass (Lax, 1956; Dexter et al., 1956) are available.

(C) The Vibrating Lattice

In the previous section, the impurity centre wavefunctions were dependent upon the electron coordinates (r), with no consideration being given to the coordinates of the lattice. Such an omission is clearly unrealistic; but on the other hand the Schrödinger equation for a system whose wavefunction involves the electron coordinates (r) and possibly a large number of lattice coordinates (x) is too difficult to solve. The development of the following approximations paved the way for further theoretical advance.

(1) The Born-Oppenheimer or Adiabatic Approximation

The Born-Oppenheimer approximation (Born and Oppenheimer, 1927; Seitz, 1940; Goldberg, 1966) has its basis in the fact that the period of orbital electronic motion is usually short compared with the period of lattice vibrations. Thus there exist stationary electronic states, described by the many electron wavefunctions $\phi(r)$ that are functions only

of the electronic coordinates (r), and these states will be smoothly or adiabatically deformed by the displacements of the nuclei from their equilibrium positions. Thus the total wavefunction $U_k(r, X)$ may be written as a product function in the form:-

$$U_k(r, X) = \phi_{bX}(r) \Pi_{\beta b}(X) \quad 11.2$$

where the electronic wavefunction $\phi(r)$ is parametrically dependent on the instantaneous positions (X) of the nuclei. The nuclear wavefunction $\Pi(X)$ depends parametrically on the electronic state (b), but not on the positions of the electrons. The quantum numbers labelling the electronic and nuclear states are respectively b and β .

The adiabatic approximation would appear to be valid provided:-

$$\frac{\hbar \omega}{E_b - E_a} \ll 1 \quad 11.3$$

However, Herring (1956) gives a somewhat more precise condition, namely

$$\frac{\hbar \omega}{E_b - E_a} \frac{\Delta X}{(\Delta X)'} \ll 1 \quad 11.4$$

where ΔX is the lattice vibrational amplitude, and $(\Delta X)'$ the nuclear displacement necessary to produce a significant change in the electronic wavefunction. On the basis of this

criterion, the adiabatic approximation is valid (Dexter, 1956a; Goldberg, 1966) for most inorganic semiconductors and localized impurity centres, wherein the electronic states for visible and ultraviolet transitions are not too closely spaced. The violation of this approximation increases the probability of non-radiative transitions.

The transitions involved in the basic Equations I.14 and I.15 may now be re-examined and divided into the following categories:

(a) Transitions involving the nuclear wavefunctions only are not of interest here since they exclude the impurity centre.

(b) Transitions that involve only the electronic wavefunctions occur mainly in organic and rare earth materials, and will not be discussed further.

(c) Transitions in which both the nuclear and the electronic wavefunctions change are of principal concern here since they occur in the alkali halides.

In this more general case, each given electronic transition ($\alpha \leftrightarrow \beta$) will have an associated vibrational spectrum involving transitions ($\alpha \leftrightarrow \beta$) between pairs of vibrational states, each line within the vibrational spectrum having a Lorentzian distribution (Dexter, 1956a). The basic Equations I.14 and I.15 are still valid, but with the quantum numbers (m) and (k) generalized to include both electronic

and nuclear states. In an absorptive transition between two electronic states at absolute zero, a sum must be performed over the vibrational levels associated with the excited electronic state. At elevated temperatures, in addition to the summation over the final vibrational states, an appropriate thermal average must be performed over the population of vibrational levels in the initial electronic state.

The basic low temperature Equations I.14 and I.15 are thus modified, and using $A_{v\alpha}$ and $A_{v\beta}$ to denote statistical averages over the initially occupied vibrational states, become:-

$$\sigma_{ab}[E] = \left[\left(\frac{\epsilon_e}{\epsilon_o} \right)^2 \frac{1}{n} \frac{4\pi^2 e^2}{3\hbar c} A_{v\alpha} \sum_{\beta} |E_{ab\alpha\beta}|^2 |r_{ab\alpha\beta}|^2 F_{ab\alpha\beta}^a [E] \right] \quad 11.5$$

and

$$\omega_{ba}[E] = \left[\left(\frac{\epsilon_e}{\epsilon_o} \right)^2 \frac{1}{n} \frac{4e^2}{3h^4 c^3} A_{v\beta} \sum_{\alpha} |E_{ba\beta\alpha}|^3 |r_{ba\beta\alpha}|^2 F_{ba\beta\alpha}^e [E] \right] \quad 11.6$$

where the matrix element $r_{ab\alpha\beta}$ is defined as:-

$$r_{ab\alpha\beta} = \iint \Pi_{\alpha\alpha}^*(X) \phi_{\alpha\alpha}^*(r) |r| \Pi_{\beta\beta}(X) \phi_{\beta\beta}(r) dX dr \quad 11.7$$

Normally the many vibrational lines underlying an electronic transition are unresolved, resulting in the broad absorption and emission spectra characteristic of luminescence from impurity centres. In such cases the shape functions

$F_{ab\alpha\beta}^a$ and $F_{ba\beta\alpha}^e$ may be replaced by the delta functions:-

$$\delta \{ E_{b\beta} - E_{a\alpha} - E \}$$

It is, however, sometimes possible to observe the vibrational

spectrum underlying an absorption or emission band. This phenomenon will be considered later.

(2) The Condon Approximation

Using the Born approximation, the dipole matrix element of Equation II.7 may be rewritten in the form:-

$$r_{ab\alpha\beta} = \int \Pi_{\alpha\alpha}^*(X) \Pi_{b\beta}(X) r_{ab}(X) dX \quad \text{II.8}$$

where

$$r_{ab}(X) = \int \phi_{\alpha\alpha}^*(r) |r| \phi_{b\beta}(r) dr \quad \text{II.9}$$

The electronic wavefunctions $\phi_{\alpha\alpha}(r)$ depend parametrically upon the nuclear coordinates and result in the matrix element $r_{ab}(X)$ being a function of X . The Condon approximation ignores this dependence or in a refined approximation substitutes an appropriate average over the nuclear coordinates. This result can also be obtained from the Born-Oppenheimer approximation, if at Equation II.2 the parametric dependence of the electronic wavefunction upon the nuclear coordinates is neglected.

Thus the square of the dipole matrix elements for absorption and emission become:-

$$\left| r_{ab\alpha\beta} \right|^2 = \langle |r_{ab}|^2 \rangle_{Av} \left| \int \Pi_{\alpha\alpha}^*(X) \Pi_{b\beta}(X) dX \right|^2 \quad \text{II.10}$$

$$\left| r_{ba\beta\alpha} \right|^2 = \langle |r_{ba}|^2 \rangle_{Av} \left| \int \Pi_{b\beta}^*(X) \Pi_{\alpha\alpha}(X) dX \right|^2 \quad \text{II.11}$$

In general the Condon average for an absorptive transition will differ from that for an emissive one, since different

sets of nuclear coordinates are involved in each transition. Further, the relevant nuclear coordinates depend upon the particular vibrational states α and β involved, so that a suitable mean must be taken over the vibrational spectrum also.

In spite of its almost universal practical use, the Condon approximation has suffered little scrutiny. Dexter (1954), however, calculated that for a well localized centre, the Condon approximation depresses the low energy side relative to the high energy side of the emission band, probably by something less than ten percent, and vice versa for the absorption band.

(D) Comparison of the Rigid and Vibrating Lattice Models

The previous discussion has emphasized and perhaps lent more credibility to the adiabatic approximation at the expense of the static one. This bias is justified in the present context since it leads rather elegantly to the configurational coordinate model, the basis of this thesis.

Unfortunately, some of the literature in the alkali halide field proliferates this bias to the extent of regarding the adiabatic approximation as "exact" or at least superior to the static (Lax, 1956). With the exception of a book by Born and Huang (1954) there appears little to justify this apparent superiority, especially in view of papers by Frenkel (1932) and Markham (1954) which indicate that the

adiabatic approach is merely an alternate approximation, not necessarily superior. Markham (1956) compared the two approximations by means of the variational principle, and concluded that the static approach overestimates the potential energy and underestimates the kinetic energy associated with the lattice, whilst the adiabatic approximation does exactly the opposite.

CHAPTER III

THE THEORY OF IDEALIZED CENTRES

Returning to a central theme of the theoretical discussion, the prediction of the experimentally observed absorption and emission band shapes is characterized by Equations II.5 and II.6, which both involve the shape factors F . Even if the approximations of the previous chapter are made, the band shape calculation is still such a formidable task that once more recourse has to be made to a specific simplified model of the luminescent centre. The "diffuse" and "well localized" models are involved, resulting in the following treatments:

(A) The Harmonic or Linear Approximation

The linear approximation, usually used in conjunction with the diffuse model, assumes that electron wavefunctions and energy levels of the centre in a static undeformed lattice are available (Wannier, 1937) for use in a perturbation calculation. In order to use a perturbation technique, a weak interaction between the centre and the lattice ions is mandatory, and the harmonic approximation requires that the interaction energy be linear in the displacements of the ions from their equilibrium positions. The development of this model by Huang and Rhys (1950), Lax (1952), O'Rourke (1953) and Pekar (1953) is outlined below.

In the static approximation, the lattice may be regarded as a set of N independent harmonic oscillators all of the same frequency. The system may then be characterized in suitable units by a Hamiltonian of the form:-

$$H^{ab} = \frac{1}{2} \sum_{j=1}^N \left[\dot{X}_j^2 + \{\omega_j^{ab}\}^2 X_j^2 \right] \quad \text{III.1}$$

with harmonic wavefunctions:-

$$\phi_j^a(X_j) \quad \text{and} \quad \phi_j^b(X_j)$$

for which the energy levels are:-

$$E^a = \{n_j^a + 1/2\} \hbar \omega_j^a \quad \text{and} \quad E^b = \{n_j^b + 1/2\} \hbar \omega_j^b$$

with a and b denoting the ground and excited electronic states respectively. In general the wavefunctions of the vibrational states can be expanded in terms of the Born-Oppenheimer approximation according to the previous chapter.

The interaction Hamiltonian, dictated by the linear approximation, becomes:-

$$H_{int}^{ab} = \frac{1}{\sqrt{N}} \sum_{j=1}^N A_j X_j \quad \text{III.2}$$

where A_j is the coupling constant between the centre and the lattice for the electronic transition $a \rightarrow b$.

By making the following linear transformation upon the normal lattice coordinates X_j the system may be reduced once again to a set of oscillators.

$$X_j^{ab} \rightarrow X_j - \frac{1}{\sqrt{N}} \{\omega_j^{ab}\}^{-2} A_j \quad \text{III.3}$$

Then the total Hamiltonian becomes:-

$$(H + H_{int}^{ab}) = \frac{1}{2} \sum_{j=1}^N \left[\left\{ \dot{X}_j^{ab} \right\}^2 + \left\{ w_j^{ab} \right\}^2 \left\{ X_j^{ab} \right\}^2 - \frac{1}{N} \left\{ w_j^{ab} \right\}^{-2} A_j^2 \right] \quad \text{III.4}$$

and the right hand term, being independent of the nuclear coordinates, represents a relative shift in the energy levels resulting from the interaction. Thus the electronic transition energy becomes:-

$$(E_{ab})' = E_{ab} - \frac{1}{2N} \sum_{j=1}^N \left\{ w_j^{ab} \right\}^{-2} A_j^2 \quad \text{III.5}$$

with

$$\hbar \omega_{ba} = E_b' - E_a'$$

Recalling Equations II.5 and II.6, the absorption coefficient and spontaneous emission probability are given by:-

$$\sigma_{ab}[E] = \left[\left(\frac{\epsilon_e}{\epsilon_o} \right)^2 \frac{1}{n} \right] \frac{4\pi^2 e^2}{3\hbar c} A_{v\alpha} \sum_{\beta} \left| E_{ab\alpha\beta} \right| \left| r_{ab\alpha\beta} \right|^2 F_{ab\alpha\beta}^a(E)$$

and

$$\omega_{ba}[E] = \left[\left(\frac{\epsilon_e}{\epsilon_o} \right)^2 \frac{1}{n} \right] \frac{4e^2}{3\hbar^4 c^3} A_{v\beta} \sum_{\alpha} \left| E_{ba\beta\alpha} \right| \left| r_{ba\beta\alpha} \right|^2 F_{ba\beta\alpha}^e(E)$$

Certain terms within these equations may now be simplified further by application of previously discussed approximations, and the limitations of the present model.

(1) The Condon approximation is invoked to average over the vibrational states, replacing elements of the form:-

$$\left| r_{ab\alpha\beta} \right|^2 \text{ by } \left\langle \left| r_{ab} \right| \right\rangle A_v \left| \int \Pi_{a\alpha}^*(X) \Pi_{b\beta}(X) dX \right|^2 \quad \text{III.6}$$

according to Equations II.10 and II.11. In addition, the energy terms of Equations II.5 and II.6, $|E_{ab\alpha\beta}|$ and $|E_{ba\beta\alpha}|$, are replaced by suitable averages, $\langle |E_{ab}| \rangle$ and $\langle |E_{ba}| \rangle$, assuming that the variation of E over the absorption and emission bands is small compared with the average value. This, the so-called "narrow band approximation", is clearly not a good approximation, but is reasonable in view of the lack of a functional dependence between $|r_{ab}|$ and the nuclear coordinates.

(2) The shape functions $F^a(E)$ and $F^e(E)$ are replaced by Dirac delta functions expressed in the integral representation of Lax (1952):-

$$F(E) = \delta\{E_{b\beta} - E_{a\alpha} - E\} = \frac{1}{2\pi\hbar} \int_{-\infty}^{\infty} e^{\frac{it}{\hbar}\{E_{b\beta} - E_{a\alpha} - E\}} dt \quad \text{III.7}$$

where $\{E_{b\beta} - E_{a\alpha}\}$, determined from the oscillator energy levels, is:-

$$\{E_{b\beta} - E_{a\alpha}\} = \hbar\omega_{ba} + \sum_{j=1}^N \left[\left\{ n_j^b + \frac{1}{2} \right\} \hbar\omega_j^b - \left\{ n_j^a + \frac{1}{2} \right\} \hbar\omega_j^a \right] \quad \text{III.8}$$

In general $E_{ab} > \hbar\omega_{ba} > E_{ba}$ and the difference between E_{ab} and E_{ba} is commonly called the Stokes' shift.

Thus substitution of III.6, III.7, and III.8 into II.5 and II.6 gives:-

$$\sigma_{ab}[E] = \left[\left(\frac{\epsilon_e}{\epsilon_o} \right)^2 \frac{1}{n} \right] \frac{4\pi^2 e^2}{3\hbar c} \langle |r_{ab}|^2 \rangle_{Av} \langle |E_{ab}| \rangle_{Av} I_{ab}[E] \quad \text{III.9}$$

and

$$\omega_{ba}[E] = \left[\left(\frac{\epsilon_e}{\epsilon_o} \right)^2 n \right] \frac{4e^2}{3\hbar^4 c^3} \langle |r_{ba}|^2 \rangle_{Av} \langle |E_{ba}|^3 \rangle_{Av} I_{ba}[E] \quad \text{III.10}$$

where I_{ab} and I_{ba} are the normalized absorption and emission band shapes given by:-

$$I_{ab}[E] = \frac{1}{2\pi\hbar} A_{\nu\alpha} \sum_{\beta} \int_{-\infty}^{\infty} dt e^{\frac{it}{\hbar} \{E_{b\beta} - E_{a\alpha} - E\}} \left| \int \Pi_{a\alpha}^*(X) \Pi_{b\beta}(X) dX \right|^2 \quad \text{III.11}$$

and

$$I_{ba}[E] = \frac{1}{2\pi\hbar} A_{\nu\beta} \sum_{\alpha} \int_{-\infty}^{\infty} dt e^{\frac{it}{\hbar} \{E_{b\beta} - E_{a\alpha} - E\}} \left| \int \Pi_{b\beta}^*(X) \Pi_{a\alpha}(X) dX \right|^2 \quad \text{III.12}$$

The major shape dependence results from the square of the vibrational overlap integral, which may be evaluated explicitly since each vibrational wavefunction is a product of the harmonic oscillator wavefunctions:-

$$\Pi_{a\alpha}(X) = \prod_{j=1}^N \phi_{j\alpha}^a(X_j) \quad \text{III.13}$$

where α defines the quantum state of the j -th oscillator mode.

The band shapes, given in Equations III.11 and III.12, have been evaluated (O'Rourke, 1953) and may be expressed in the form:-

$$I_{ab}[E] = \frac{1}{2\pi\hbar} \int_{-\infty}^{\infty} \left\{ e^{i[w_{ba} - \omega]t} e^{\frac{it}{2} \left[\sum_{j=1}^N \{w_j^b - w_j^a\} \text{Coth}\{\hbar\omega_j^a/2kT\} \right]} \right. \\ \left. \times e^{\left[\sum_{j=1}^N \frac{w_j^a}{\hbar N} \frac{\{A_j^b/(\omega_j^b)^2 - A_j^a/(\omega_j^a)^2\}}{\{\text{Coth}^{-1}\frac{t}{2}w_j^b + \text{Coth}\frac{1}{2}(\hbar\omega_j^a/kT + i\omega_j^a t)\}} \right]} \right\} dt \quad \text{III.14}$$

together with a similar equation for the emission band shape. By assuming that the vibrational wavefunctions have identical form in both the excited and ground states, (i.e. $\omega_j^a = \omega_j^b = \bar{\omega} = \text{constant}$), Huang and Rhys (1950) and Pekar (1953) were able to simplify Equation III.14 further and express the absorption coefficient of Equation III.9 in the form:-

$$\sigma[\hbar\omega_{ba} - \hbar\bar{\omega}p] = \left[\left(\frac{\epsilon_e}{\epsilon_0} \right)^2 \frac{1}{n} \right] \frac{4\pi^2 e^2}{3\hbar c} \langle |r_{ab}|^2 \rangle_{Av} \langle |E_{ab}| \rangle_{Av} \frac{1}{\hbar\bar{\omega}} \left[\frac{\langle n \rangle + 1}{\langle n \rangle} \right]^{p/2} \\ \times e^{-S(2\langle n \rangle + 1)} \sum_{\xi=-\infty}^{\infty} \delta\{\xi - p\} I_p \left\{ 2S[\langle n \rangle(\langle n \rangle + 1)]^{1/2} \right\} \quad \text{III.15}$$

where p is an integer and I_p the p -th modified Bessel function of the 1st kind. $\langle n \rangle$ is the mean number of vibrational quanta in each oscillator at a temperature T ,

$$\text{i.e. } \langle n \rangle = \frac{e^{-\{\hbar\bar{\omega}/kT - 1\}}}{e^{-\{\hbar\bar{\omega}/kT - 1\}}}$$

s is the mean number of vibrational quanta emitted or absorbed in the electronic transition, and is given by:-

$$s = \frac{1}{2} \frac{(A^a - A^b)^2}{\hbar\bar{\omega}^3}$$

If each delta function of Equation III.15 is effectively "smeared out" over a range of energies, then the resultant continuous function is approximately Gaussian in energy (Lax, 1952). The predicted peak positions of the absorption and emission bands are independent of temperature, having the form:-

$$E_{ab}^0 \approx E_{ab}(\max) = \hbar\omega_{ba} + S\hbar\bar{\omega}$$

III.16

$$E_{ba}^0 \approx E_{ba}(\max) = \hbar\omega_{ba} - S\hbar\bar{\omega}$$

The predicted mean square widths of both bands are the same, namely

$$\begin{aligned} \langle [E - E(\max)]^2 \rangle_{Av} &= \{ \hbar\bar{\omega} \}^2 s \{ 2 \langle n \rangle + 1 \} \\ &= \{ \hbar\bar{\omega} \}^2 s \operatorname{Coth} \{ \hbar\bar{\omega} / 2kT \} \end{aligned}$$

III.17

Thus at low temperatures the band width is constant ($= \hbar\bar{\omega}\sqrt{s}$), and at high temperatures varies as \sqrt{T} .

Using wavefunctions calculated by Simpson (1949), Huang and Rhys (1950) found that for an F-centre in KBr, s has the value 3.6. The upper limit for s , corresponding to extreme localization of the ground state and diffusion of the excited state, was also calculated and found to be 55. The best available experimental value against which to check the

theory is 22.4 (Dexter, 1956a). The low theoretical estimation of s indicates that the long range interaction assumed by Huang and Rhys is inadequate, and that the local effects of the nearest neighbours of the F-centre are probably appreciable. The following experimental evidence supports this suggestion:-

(a) The peak position of the F-band shifts with temperature (Pohl, 1937; Russell and Klick, 1956).

(b) The widths of the absorption and emission bands are unequal (Botden et al., 1954).

Further, a theoretical treatment (Dexter, 1956) shows that most of the charge distribution of the F-centre ground state, and roughly half that of the excited state, lies within one interionic radius of the centre. For such a well-localized distribution, a "particle in a box" model (Ivey, 1947; Jacobs, 1954) would be more appropriate.

Pekar (1953) performed an F-centre calculation similar to that of Huang and Rhys and obtained somewhat better agreement with experiment. In addition to deriving for s the value of 26, he predicted the peak position of the emission band with fair accuracy.

(B) The Tight Binding Approximation

The essential concept of the tight binding model is that of a well-localized centre in which the associated electronic states are confined to the immediate vicinity of

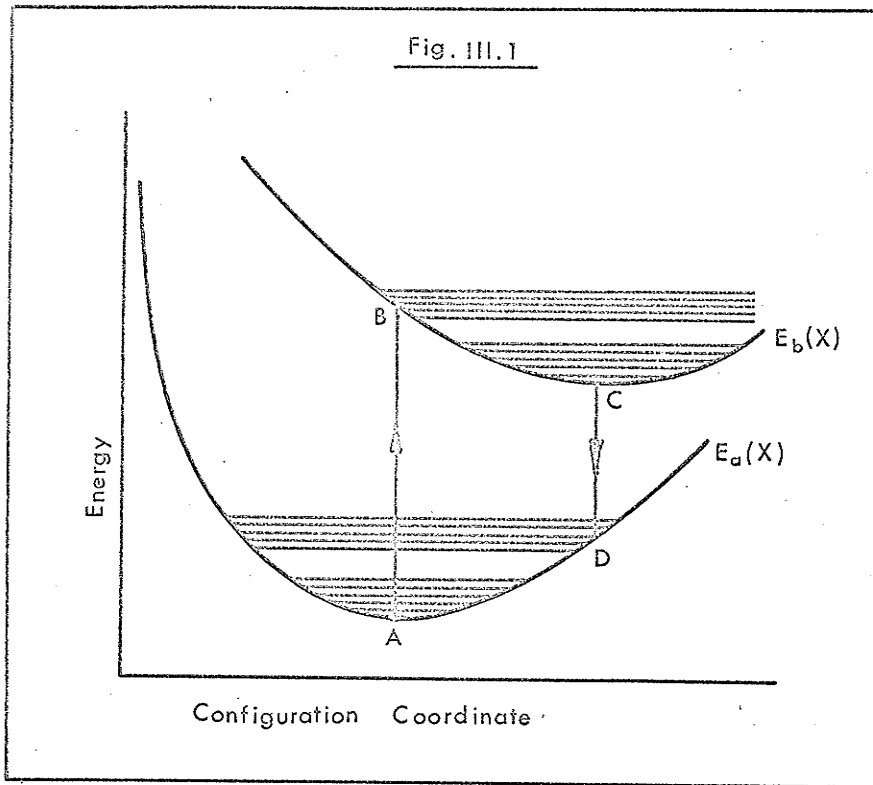
the centre, and are influenced only by the nearest neighbour ions.

If the physical properties of the substitutional impurity differ appreciably from those of the host ion which the impurity replaces, then the vibrational frequencies and equilibrium positions of the nearest neighbour ions will be modified and will depend upon the electronic state of the centre. In fact, Bjork (1957) has shown that if the centre creates new vibrational modes, then all others intrinsic to the host are excluded from the region, and thus the bulk vibrational spectrum may be ignored.

Von Hippel (1936) and Seitz (1939) proposed a localized model that has since become known as the "Configurational Coordinate Model". The tightly bound impurity is considered to interact predominantly with the six nearest neighbours of the face centred cubic structure, giving rise to eighteen degrees of freedom or "configuration coordinates". To a first approximation, transverse motion of the surrounding ions does not alter the distance to the impurity ion, so that motion in the six radial directions relative to the impurity will have the greatest effect on the potential energy of the centre. The most important oscillatory mode will be the "breathing mode", or in phase radial motion of the nearest neighbour ions. Hence, many centres may be approximated by one important configuration coordinate or

mode of vibration, possibly with several others of minor significance. Lax (1952) has shown that in certain cases a one-coordinate model may be used to describe a physically more complex centre, provided that the configuration coordinate is not directly associated with any single mode of vibration of the centre.

Since the potential energy of the centre varies quadratically with small displacements of the nearest neighbour ions from their equilibrium positions, the centre may be regarded as an harmonic oscillator with the usual wavefunctions and vibrational energy levels. The minima of different energy surfaces in configuration space occur at different values of the coordinates, since the equilibrium positions of the surrounding ions differ for each electronic state in question. Moreover, in ionic crystals one can predict, at least qualitatively, the relative positions of the ground and excited state minima. For a transition from the ground to a higher state in a localized positive centre, the charge distribution is effectively expanded, resulting in an increased attraction between the impurity and its surrounding ions. Thus the minimum of the excited state energy surface is at a smaller configuration coordinate value than is the ground state. The converse holds for a negative impurity centre, of which the F-centre is an example. The experimental results of Jacobs (1954), Russell and



Klick (1956) and the theory of Williams (1951), support the qualitative argument above. Also, since the charge distribution is more diffuse for the excited than for the ground state, the curvature of the excited state energy surface is expected to be smaller than that of the ground state. The F-centre data of Russell and Klick (1956) and of Klick et al. (1964) agree with this suggestion, whilst the data of Luty and Gebhardt (1962) disagree.

As a pedagogical tool, consider a physical system represented by one configuration coordinate and two electron states. For more than one coordinate, one may visualize a cross section of the energy surfaces, with all except one coordinate fixed.

With reference to Figure III.1, at low temperatures

the centre will be in a vibrational level close to the zero point (A) of the ground electronic energy surface (Curve a). According to the Born-Oppenheimer approximation, in the event of absorption a vertical transition will occur to some point (B) on the excited electronic energy curve. Since the high vibrational state reached is inconsistent with the low temperature of the crystal, the centre will oscillate rapidly, create lattice phonons, and decay in 10^{-10} to 10^{-11} seconds to the zero point region (C) of the excited state energy curve (Curve b). At a later time (approximately 10^{-8} seconds), photon emission will occur from (C), leaving the centre in some high vibrational level (D) of the ground electronic state. Again energy will be transferred to the lattice by means of phonon creation, and the centre decays to the zero point region (A). The Stokes' Shift, as mentioned earlier, is the difference in the energies of absorption (AB) and emission (CD).

Using the current model, it is now possible to retrace parts of the theoretical discussion, making certain approximations in order to simplify the expressions for the absorption and emission band shapes (Equations II.5 and II.6).

To recapitulate, the matrix elements $r_{ab\alpha\beta}$ and $r_{ba\beta\alpha}$ were replaced by suitable averages as discussed in connection with the Condon approximation (Chapter II), and the transition energies $E_{ab\alpha\beta}$ and $E_{ba\beta\alpha}$, under the narrow band

approximation, were replaced by mean values. Now, since in inorganic phosphors transitions between individual vibrational levels are not generally seen under the envelope of the electronic transition, both Lorentzian shape functions $F_{ab\alpha\beta}^o[E]$ and $F_{ba\beta\alpha}^e[E]$ may be replaced by the delta function:-

$$\delta \{E_{b\beta} - E_{a\alpha} - E\}$$

Using these approximations Equations III.9 and III.10 were derived, with the normalized absorption and emission band shapes given by:-

$$I_{ab} = A_{v\alpha} \sum_{\beta} \left| \int \Pi_{\alpha\alpha}^*(\chi) \Pi_{b\beta}(\chi) d\chi \right|^2 \delta \{E_{b\beta} - E_{a\alpha} - E\} \quad \text{III.18}$$

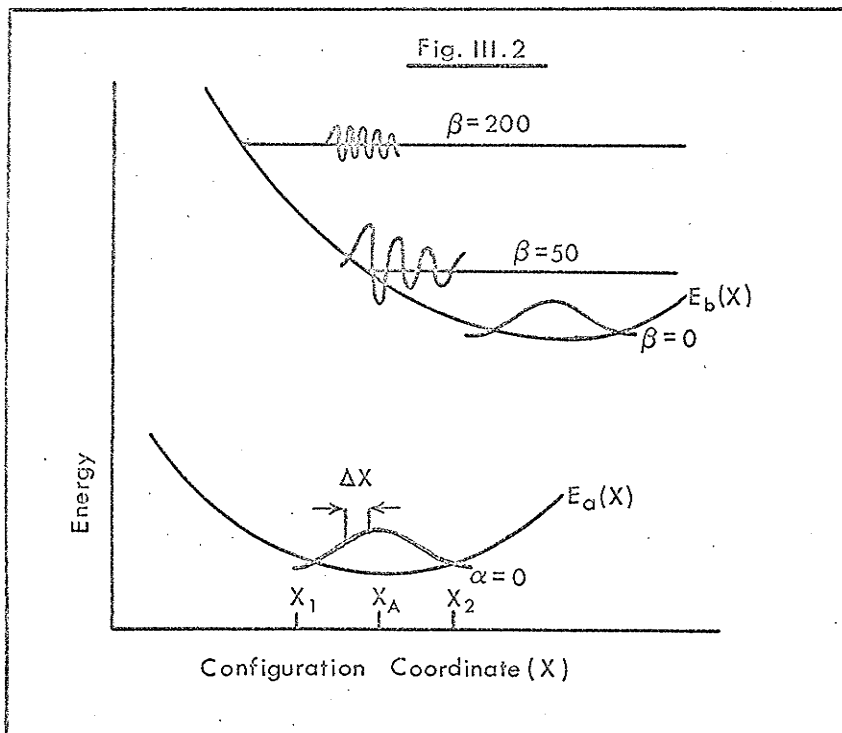
and

$$I_{ba} = A_{v\beta} \sum_{\alpha} \left| \int \Pi_{b\beta}^*(\chi) \Pi_{a\alpha}(\chi) d\chi \right|^2 \delta \{E_{b\beta} - E_{a\alpha} - E\} \quad \text{III.19}$$

Apart from the different representation of the delta function, the above equations are functionally the same as III.11 and III.12 pertaining to the linear approximation. The difference is that the vibrational matrix elements are computed using different nuclear wavefunctions.

(C) The Franck-Condon Principle

The Franck-Condon Principle, by means of which Equations III.18 and III.19 can be greatly simplified, assumes



that during an electronic transition each vibrational mode either changes by many quanta, or does not change at all.

If the vibrational modes of the ground and excited electronic states are described by the wavefunctions $\{Q_2^a(X)\}$ and $\{Q_2^b(X)\}$ respectively, then at low temperatures the most important mode of the ground electronic state is that for which $a=0$. The important modes of the excited electronic level are those for which $\beta \gg 1$. The band shapes are then determined by the square of matrix elements of the form:-

$$\int Q_0^{a*}(X) Q_\beta^b(X) dX$$

III.20

Figure III.2 shows that outside the region X_1 to X_2

the zero point vibrational wavefunction $\psi_0^a(X)$ is very small, and thus makes a negligible contribution to the above integral. Contributions to the integral from an element ΔX that is inside the range X_1 to X_2 may be subdivided as below:-

(i) When β is zero or small, the contribution is negligible since the amplitude of the wavefunction $\psi_\beta^b(X)$ is very small in the region ΔX .

(ii) When β is very large, the vibrational wavefunction oscillates very rapidly in the region of ΔX , the positive and negative swings having approximately equal amplitudes, again resulting in a negligible contribution to the integral.

(iii) When β has some intermediate value, such that $E_{b\beta}$ is close to the classical parabolic curve $E_b(X)$ shown in Figure III.2, then and only then can an appreciable contribution to the integral III.20 occur.

Thus setting $E_{b\beta} = E_b(X)$, Equation III.18 may be written as:-

$$\begin{aligned} I_{ab}[E] &= A_{v_a} \sum_{\beta} \int \Pi_{a\alpha}^*(X) \Pi_{b\beta}(X) dX \int \Pi_{a\alpha}^*(X') \Pi_{b\beta}(X') dX' \delta\{E_b - E_{a\alpha} - E\} \\ &= A_{v_a} \int \left| \Pi_{a\alpha}(X) \right|^2 dX \delta\{E_b - E_{a\alpha} - E\} \end{aligned} \quad \text{III.21}$$

together with a similar expression for the emission band shape. The above integral may be evaluated to yield:-

$$I_{ab}[E] = A v_{\alpha} \left\{ \left| \Pi_{\alpha\alpha}(R_{\alpha}) \right|^2 \left[\frac{dX}{dE_b(X)} \right]_{X=R_{\alpha}} \right\} \quad \text{III.22}$$

where R_{α} are the values of the nuclear coordinates for which energy is conserved.

$$\text{i. e.} \quad E_b(R_{\alpha}) - E_{\alpha\alpha} = E$$

Thus the band shape function is the thermal average over the electronic ground state vibrational levels of the product of two factors. The first is the initial probability of occupation of position, and the second is the transition energy at that position.

At high temperatures, many vibrational levels in the ground electronic state will be involved in absorptive transitions so that $E_{\alpha\alpha}$ may be replaced by a mean value $E_{\alpha}(X)$ and Equation III.22 written as:-

$$I_{ab}[E] = A v_{\alpha} \left| \Pi_{\alpha\alpha}(R) \right|^2 \left[\frac{dX}{d\{E_b(X) - E_{\alpha}(X)\}} \right]_{X=R} \quad \text{III.23}$$

where R represents the configuration coordinate values for which the transition energy E equals $E_b(X) - E_{\alpha}(X)$.

A further simplification of Equations III.22 and III.23 results if the assumption is made that, over the range of

configurational coordinates involved in the transition, (X_1 to X_2 in Figure III.2), the energy surface $E_b(X)$ may be approximated by a straight line of slope $d\{E_b(X)\}/dX|_{x_A}$. This reduces the second factor of Equation III.22 to a constant, and the shape function is then determined by the thermally averaged quantum mechanical distribution function, which Lax (1952) has shown to be Gaussian in X . The width, $l(T)$ of the Gaussian absorption band is related to the absolute temperature by:-

$$l(T) = l(0) \left[\coth\{\hbar\nu_0/2kT\} \right]^{1/2} \quad \text{III.24}$$

where $\hbar\nu_0$ is the energy separation of the electronic ground state vibrational levels, and $l(0)$ is the width at absolute zero. A similar equation exists for the emission band.

Dexter (1958) has examined the validity of the approximation whereby the upper configuration curve (b) is replaced by a straight line. He calculated that if the curvature is not neglected, then at low temperatures a high energy tail is to be expected on the absorption band, and a low energy tail on the emission band. The results of Russell and Klick (1956) and of Patterson and Klick (1957) show the above distortions. At higher temperatures, however, occupation of levels above the zero point vibrational level of the ground electronic state results in a decrease in the high energy tail of the absorption band, and in the low energy

tail of the emission band. Thus the temperature and curvature effects tend to cancel, producing bands that are more nearly Gaussian than might otherwise be expected.

(D) Calculation of the Configurational Coordinate Diagram

In order to construct in theory the configuration coordinate diagram, the energy surfaces $E_a(X)$ and $E_b(X)$ must be determined.

Near its minimum, each curve has the functional form

$$E = \frac{1}{2} \kappa X^2$$

where the force constants κ_a and κ_b are related to the vibrational frequencies ω_a and ω_b respectively by relationships of the form:-

$$\kappa = M\omega^2$$

M is the effective mass of the centre and is usually taken as the total mass of the impurity and six nearest neighbours (Curie, 1963).

Now $E_a(X)$ and $E_b(X)$ are the expectation values of the complete Hamiltonian $H_I(X)$ of the centre, which may be expressed in the following form using perturbation theory:-

$$H_I(X) = H_0 + \lambda(X)$$

where H_0 is the Hamiltonian of the isolated impurity atom, and $\lambda(X)$ represents the interaction of the impurity with its surroundings, under the assumption that $H_0 \gg \lambda(X)$.

H_0 may then be determined by solving the Schrödinger equation for the isolated impurity atom:-

$$H_0 \varphi_i^0(r) = E_i \varphi_i^0(r)$$

where $\varphi_i^0(r)$ are the wavefunctions of the isolated atom. The wavefunctions of the centre embedded in the host may then be expressed in the form:-

$$\phi_{ix}(r) = \varphi_i^0(r) + \mu_{ix}(r)$$

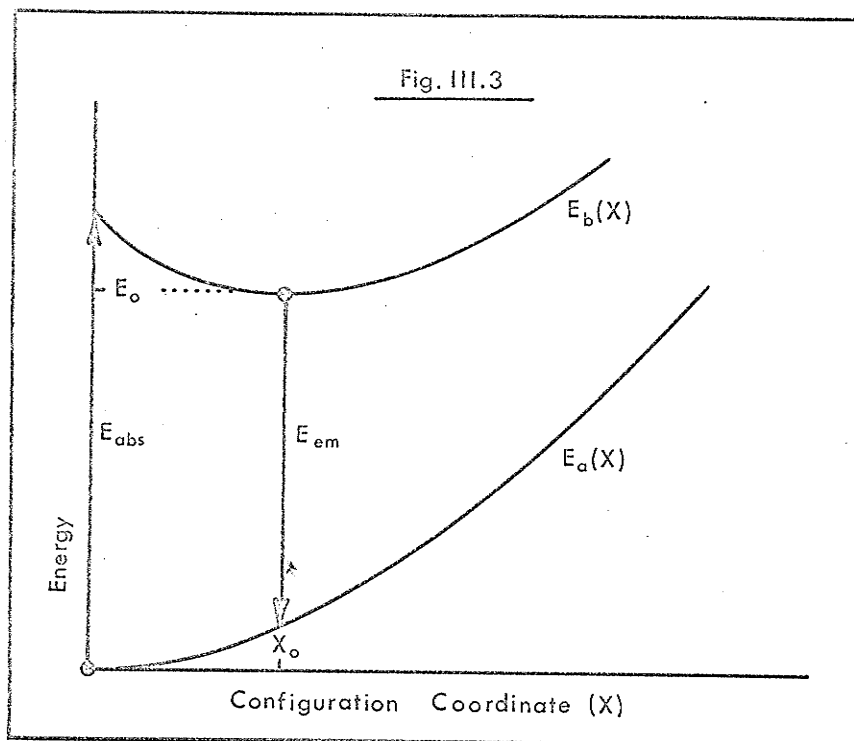
provided the perturbation is small. A somewhat better approximation that uses symmetrically orthogonalized wavefunctions is given by Löwdin (1950) and discussed by Knox and Dexter (1956).

The expectation value of the total Hamiltonian is then given by:-

$$\begin{aligned} E_i(X) &= \int \phi_{ix}^*(r) [H_0 + \lambda(X)] \phi_{ix}(r) dr \\ &\approx \int \varphi_i^{0*}(r) H_0 \varphi_i^0(r) dr + \int \varphi_i^{0*}(r) \lambda(X) \varphi_i^0(r) dr \\ &= E_i^0 + e_i(X) + \text{smaller terms} \end{aligned}$$

Thus, providing that a suitable choice of $\lambda(X)$ can be made, the transition energies can be found and the configurational coordinate diagram completed.

The above theoretical technique was applied by



Williams (1951) to the system $KCl(Tl)$, and will be discussed later.

(E) Construction of the Configurational Coordinate Diagram

From Experimental Data

Using the interpretations of the previous section, the construction of the diagram reduces to the determination of the relative vertical and horizontal displacements of the ground and excited state electronic surfaces, together with their parabolic constants.

In Figure III.3 the origin of coordinates is taken at

the minimum of the ground electronic state, and with the indicated notation, the ground and excited state curves are described respectively by the equations:-

$$E_a(X) = \frac{1}{2} \kappa_a X^2 \quad \text{III.25}$$

$$E_b(X) = E_o + \frac{1}{2} \kappa_b \{X - X_o\}^2 \quad \text{III.26}$$

where κ_a and κ_b are defined as in the previous section.

The energies corresponding to the peaks of the absorption and emission bands, E_{abs} and E_{em} , are given by:-

$$E_{abs} = E_o + \{s_b + \frac{1}{2}\} \hbar \omega_b - \frac{1}{2} \hbar \omega_a \quad \text{III.27}$$

$$E_{em} = E_o - \{s_a + \frac{1}{2}\} \hbar \omega_a \quad \text{III.28}$$

where s_a and s_b label the vibrational levels within the electronic states. Now recalling Equation III.24, the full width at half maximum of the absorption band is:-

$$L(\tau) = L(0) \left[\text{Coth} \{ \hbar \omega_a / 2kT \} \right]^{1/2}$$

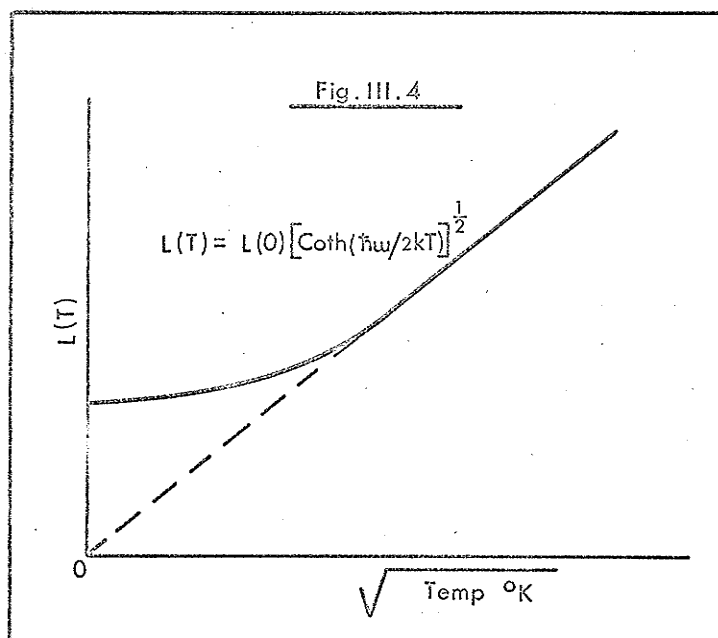
with a similar equation relating the emission band width to the absolute temperature. The functional dependence is shown schematically in Figure III.4.

At high temperatures, $\text{Coth} \{ \hbar \omega / 2kT \} \rightarrow \{ \hbar \omega / 2kT \}^{-1}$

$$\text{so that } L(\tau) \rightarrow L(0) \{ \hbar \omega / 2kT \}^{-1/2} \quad \text{III.29}$$

Thus by plotting the graph experimentally, and measuring its

slope and the projected intercept on the $L(T)$ axis, the vibrational frequencies ω_a and ω_b can be determined. A two parameter least squares fit to the experimental data would of course be more desirable. The least squares fitting of functions in which both dependent and independent variables are in error, as in this case, has been treated by Deming (1943).



Now since the spacing of the vibrational levels is small compared to the spacing of the electron levels, (Russell and Klick, 1956), Equations III.27 and III.28 may be approximated by:-

$$E_{\text{abs}} = E_0 + \frac{1}{2} \kappa_b X_0^2 \quad \text{III.30}$$

and

$$E_{\text{em}} = E_0 - \frac{1}{2} \kappa_a X_0^2 \quad \text{III.31}$$

Thus the parameters κ_a and κ_b may be determined, and the configurational coordinate diagram constructed. Approximate values for the mean numbers of phonons involved in the absorptive and emissive processes may then be calculated from Equations III.27 and III.28.

The configurational coordinate model has been applied successfully to several different impurity centres. Russell and Klick (1956) have studied the F-centre in a variety of the alkali halides; Klick, Patterson and Knox (1964) investigated the F-centre in KCl; the Tl^+ centre has been the subject of studies by Johnson and Williams (1952, 1960). The Mn^{2+} centre in $ZnSiO_4$ was studied by Klick and Schulman (1950). Previous applications of the configurational coordinate model to $NaI(Tl)$ will be reviewed later.

(F) Assignment of the Electronic States

Although the configurational coordinate model described in the previous section considered only the ground state plus a single excited electron level, most impurity centres can be excited to more than one state. The model may however be applied to the ground and each excited state in turn, provided that the experimentally observed absorption or emission bands can be attributed to specific electronic transitions. Often the assignment can be made on the basis of the position and intensity of each band.

The pioneer work of Hilsch (1927, 1937), Forró (1929,

1930), and many others on the absorption spectra of Tl^+ and Pb^{++} activated alkali halide phosphors provided a wealth of experimental data. At least two absorption bands, named the "A" and "C" bands, were seen in each case; and sometimes another weak one, called the "B" band, was observed between the A and C bands. The C band was always found to be the strongest and to lie on the high energy side of the A band. Sometimes the C and B bands were obscured by the fundamental absorption edge of the host crystal. The integrated absorption coefficient of the bands was found to be proportional to the impurity concentration, and the oscillator strength of the B band was found to increase with temperature.

On the basis of the above experimental data, Seitz (1938) gave the first explanation of the properties of the Tl^+ doped alkali halides. Since the Tl^+ monovalent ion is the most stable thallos ion at the high temperatures at which crystals are grown, he assumed that the Tl^+ ions substitutionally and randomly replaced the positive ions of the host. Seitz then proposed two processes by which to explain the absorption bands: the intraionic excitation of the Tl^+ ion, and the transfer of an electron to the Tl^+ ion from a neighbouring halogen site. The first process was thought to be the more likely because:-

(i) The positions of the A, B, and C bands of Tl^+ move only slightly when one host material is substituted for

another.

(2) The electron transfer model predicts a doublet structure that was not then seen. However, recent experiments (see later) lend more credence to this model.

(3) Absorption bands arising from electron transfer transitions were expected to appear at higher energies than did the observed bands.

By considering the term diagram of the free Tl^+ ion and its expected modifications when the ion is embedded in a host material, Seitz suggested that the low energy A band be attributed to the ${}^1S_0 \rightarrow {}^3P_1 \left\{ {}^1A_1 \rightarrow {}^3T_1 \right\}$ transition, and the C band to the completely allowed transition ${}^1S_0 \rightarrow {}^1P_1 \left\{ {}^1A_1 \rightarrow {}^1T_1 \right\}$. The bracketed spectral notation is taken from Eyring et al. (1944). The singlet-triplet transition is not consistent with the spin-selection rule and thus the A band should be weaker than the C band, as confirmed experimentally by Hilsch (1927). Although under cubic symmetry transitions such as ${}^1S_0 \rightarrow {}^3P_0$ or ${}^3P_2 \left\{ {}^1A_1 \rightarrow {}^3A_1 \right.$ and ${}^1A_1 \rightarrow {}^3E$ or ${}^3T_2 \left. \right\}$ are forbidden, they may be expected to occur with small intensity if the crystal symmetry is lowered, for example, by lattice vibrations. Since the intensity of the B band is weak at low temperatures and increases as the temperature rises (Ferró, 1930), it was attributed to a transition of the above type, namely to the ${}^1S_0 \rightarrow {}^3P_2 \left\{ {}^1A_1 \rightarrow {}^3E \right.$ or ${}^3T_2 \left. \right\}$ transition. Using the configurational coordinate model and

the above electron level assignment, Williams (1951, 1951a) and Williams and Hebb (1951) considered the compound KCl(Tl) from a theoretical standpoint. The totally symmetrical displacement of the nearest neighbour Cl^- ions surrounding the Tl^+ ion was taken as the configuration coordinate. The energy of the ground ($^1\text{S}_0$) and excited ($^3\text{P}_1$) states of the Tl^+ ion were calculated using, when possible, the available experimental data. Their results explained quite well the A absorption band and its associated emission band, together with their temperature and pressure dependence (Johnson and Studer, 1951; Johnson and Williams, 1954).

Johnson and Williams (1952) and Johnson (1954) applied the same theory to the high energy absorption and emission bands of KCl(Tl) , assuming that the bands resulted from $^1\text{S}_0 \leftrightarrow ^1\text{P}_1$ transitions. They estimated the energy of the $^1\text{P}_1$ state, and suggested that near resonance of the level with the host resulted in the poor agreement of their estimate with experimentally determined values. More recent work, however, (Aoyagi and Kuwabara, 1960; Edgerton and Teegarden, 1963) suggests that the transition assignment may be in error, since the emission band is not seen at low Tl^+ concentrations.

As indicated earlier, the theory adopted by Williams predicts that the absorption and emission bands have no vibrational structure and are Gaussian in shape. Some experiments, however, have shown the presence of structure

within the absorption and emission bands. Hüniger and Rudolph (1940) observed structure within the A and C absorption bands of Sn^{++} doped alkali halides, and Fukuda (1964) reports structure in the A and C absorption bands of NaCl, KCl, and KBr doped with In^+ , Sn^{++} , Tl^+ and Pb^{++} . In attempting to discover the D band in KI(Tl), Yuster and Delbecq (1953) observed that the C band is triplet, and Williams et al. (1957) noticed structure in the A and C bands of KCl(In).

Patterson (1958) observed a doublet structure at room temperature in the A and C bands of KCl(Tl). The structure, however, was not present at or below the temperature of liquid nitrogen. He suggested the existence of two kinds of Tl^+ centres:-

(1) A Tl^+ ion embedded in a face centred cubic (NaCl) structure.

(2) A Tl^+ ion embedded in a local body centred cubic (CsCl) structure.

The high energy absorption and emission components were attributed to the CsCl type centre since Eppler and Drickamer (1960) noted that the A band shifts to higher energy during a pressure-induced phase change from NaCl type structure to CsCl type.

Yuster and Delbecq (1953) found that at high Tl^+ concentrations in KI(Tl) an additional band was present in

the low energy shoulder of both A and C absorption bands. Moreover, the intensity of the additional bands varied linearly, not with the Tl^+ concentration as did the A and C bands, but with the square of the Tl^+ concentration. These new bands were attributed to the $(Tl^+)_2$ "dimer" centre which consists of two thallos ions as near neighbours. Van Sciver (1955), Uchida and Kato (1959), and Matsui (1967), following the pioneer work on $NaI(Tl)$ by Hilsch (1927, 1937), Hilsch and Pohl (1928), and Lorenz (1928), observed bands characteristic of the dimer centre in absorption, emission, and excitation spectra taken at high concentrations of Tl^+ . Butler (1956) and Patterson and Klick (1957) reported a small band in the low energy shoulder of the A absorption band of $KCl(Tl)$. Since the band was not seen by Fukuda (1964), who used samples of low Tl^+ content, it probably resulted from a dimer transition.

Zazubovich et al. (1964) found that in Sn^{++} doped KCl , KBr , and KI the A band was doublet whilst the C band was triplet, and suggested that the structure was the result of cation vacancies in the lattice. Fukuda (1964), Fukuda et al. (1964), and Onaka et al. (1965) have observed similar structures in $NaCl(In)$, $KBr(In)$, $NaCl(Sn)$, $KBr(Sn)$, $NaCl(Pb)$, and $KCl(Pb)$.

In recent years, investigation of the time dependence of the luminescence spectra of doped alkali halides has

received considerable attention (Illingworth, 1964; Trinkler and Piyavin, 1965; Wall, 1969). The results, in general, confirm the presence of structure within the A and C bands. Edgerton and Teegarden (1963, 1964), Edgerton (1965), and Fukuda (1964) conclude that the multiplet structures may be explained by the Jahn-Teller Theorem (Jahn and Teller, 1937, 1938; Van Vleck, 1939; Öpik and Pryce, 1957). This theorem as applied to luminescence centres, states that a geometrical arrangement of atoms about a centre in a degenerate electronic state is unstable, so that the ions will move to destroy at least part of the degeneracy. For F-centres, or Tl^+ centres in alkali halides, the degeneracy of the p-states is not removed by the cubic crystal field, so that according to the theorem a distortion of the surroundings of the centre is required in order to remove part of the degeneracy. The Jahn-Teller Effect will be considered again later.

CHAPTER IV

DATA ACCUMULATION AND CORRECTION

(A) Experimental Apparatus

The apparatus was designed so that between liquid nitrogen and room temperatures a sample crystal could be subjected to two different but related experiments:-

(i) Excitation Experiment

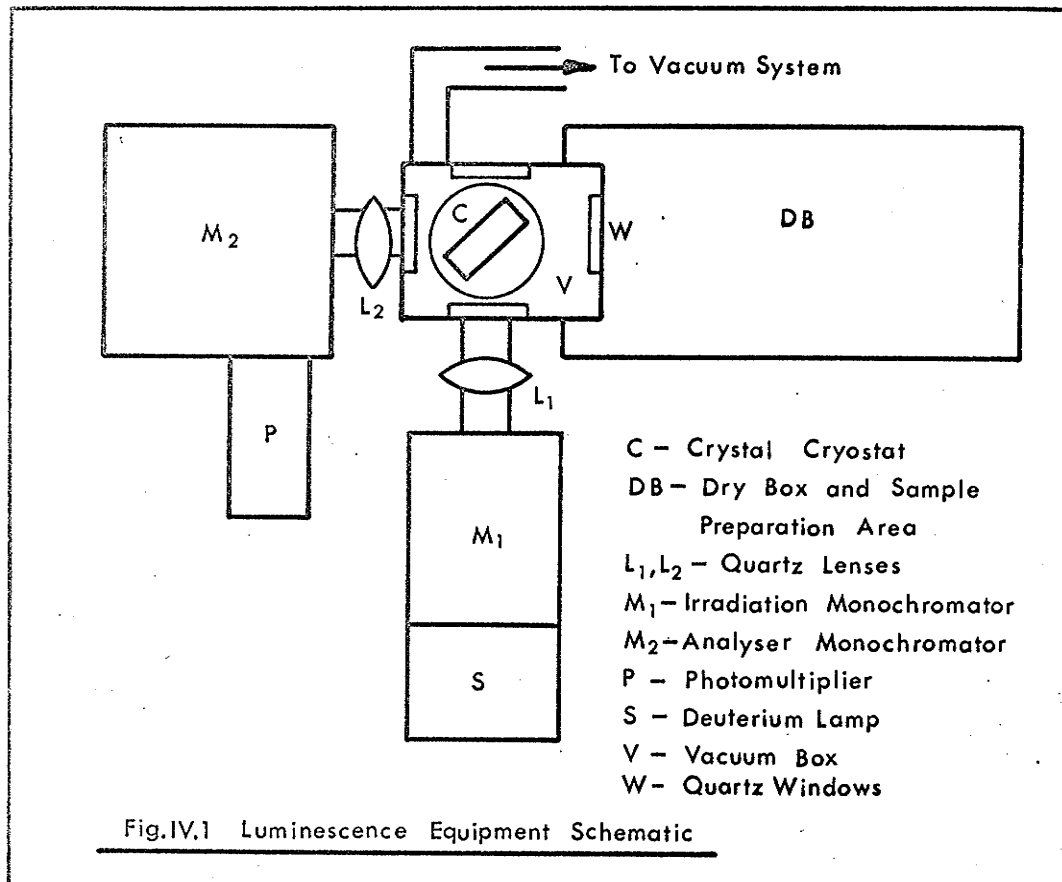
For this study the intensity of light at a set wavelength emanating from the crystal was investigated as a function of exciting wavelength.

(ii) Emission Experiment

In this investigation the crystal was excited by monochromatic light, and the emission intensity studied as a function of wavelength.

(1) Mechanical Equipment

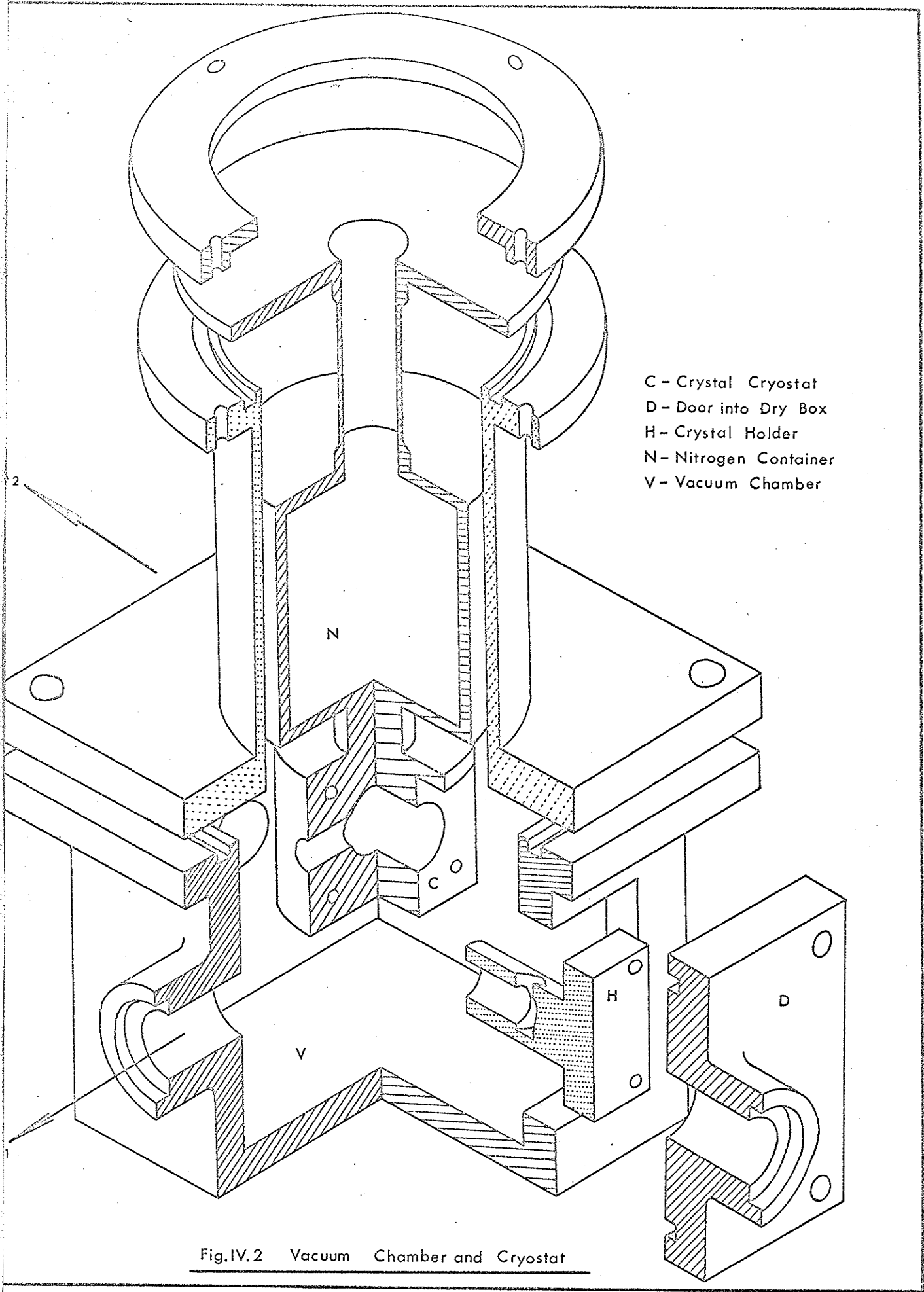
Figure IV.1 indicates schematically the equipment arrangement, and Figure IV.2 shows details of the vacuum box and crystal cryostat. Sample crystals prepared in the dry box (DB) and mounted in the crystal holder (H), were transferred into the vacuum chamber (V) and secured in the cryostat (C). Light from the high pressure deuterium source (S), its wavelength selected by the irradiation monochromator (M_1), illuminated the crystal via the quartz lens (L_1). Luminescent radiation from the sample was collected by the



quartz lens (L_2), focussed onto the entrance slit of the analyser monochromator (M_2), and its intensity detected by the photomultiplier (P). The indicated crystal orientation eliminated reflection of the incident beam into the analyser monochromator (M_2). The temperature of the sample was measured by a copper-constantan thermocouple attached to the brass crystal holder.

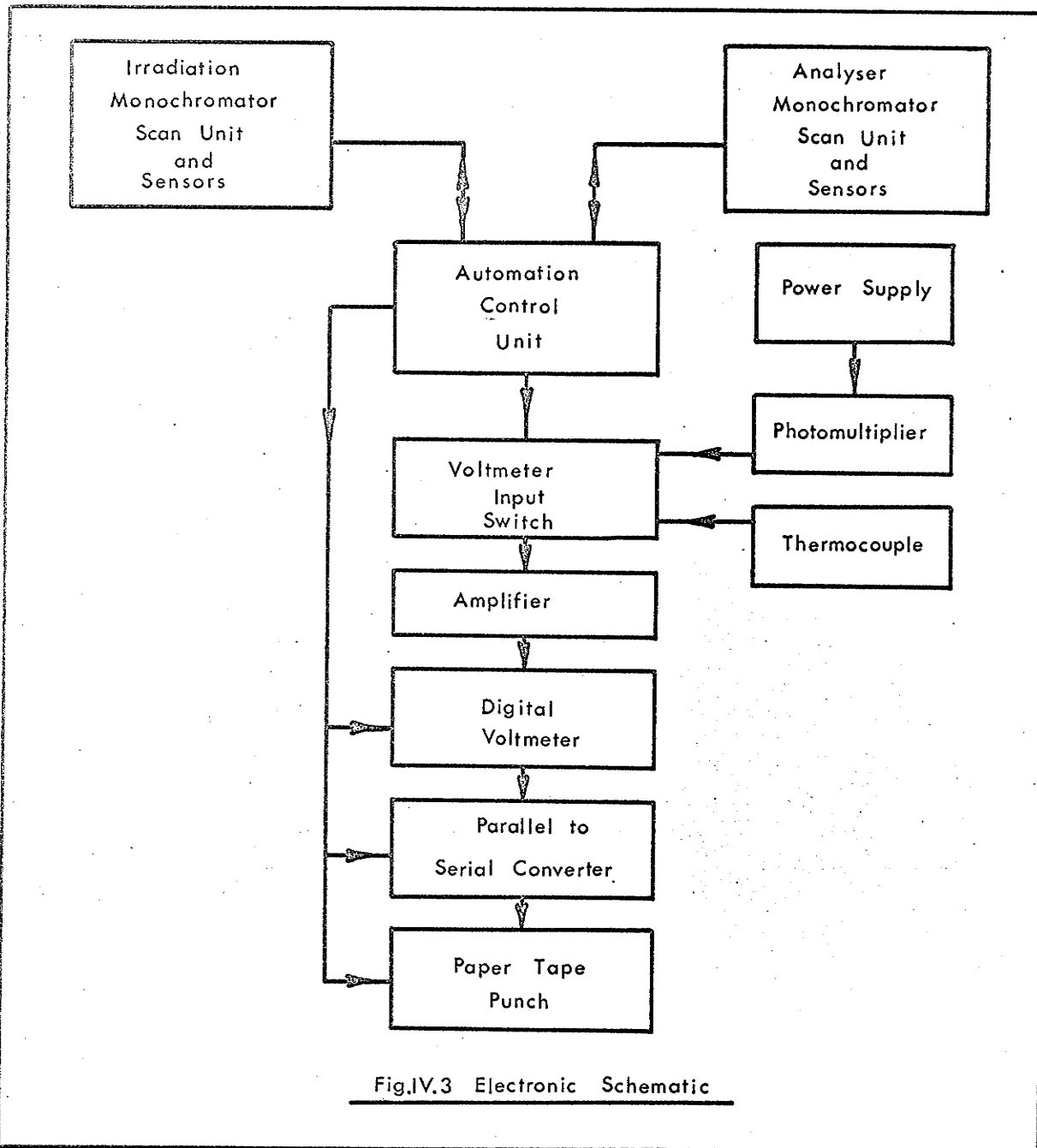
(2) Electronic Equipment

Since the nature of the project required the



- C - Crystal Cryostat
- D - Door into Dry Box
- H - Crystal Holder
- N - Nitrogen Container
- V - Vacuum Chamber

Fig.IV.2 Vacuum Chamber and Cryostat



accumulation of a large number of excitation and emission spectra, it was desirable to automate the system. This was

achieved as indicated schematically in Figure IV.3. Each of the monochromators was equipped with a reversible synchronous motor which drove the grating through an appropriate gear train. A number of cams attached to each grating drive shaft triggered microswitches which in turn set ring counters in the automatic control unit. The state of the ring counters controlled the sequential process of data accumulation according to the following cycle:-

Phase (i)

With the irradiation monochromator set to excite the sample at a given wavelength, the analyser monochromator scanned the emission spectrum until the spectral region of interest was reached. At this point a microswitch closed causing the control unit to feed the photomultiplier output to the digital voltmeter. The voltmeter, under command of a train of pulses generated by the control unit, sampled its direct current input at regular intervals determined by the time separation of the pulses, and fed its binary coded decimal output through a parallel to serial converter into the tape punch.

Phase (ii)

At the end of the spectral region of interest, another microswitch closed causing the control unit to stop output of the encoded spectrum, and to switch the voltmeter input to the thermocouple. The converter then punched out the crystal

temperature, and a strip of "buzzed" tape to separate one spectrum from the next.

Phase (111)

Closure of a third microswitch reversed the direction of the analyser scan, permitting the grating to return to the position at which Phase (1) commenced, whereupon a fourth switch closed and the cycle was repeated. While returning to its initial position no data were collected, but the irradiation monochromator was activated and set to excite the sample at a new wavelength. The wavelength range over which the sample was excited could be adjusted by two cams operating microswitches, while a third cam determined the wavelength interval between successive excitations.

In parallel with the automatic system was an auxiliary manual one, permitting interruption or suppression of any phase of the cycle.

The wavelength corresponding to the first recorded point of each spectrum was determined by the angular position of the grating drive shaft at which a microswitch closed. Some difficulty was anticipated and experienced in achieving reproducibility of this angular position. Suitable design of the cam profile, however, resulted in variations of less than ± 20 minutes of arc, or equivalently ± 2 Angstrom on the analyser monochromator and ± 4 Angstrom on the irradiation monochromator. Since spectra were usually taken with an

instrument band pass of 132Å over a wavelength range in excess of 1000Å, the above precision was considered sufficient for present needs.

The following is a list of model numbers or origins of various items of equipment used:-

High Pressure Deuterium Lamp	Bausch and Lomb	#33-86-35-01
Irradiation Monochromator	Bausch and Lomb	#33-86-25
Analyser Monochromator	Bausch and Lomb	#33-86-45
Photomultiplier	E.M.I.	#6256
High Voltage Supply	Keithley Model	242
Amplifier	Magnetic Instruments Model	759-5
Digital Voltmeter	Vidar Model	500
Parallel to Serial Converter	Designed and built in the laboratory from DEC Modules	
Paper Tape Punch	Tally Model	420
Vacuum System	Mercury Diffusion Pump	

(B) Sample Preparation

Single crystals of NaI having a nominal thallium concentration of 0.2M% were purchased from Harshaw Chemical Company. Because of the extremely hygroscopic nature of NaI(Tl), samples were prepared in a dry environment. Crystals one centimeter square by one to two millimeters thick were cleaved from a single crystal block. Immediately after cleavage, the sample was transferred through a door

connecting the dry box to the crystal cryostat (Figure IV.1 and IV.2). The vacuum chamber was then sealed and exhausted to a pressure between 10^{-4} and 10^{-5} mm. of mercury.

(C) Experimental Procedure

As indicated in the previous sections of this chapter, excitation and emission spectra were taken in the range between liquid nitrogen and room temperatures. The usual procedure was to take spectra at room temperature, then cool the sample to liquid nitrogen temperature and repeat the experiments. Following this, the nitrogen was removed and the cryostat allowed to warm up by means of conduction through the thin stainless steel dewar neck and heat transfer through the vacuum. Spectra were then taken at intermediate temperatures during the warmup. The time taken for the cryostat temperature to change from near that of liquid nitrogen to 0°C . was about eight hours, depending upon the vacuum. Even at the lowest temperatures the rate of temperature rise was no higher than two centigrade degrees per minute, so that over the three or four minutes required to take a spectrum, the temperature was sensibly constant. In order to reduce the warming rate and therefore the temperature lag between the cryostat and crystal, the latter was embedded within the large mass of metal comprising the crystal holder (Figure IV.2), and kept in intimate contact by a spring.

As previously mentioned, all data were punched on

strip paper tape. The numerical coding was chosen to be compatible with an IBM 1620 computer so that the spectra could be transferred onto cards prior to correction and analysis by an IBM 360/65 computer.

(D) Data Correction

Before the luminescence spectra could be analysed and interpreted, it was necessary to apply certain correction factors. These are outlined below:-

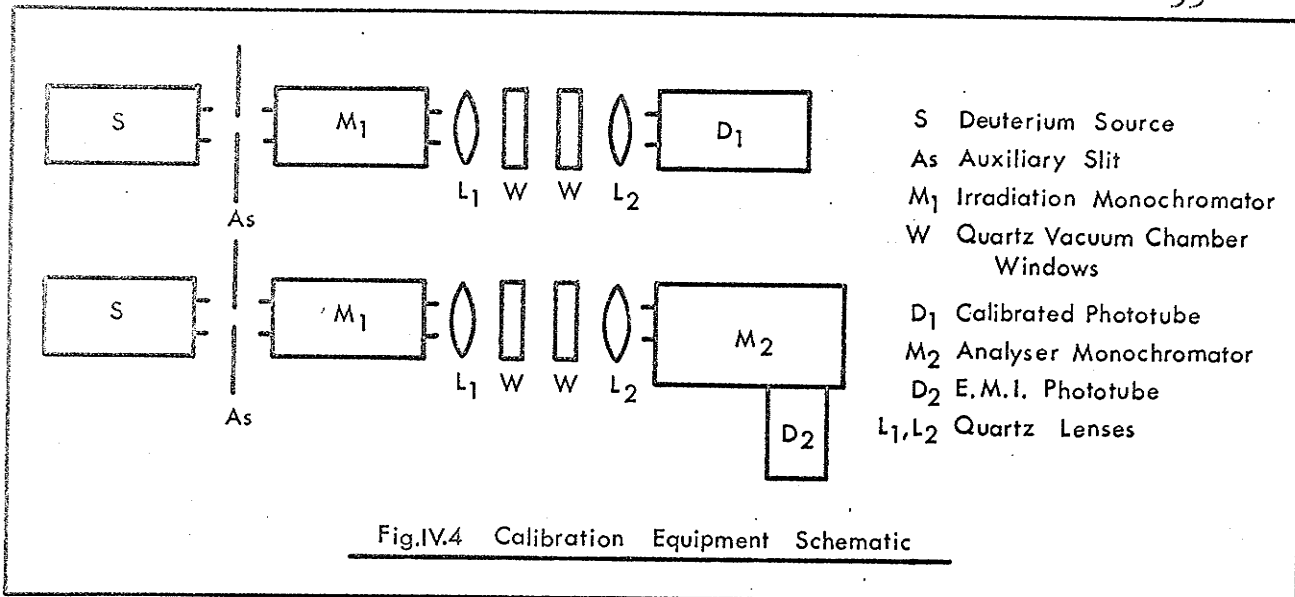
(1) Spectral Response Correction

One of the problems encountered in broad band luminescence experiments is that the spectral response curves of monochromators, photomultipliers, windows and lens systems are dependent upon the wavelength of the radiation passing through the system. In addition, there is no light source available which ranges with uniform intensity from the ultraviolet to the visible. Thus it is necessary to determine the following quantities as a function of wavelength:-

(i) The relative intensity of light incident on the crystal.

(ii) The response to the luminescent emission of the analyser system, comprising the monochromator and photomultiplier combination and associated optics.

These spectral response curves were determined by two auxiliary experiments, A and B, shown in Figure IV.4. In



the first, the deuterium lamp and irradiation monochromator were mounted in series with an R. C. A. 7200 photomultiplier previously calibrated by the Radio Corporation of America, and the light intensity $I_1\{\lambda\}$ seen by the detector plotted as a function of wavelength. In the second experiment, the lamp and irradiation monochromator were placed in series with the analyser monochromator and its associated E.M.I. photomultiplier, and the intensity $I_2\{\lambda\}$ again plotted as a function of wavelength. The response curves were determined as below, where $R_1\{\lambda\}$ is the relative response of the lamp-irradiation monochromator combination, and $R_2\{\lambda\}$ that of the analyser monochromator and E.M.I. photomultiplier. $D\{\lambda\}$ is the known relative response of the calibrated R. C. A. phototube.

$$I_1\{\lambda\} = R_1\{\lambda\} D\{\lambda\}$$

$$I_2\{\lambda\} = R_1\{\lambda\} R_2\{\lambda\}$$

from which $R_1\{\lambda\} = I_1\{\lambda\}/D\{\lambda\}$
 and $R_2\{\lambda\} = I_2\{\lambda\}D\{\lambda\}/I_1\{\lambda\}$

The relative response curves clearly depend upon the band pass or slit width of the monochromators. Consequently the calibration was done using slit geometry identical to that employed in the luminescence experiments. The light intensity reaching the detector during spectral calibration, however, was much greater than that emitted under excitation of a crystal, so that using the above slit geometry, some means of regulating the intensity was required, in order to prevent damage to the phototubes and to operate in the same signal range. It was determined experimentally that variation of the monochromator slit heights caused considerable distortion of the response curves, but that an auxiliary slit mounted perpendicularly to the monochromator slits in the position indicated in Figure IV.4 resulted in no noticeable distortion. An auxiliary slit mounted in the above position was thus employed as the intensity control.

Figure IV.5 shows the response curve of the R.C.A. calibrated phototube, and in Figures IV.6, IV.7, IV.8, and IV.9 are shown the relative response curves of the equipment for the instrumental band passes indicated.

Since each recorded point of a given luminescence spectrum requires correction by a factor derived from one of the above curves, the response correction of many such spectra

Fig.IV.5 Relative Response of Calibrated Photomultiplier Tube

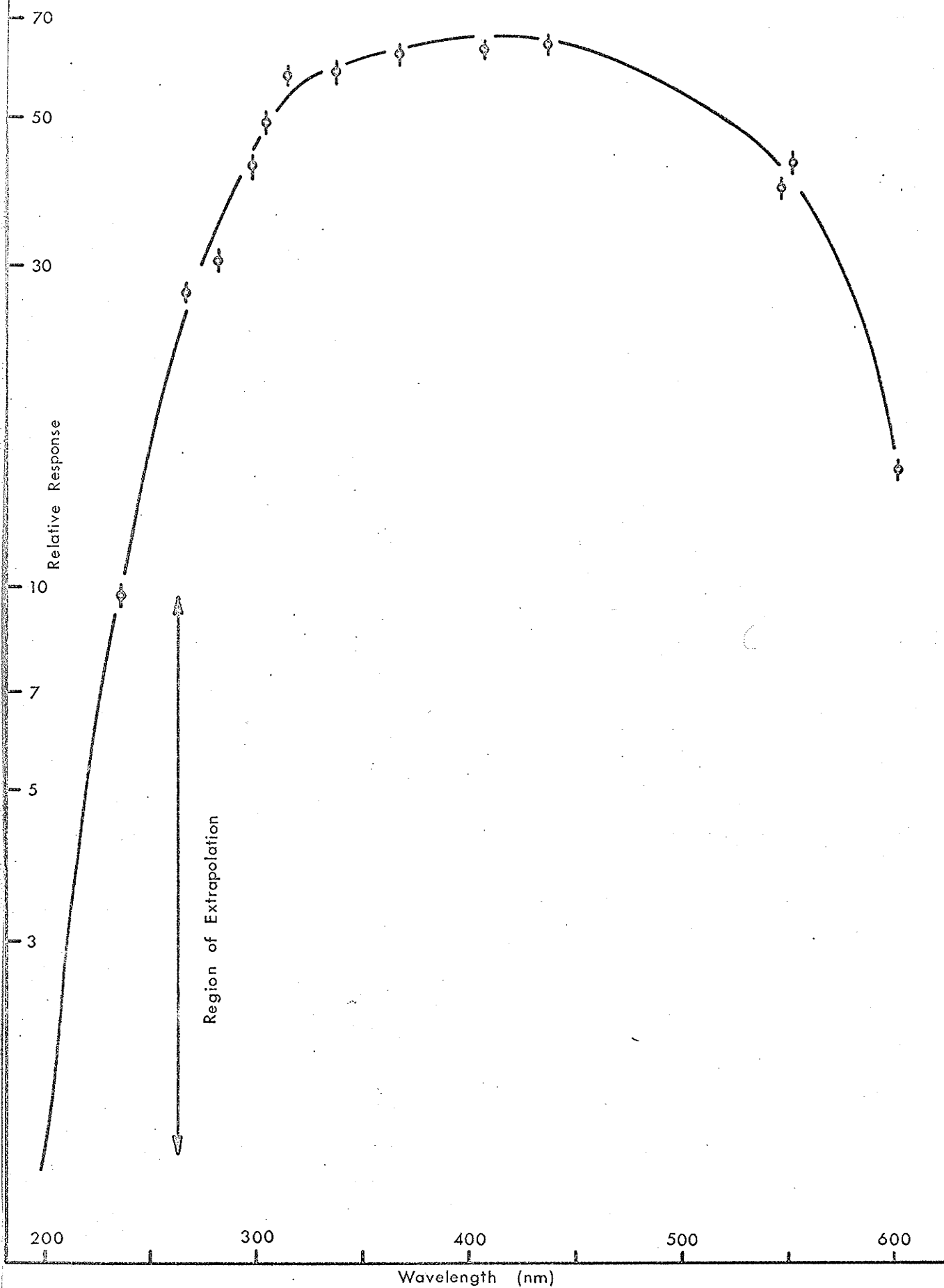
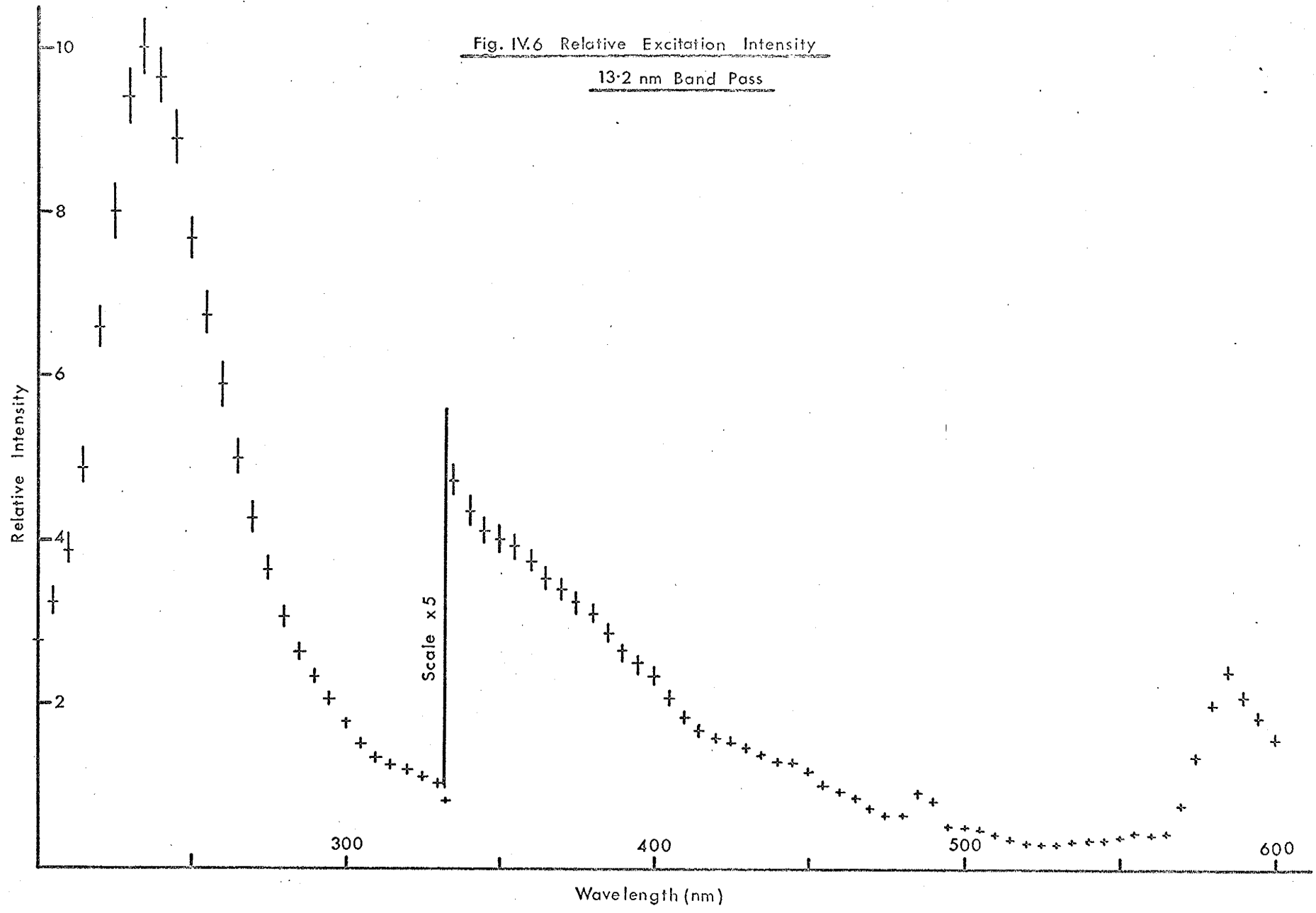


Fig. IV.6 Relative Excitation Intensity
13.2 nm Band Pass



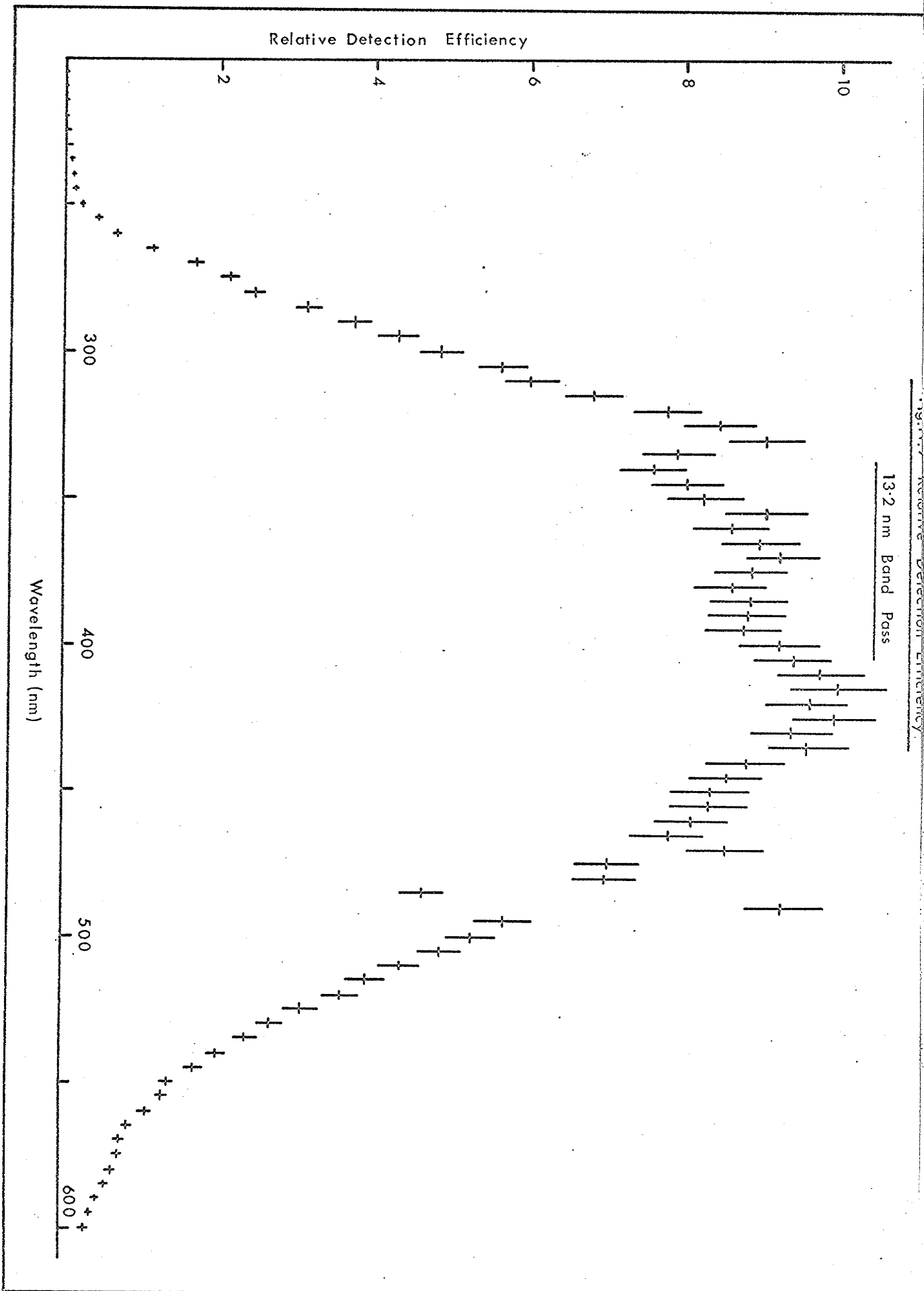
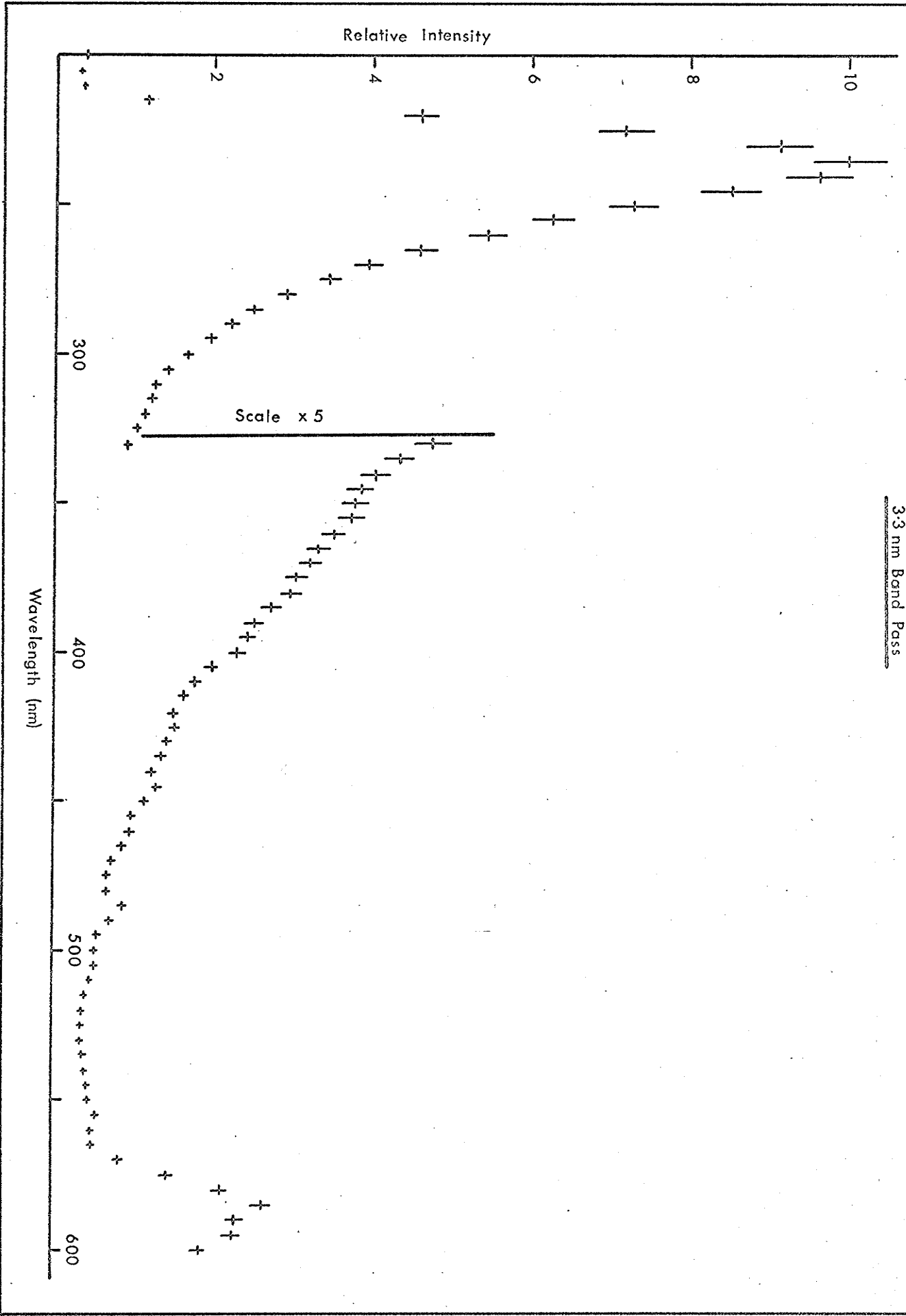
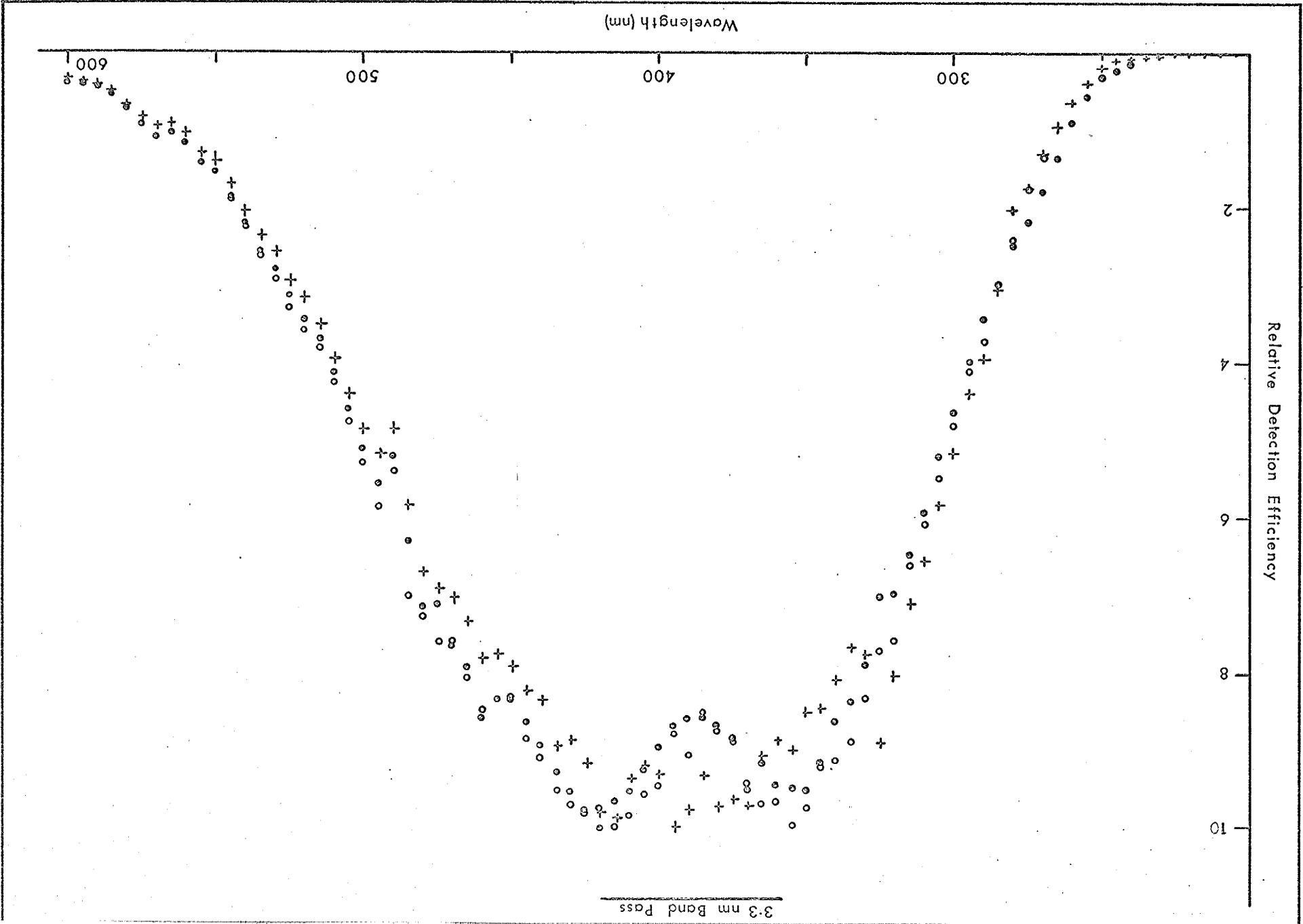


Figure 6 Relative Excitation Intensity
3.3 nm Band Pass



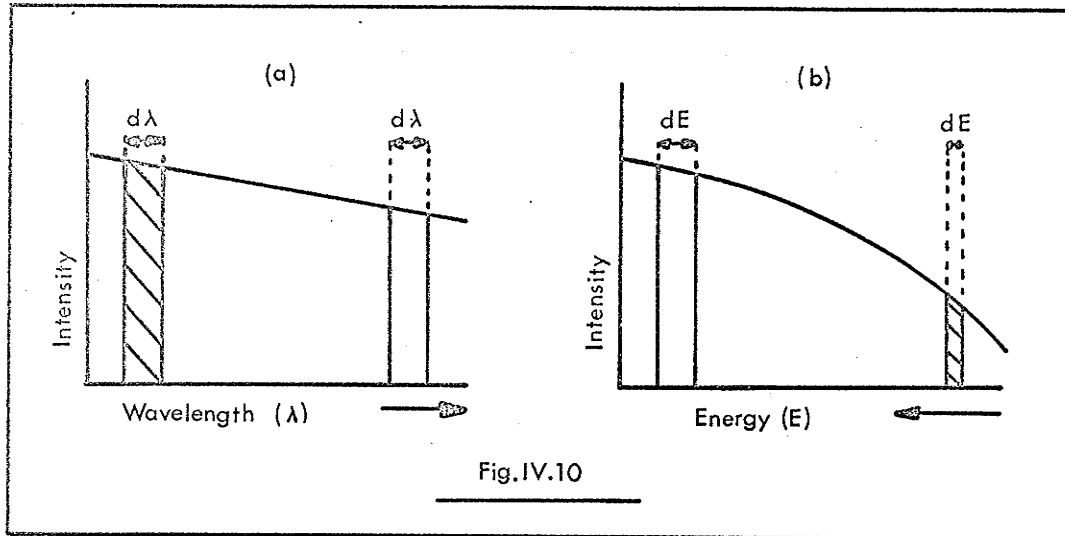


3.3 nm Band Pass

could be very tedious. In the past other workers have constructed ingenious automatic correction devices such as that of Lipsett (1959). His analogue system used cams, with profiles proportional to the instrument response curves, to drive a potential divider mounted in the photomultiplier output circuit. Correction of data pertaining to the present study, however, was greatly simplified by the use of paper tape output. The response curves were digitized at 50 Angstrom intervals and stored in a computer subroutine. Linear interpolation between the response curve data points made possible computer correction of any spectrum. Since luminescent curves are expected to be approximately Gaussian in energy (Chapter III), linear interpolation between the raw data points was used again to convert spectra having a linear wavelength scale to spectra having a linear energy scale. This conversion, conducted within the correction program, was made to facilitate the use of a Gaussian fitting program, discussed in Chapter VI.

(2) Slit Width Correction

The slit width of a grating monochromator controls the spectral band pass, which if measured in wavelength units is essentially constant over the spectral range of the instrument, as indicated by the shaded regions in Figure IV.10a. In converting from wavelength spectra to energy spectra, the width of the spectral "window" changes as seen in Figure IV.10b.



Consequently a correction must be applied for this change in energy bandpass. Now since curves IV.10a and IV.10b represent the same physical process, and the intensities I_a and I_b are the number of photons in a wavelength interval $d\lambda$ or energy interval dE involved in a transition per unit time, the area of the shaded elements must be identical. Hence:-

$$I_a d\lambda = I_b dE$$

where λ and E are related by:-

$$E = h\nu = hc/\lambda \quad (\text{with usual notation})$$

from which $d\lambda/dE = -hc/E^2$

so that $I_b \propto I_a \{1/E^2\}$

or equivalently, $I_b \propto I_a \{1/(h\nu)^2\}$

Thus to obtain a relative measure of the luminescence spectra in terms of the number of photons per unit energy interval, the raw data were corrected by applying a variable factor of $\{1/h\nu\}^3$.

(3) Temperature Determination

The thermocouple calibration curve, consisting of values at 10C⁰ intervals, was also stored in a computer program. Before and after each experiment, the thermocouple was recalibrated at liquid nitrogen and room temperatures, and the calibration curve appropriately rescaled. Linear interpolation was again employed to determine the crystal temperature from the corresponding thermocouple voltage.

The luminescence spectra were corrected, and the corresponding temperatures computed in a single program, written for the IBM 360/65 machine, and described in Appendix I.

CHAPTER V

EXPERIMENTAL DATA AND THEIR INTERPRETATION

(A) Introduction

In describing the excitation data, frequent reference will be made to the emission data which will be discussed later. At this point it is sufficient to mention that two broad emission peaks are seen, sometimes with a small peak between them.

To avoid confusion, the terms "band" and "envelope" will convey the following meanings unless specified otherwise:-

Band: An experimental peak to which a specific electronic transition has been assigned.

Envelope: An experimental peak that is the sum of several bands, or to which a specific transition has not been assigned.

Although a total of about 25 different NaI(Tl) samples were studied in all, only 11 were used to compile the data described in the following sections: 5 to obtain the excitation data, and 6 to obtain the emission data. In order to reduce the variation in Tl^+ concentration from one sample to another, the 11 samples used were cleaved from only 3 different large single crystals. In the following sections, the quoted sample numbers (1, 2 and 3) refer to the single crystals from which the samples were cleaved. Although the Tl^+ concentration will

be shown to differ among the large single crystals, samples from the same single crystal were found to be of similar Tl^+ content.

(B) Low Temperature Excitation Spectra

Figures V.1 to V.4 show excitation spectra of NaI(Tl) Sample #1 at a temperature of $97^{\circ}K$. The selected emission energies cover the ultraviolet-visible region from 2.75 eV (4500 Å) to 3.81 eV (3250 Å), spanning all the observed emission bands.

The excitation spectra giving rise to the low energy emission envelope in the vicinity of 2.88 eV (4300 Å) are presented in Figures V.1 and V.2: the former shows spectra at emission wavelengths within the low energy half of the envelope, while the latter shows spectra relating to the high energy side. Two excitation envelopes are seen, the larger in the region between 3.90 eV (3180 Å) and 4.36 eV (2840 Å) and the smaller between 4.46 eV (2780 Å) and 5.30 eV (2340 Å). The low energy excitation envelope appears to be comprised of at least two unresolved bands. Its peak height increases in Figure V.1 as the emission energy is increased and decreases in Figure V.2 as the emission energy is further increased. The increase and subsequent decrease in peak height was expected since the various emissions scan over the emission envelope. Although the peak position and width appear not to vary, they will be considered in more detail later.

The high energy excitation envelope appears to be triplet, as evidenced by the long shoulders, and will also be considered later in more detail. Its intensity variation with emission energy is more complex than that of the low energy excitation envelope due to its unresolved composite bands. The high energy side of the high energy envelope in Figure V.1 increases with increasing emission energy whilst the right hand side remains steady, and in Figure V.2 the low energy side of the envelope drops off somewhat more rapidly than does the high energy side.

In Figures V.3 and V.4 are shown the excitation spectra for emission over the range 3.26 eV (3800 Å) to 3.82 eV (3250 Å). Figure V.3 shows the spectra for excitation to the extreme high energy side of the low energy emission envelope, to a small band at 3.28 eV (3780 Å), and to the low energy side of the high energy emission envelope. The two excitation envelopes discussed in connection with Figures V.1 and V.2 are seen to decay progressively as the emission steps toward higher energies, whilst two new envelopes rise at 3.98 eV (3120 Å) and 4.68 eV (2650 Å).

Excitation to the high energy emission envelope is shown in Figure V.4. Although the transmission peak (marked T.P.) obscures somewhat the low energy region of the curves, the two excitation envelopes are much narrower than those related to excitation to the low energy emission band. The

FIGURE 1 POINTS INTERVAL - EVERY 2 POINT(S)
 GRAPH 1 (*) GRAPH 2 (+) GRAPH 3 (X) GRAPH 4 (.) GRAPH 5 (|)

EMISS/EXCIT ENERGY (eV.)	2.76	2.82	2.88	2.95
EMISS/EXCIT WAVELENGTH (Å)	4500	4400	4300	4200
TEMPERATURE (DEG. K)	97.	97.	97.	97.

DATA SCALED BUT NOT NORMALIZED

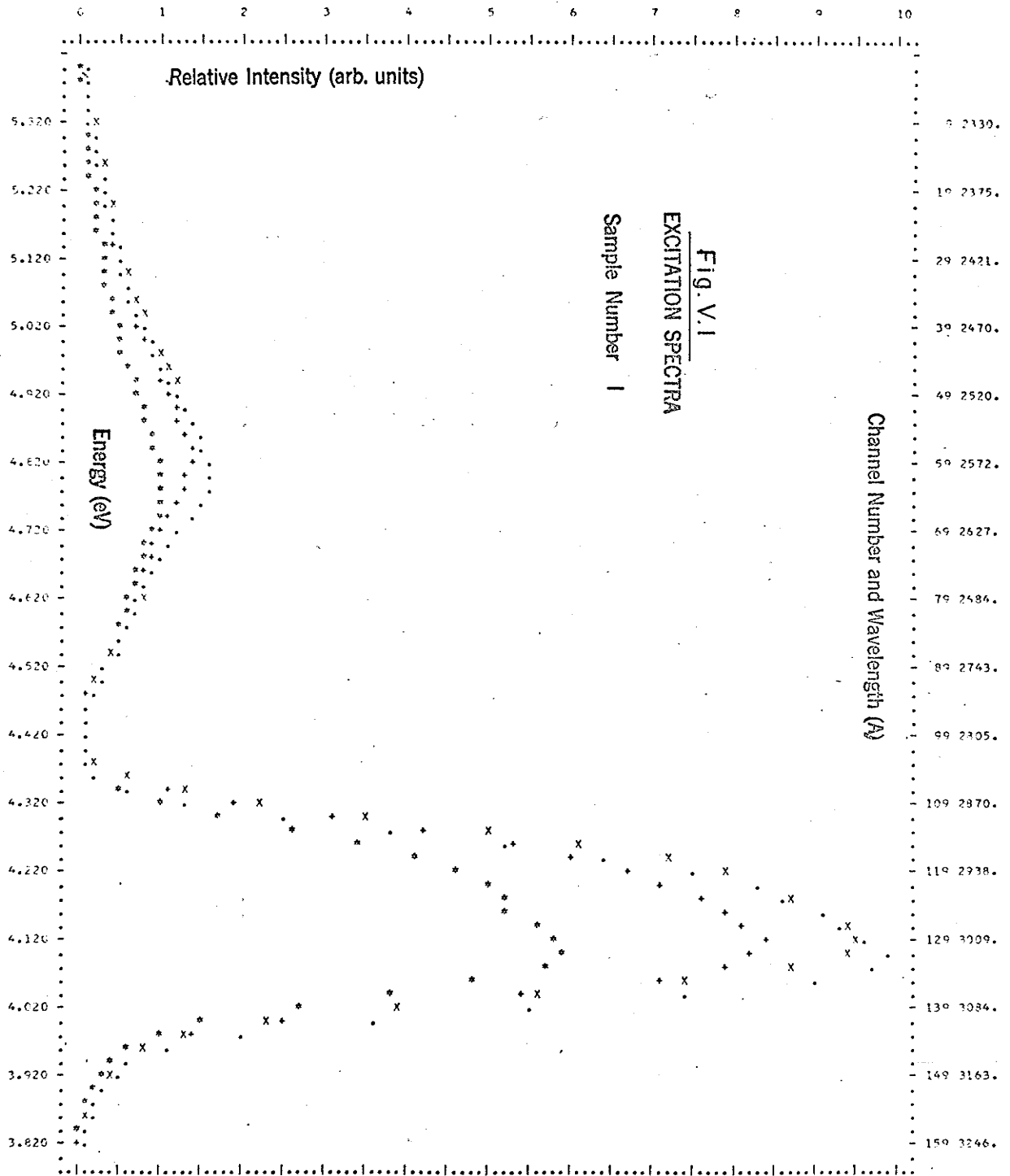


FIGURE 2 PLOTTING INTERVAL - EVERY 2 POINT(S)
 GRAPH 1 (*) GRAPH 2 (+) GRAPH 3 (X) GRAPH 4 (.) GRAPH 5 (I)

EMISS/EXCIT ENERGY (E.V.)	2.95	3.02	3.10	3.18	3.26
EMISS/EXCIT WAVELENGTH (Å)	4200	4100	4000	3990	3800
TEMPERATURE (DEG. K)	97.	97.	57.	97.	97.

DATA SCALED BUT NOT NORMALIZED

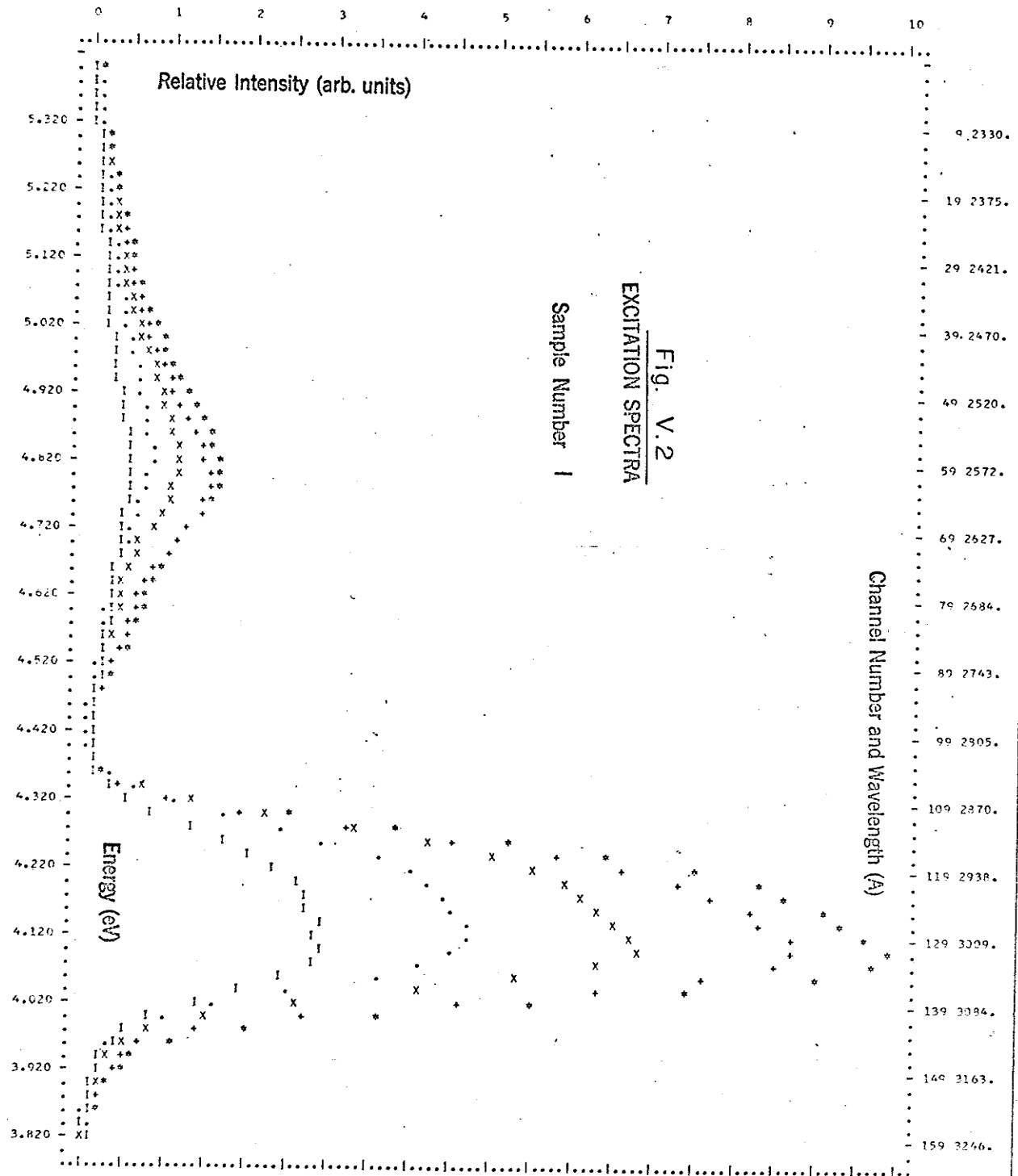


FIGURE 3

PLOTTING INTERVAL - EVERY 2 POINT(S)
GRAPH 1 (*) GRAPH 2 (+) GRAPH 3 (X) GRAPH 4 (.) GRAPH 5 (I)

EMISS/EXCIT ENERGY (E.V.) 3.26
EMISS/EXCIT WAVELENGTH (A) 3800
TEMPERATURE (DEG. K) 97.

3.44
3600
97.

3.54
3500
97.

3.59
3450
97.

DATA SCALED BUT NOT NORMALIZED

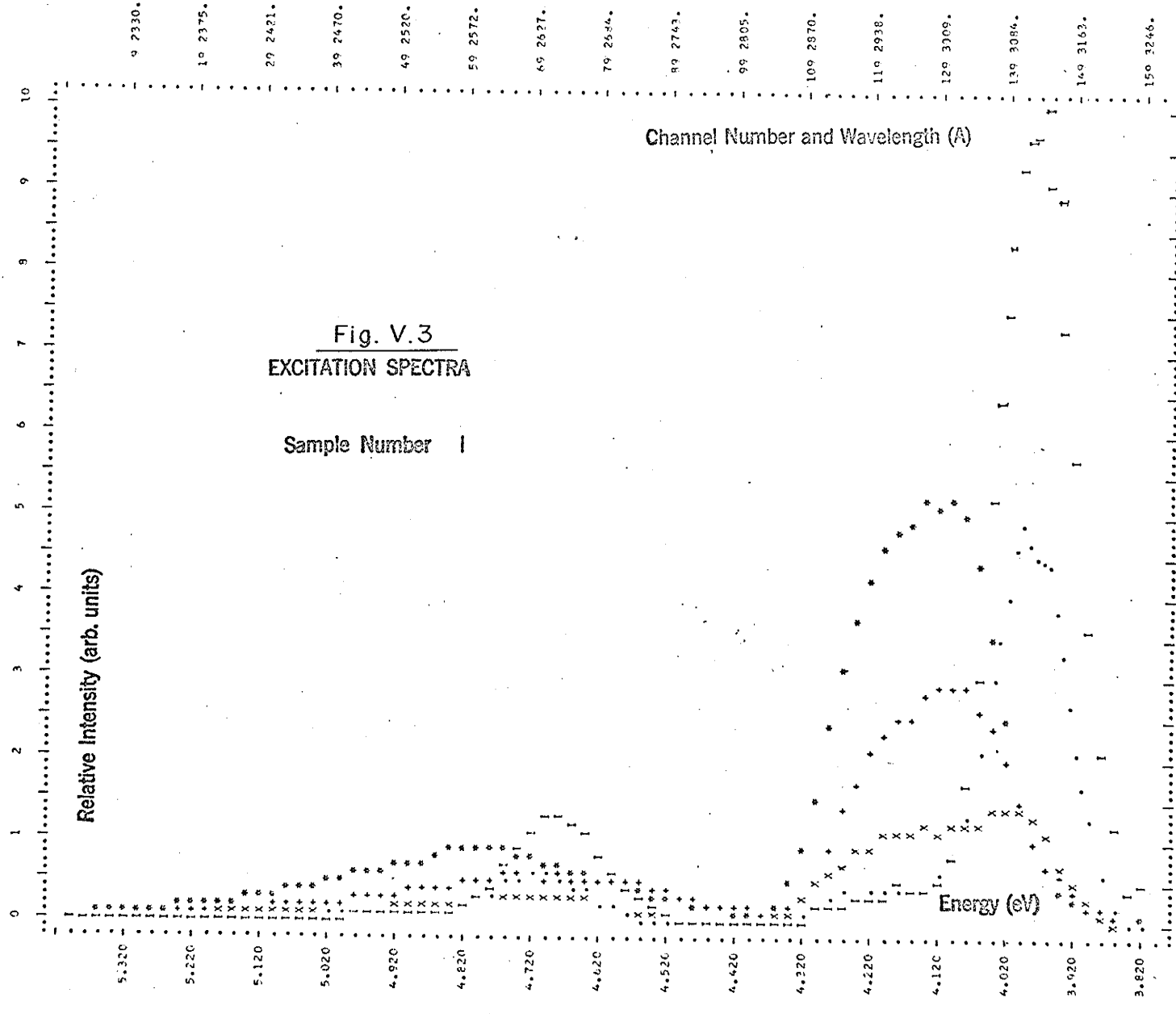


FIGURE 4 PLOTTING INTERVAL - EVERY 2 POINT(S)
 GRAPH 1 (*) GRAPH 2 (+) GRAPH 3 (X) GRAPH 4 (.) GRAPH 5 (I)

EMISS/EXCIT ENERGY (E.V.)	3.59	3.65	3.70	3.76	3.81
EMISS/EXCIT WAVELENGTH (A)	3450	3400	3350	3300	3250
TEMPERATURE (DEG. K)	97.	97.	97.	97.	97.

DATA SCALED BUT NOT NORMALIZED

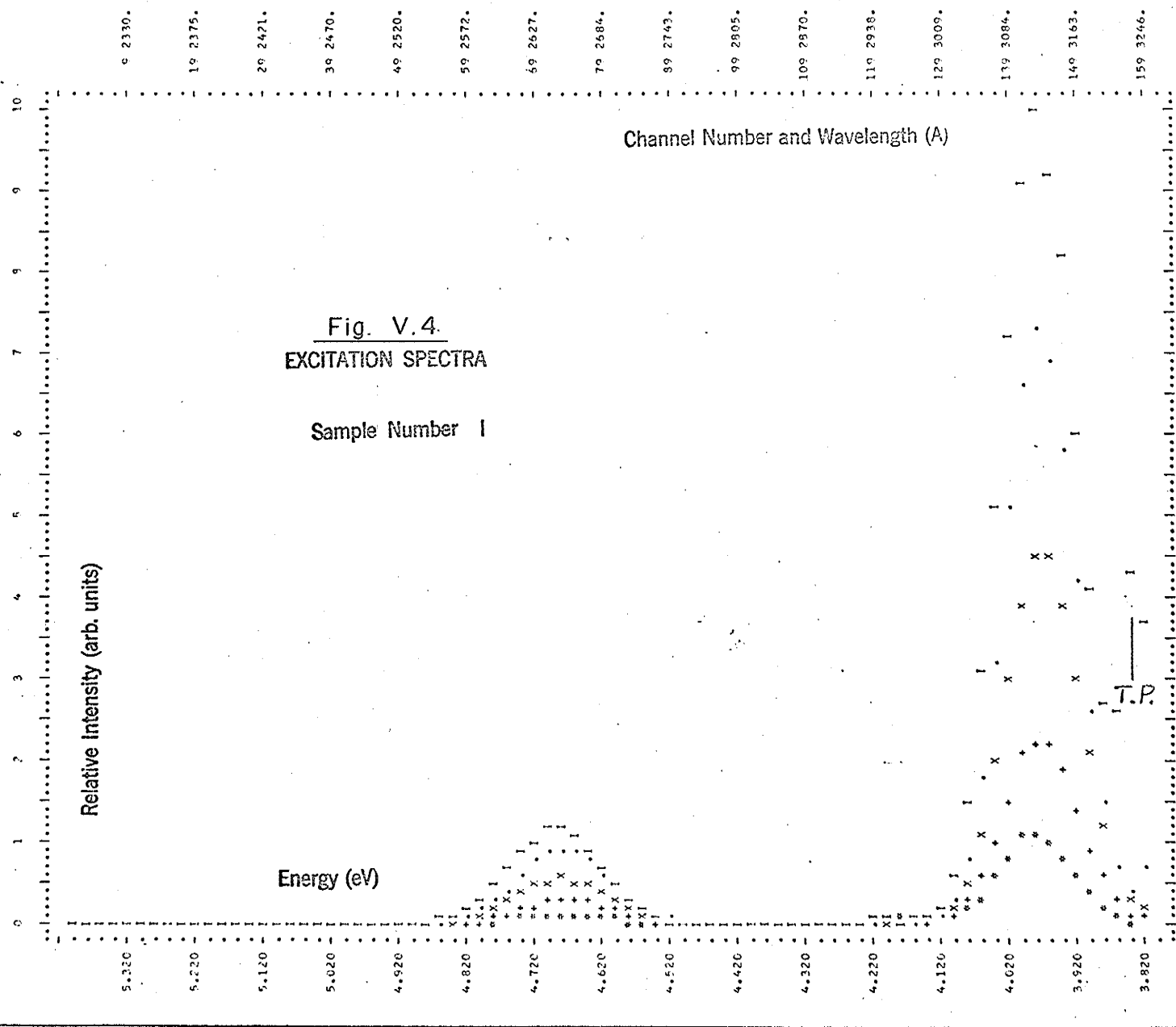
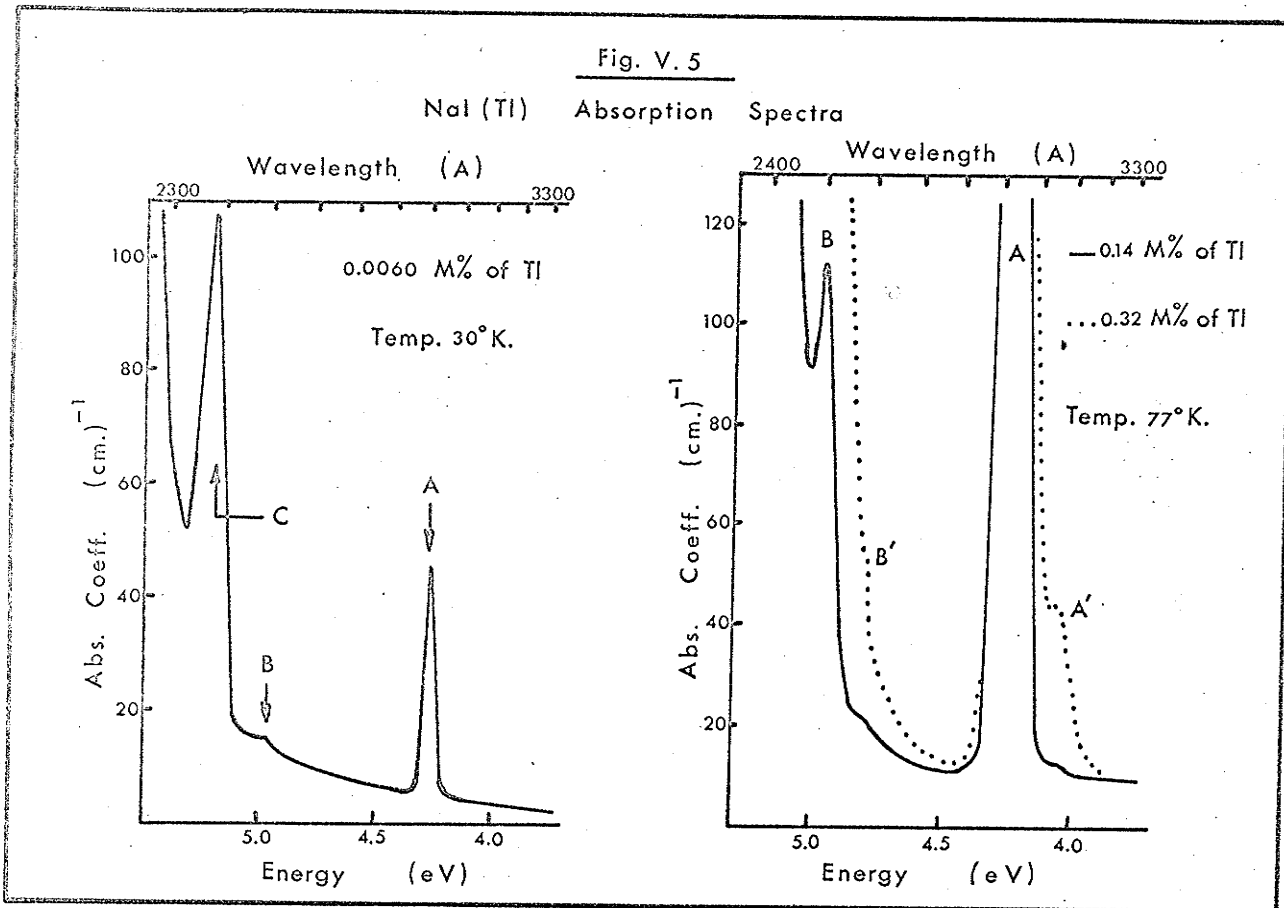


Fig. V.4.
 EXCITATION SPECTRA
 Sample Number 1

Fig. V. 5

NaI (Tl) Absorption Spectra



fine structure indicated in the narrow low energy envelope of Figure V.3, and the movement of both envelopes in Figure V.4 suggests that both may be comprised of more than one unresolved band. However the small peak shift may result not from an actual movement of the excitation envelope, but from an error in the reproducibility of the wavelength range scanned by the monochromator. As will be seen later, both effects are present, but one may be distinguished from the other in certain circumstances.

The major features of the above low temperature excitation

data may be interpreted in the light of the absorption spectra of NaI(Tl) taken by Matsui (1967) and reproduced in Figure V.5. The spectra of samples containing various Tl^+ concentrations show the A and B bands characteristic of the Tl^+ monomer absorption, the B band resolved from the fundamental absorption edge only at temperatures equal to, or below, that of liquid nitrogen. At the higher Tl^+ concentrations, absorption bands due to the dimer centre appear in the low energy shoulders of the A and B bands. These will be called the A' and B' bands respectively. The positions of the A, B, C, A' and B' bands (Matsui, 1967) are:-

Band	Position		Temperature °K
	eV	A	
A	4.26	2910	77
A'	4.06	3050	77
B	4.96	2500	77
B'	4.81	2575	77
C	5.22	2376	30

In addition to the absorption bands listed above, there may exist a C' band not seen in Figure V.5 since it would lie under the fundamental absorption edge.

In the present excitation data for a temperature of 97°K, two broad and asymmetrical envelopes are seen, together with two narrower ones on their low energy sides. Accordingly, the broad low energy asymmetrical excitation envelope at 4.14 eV (2990 Å) is associated with the A band of the monomer centre, and the other broad envelope at 4.80 eV (2580 Å) is associated

with the B band and possibly also with the C band. The narrow low energy excitation band at 3.98 eV (3120 Å) is associated with the A' band, and the other excitation envelope at 4.68 eV (2650 Å) with the B' band.

The internal structure of the A' excitation band was confirmed by similar spectra taken on Sample #2, which has a somewhat higher Tl^+ concentration than Sample #1. Figure V.6 shows the fine structure, and Figures V.7, V.8 and V.9 show the continued increase in peak height of both dimer bands as the energy of emission encroaches more and more into the high energy envelope. Figure V.6 shows the fine structure to be most prominent when both the A and A' bands are present. The shift in peak position of the A' band may be due either to varying heights of fine structure components or to a wavelength error. The variation in shape and position of the high energy excitation envelope is quite obvious in Figures V.6, V.7, V.8, and V.9, and will be discussed at a more appropriate time. Both Figures V.8 and V.9 show the transmission peak at the extreme right hand side.

FIGURE 6 PLOTTING INTERVAL - EVERY 2 POINT(S)
 GRAPH 1 (*) GRAPH 2 (+) GRAPH 3 (X) GRAPH 4 (.) GRAPH 5 (I)

EMISS/EXCIT ENERGY (E.V.)	3.48	3.50	3.52	3.56
EMISS/EXCIT WAVELENGTH (A)	3500	3540	3520	3480
TEMPERATURE (DEG. K)	95.	95.	95.	95.

DATA SCALED BUT NOT NORMALIZED

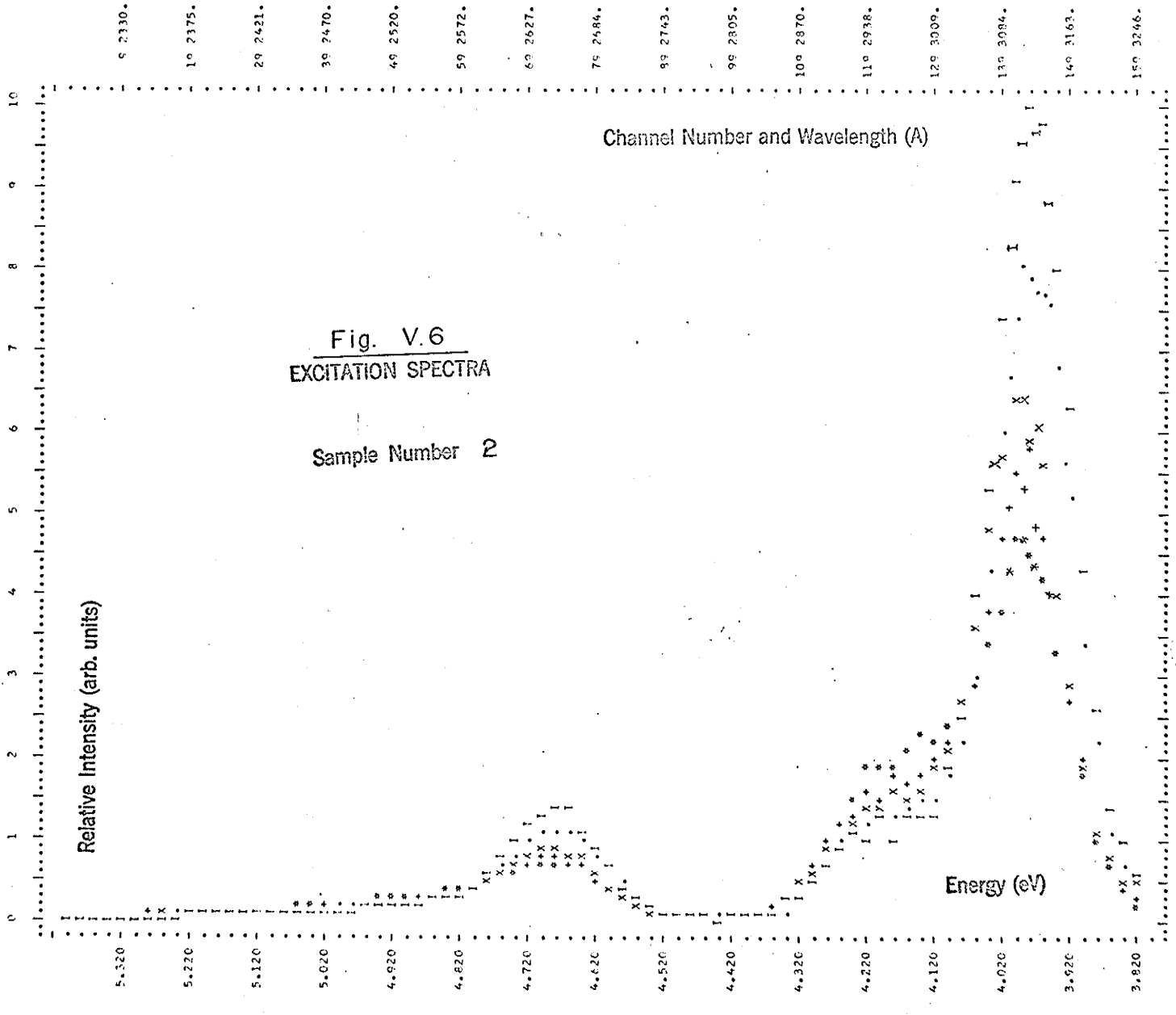


FIGURE 7

PLOTTING INTERVAL - EVERY 2 PRINT(S)

	GRAPH 1 (*)	GRAPH 2 (+)	GRAPH 3 (X)	GRAPH 4 (.)	GRAPH 5 (I)
EMISS/EXCIT ENERGY (e.v.)	3.56	3.56	3.60	3.63	3.65
EMISS/EXCIT WAVELENGTH (A)	3480	3460	3440	3420	3400
TEMPERATURE (DEG. X)	95.	95.	95.	95.	95.

DATA SCALED BUT NOT NORMALIZED

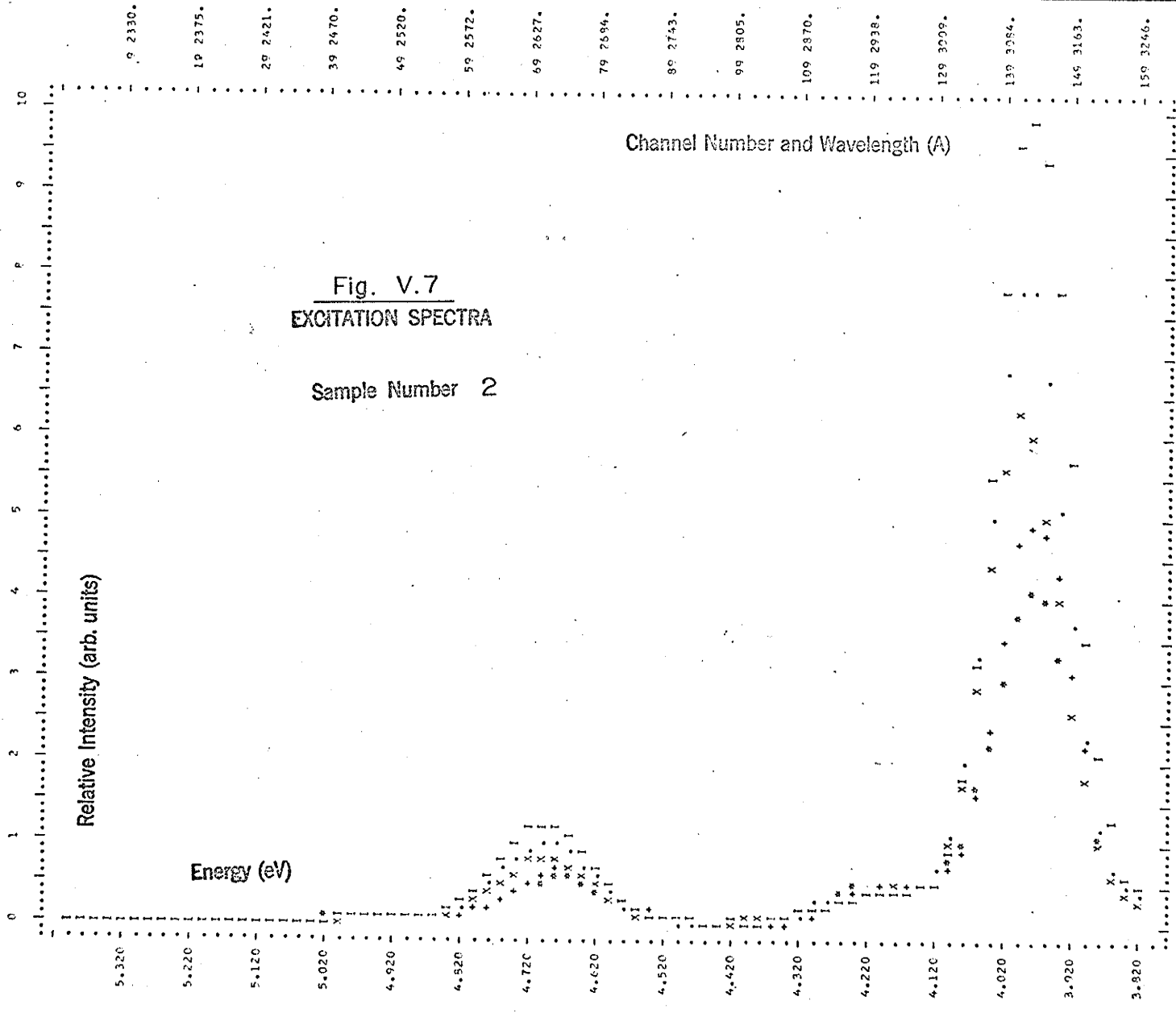


FIGURE 8 PLOTTING INTERVAL - EVERY 2 POINT(S)
 GRAPH 1 (*) GRAPH 2 (+) GRAPH 3 (X) GRAPH 4 (.) GRAPH 5 (I)

EMISS/EXCIT ENERGY (E.V.)	3.65	3.67	3.69	3.71	3.73
EMISS/EXCIT WAVELENGTH (A)	3400	3380	3360	3340	3320
TEMPERATURE (DEG. K)	95.	95.	95.	95.	95.

DATA SCALED BUT NOT NORMALIZED

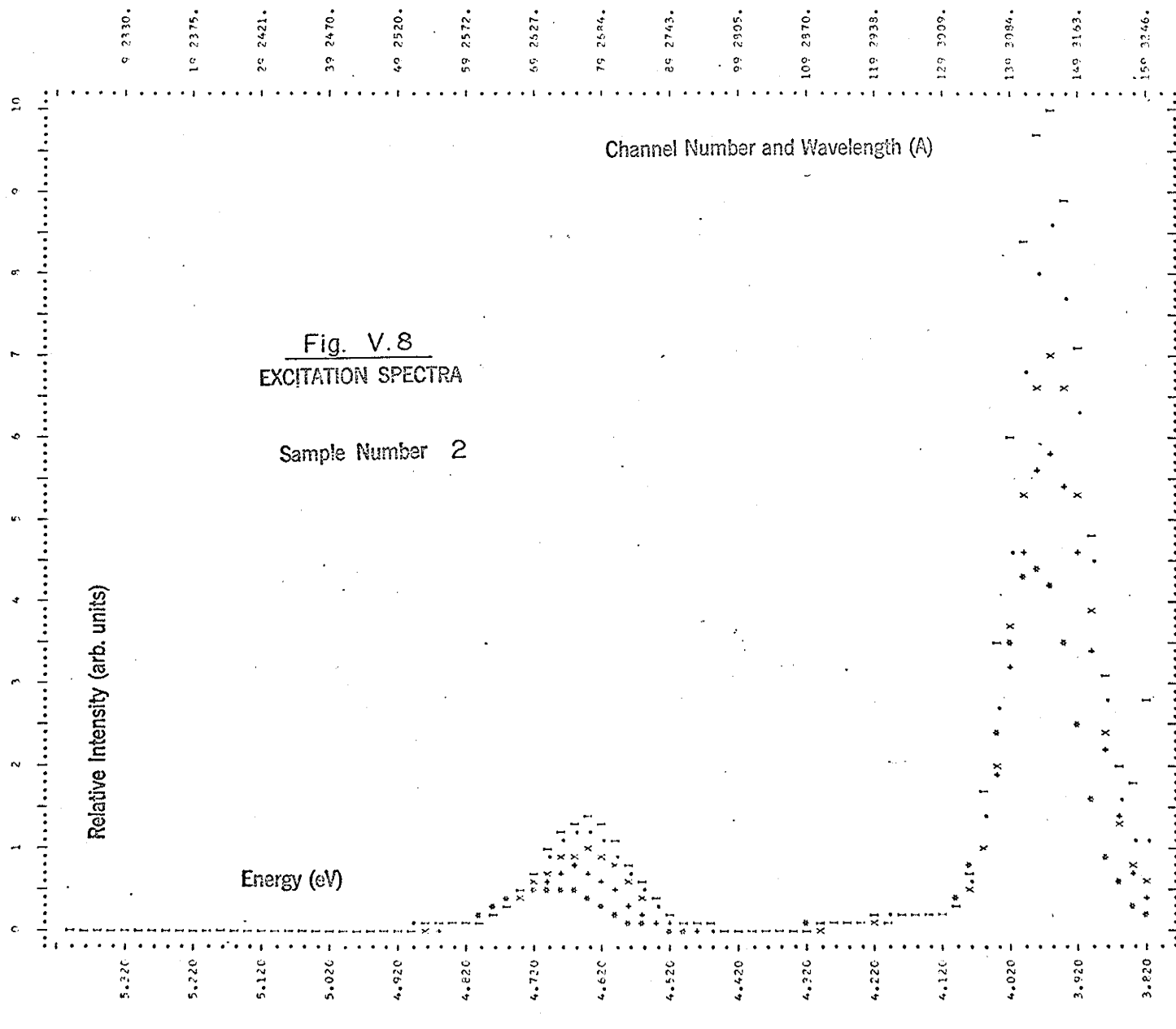


Fig. V.8
 EXCITATION SPECTRA
 Sample Number 2

FIGURE 9

PLOTTING INTERVAL - EVERY 2 POINT(S)

GRAPH 1 (*) GRAPH 2 (+) GRAPH 3 (x) GRAPH 4 (.) GRAPH 5 (I)

EMISS/EXCIT ENERGY (E.V.) 3.75 3.76 3.78 3.80 3.87

EMISS/EXCIT WAVELENGTH (A) 3320 3300 3280 3280 3240

TEMPERATURE (C.G. K) 95. 95. 95. 95. 95.

DATA SCALED BUT NOT NORMALIZED

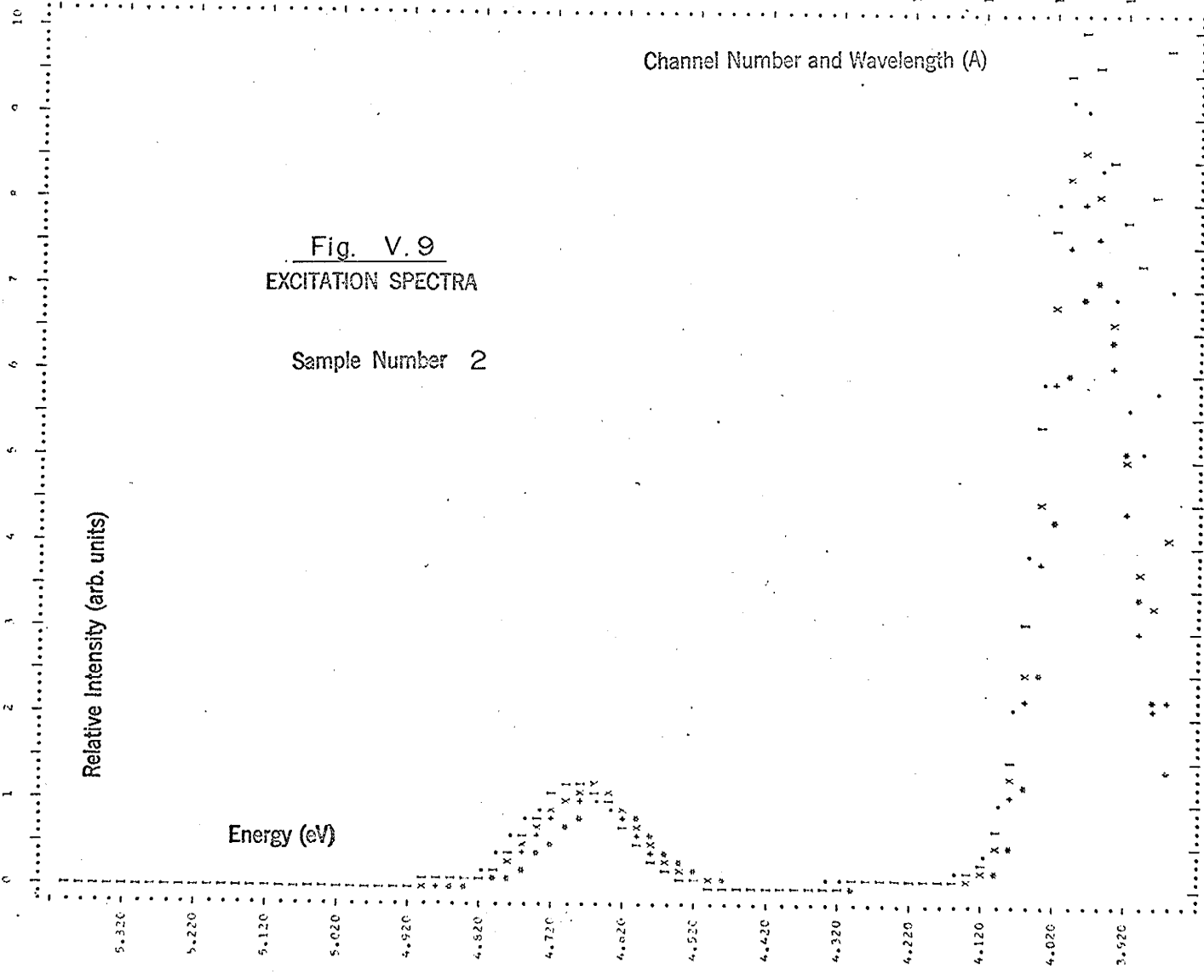


Fig. V.9
EXCITATION SPECTRA

Sample Number 2

(C) Low Temperature Excitation Envelope Shapes

Figures V.10 and V.11 show a selection of excitation curves of Sample #1 for emissions that span the entire low energy emission envelope. Since for an excitation curve the peak height of the low energy envelope is much larger than that of the high energy one, both cannot conveniently be drawn to the same scale on one graph. Thus, part (a) of each figure shows the high energy envelopes and part (b) the low energy envelopes, both sets separately normalized so that the largest peak fills the vertical dimension of each diagram.

The curves of Figures V.10a and V.11a show the high energy excitation envelope to be at least triplet, consisting of a central band flanked by a smaller one on either side. As the emission steps from 2.76 eV (4500 Å) to 3.02 eV (4100 Å), the central peak of the triplet at first rises and then falls, whilst the right hand peak remains at a fairly constant height. For emissions between 3.02 eV (4100 Å) and 3.18 eV (3900 Å) both the central and right hand components decrease, and at still higher energy emissions, a new band is seen at about 4.56 eV (2720 Å), in the low energy tail of the envelope. The rise of this band is maintained in Figure V.12a for emissions up to 3.35 eV (3700 Å), after which it decreases rapidly as the energy of emission increases still further. Since this peak appears on the low energy side of the 4.68 eV (2650 Å) B' band, and well removed from the A band region, it cannot be

identified with an electronic transition within either the dimer or the monomer centre. This band will be called the I' band.

In ascending order of energy, the Tl^+ (or $(Tl^+)_2$) ion absorption or excitation bands that lie on the high energy side of the B' band are the B, C', and C bands. Returning to Figures V.10a and V.11a, the B' band position lies midway between the central and the low energy components of the triplet envelope. Further, in Figure V.12a both the central and the high energy components are seen to decay as the B' band rises, indicating that they are bands related to the monomer centre. That is, the central component at 4.80 eV (2580 Å) of Figures V.10a and V.11a is associated with the B absorption band, while the high energy component at 5.12 eV (2420 Å) can be identified as the C band. The small tail on the high energy side of the B' band of Figure V.12a may in fact be the C' band.

Assuming that the dimer centre results from two Tl^+ ions in nearest neighbour cation positions, and that the probability of occupation of all positive ion sites by Tl^+ ions is the same, then the number of dimer centres per unit volume is:-

$$N_d \approx 6N_m^2/N^2$$

(Van Sciver, 1964), where N_m is the number of monomer centres per unit volume, N is the number of available ionic sites per

unit volume, and $N_m \ll N$. Thus for a monomer concentration of 1 part per 10^3 (i.e. $N_m/N \approx 10^{-3}$), the dimer concentration is approximately 6 parts per 10^6 . Although the dimer/monomer population ratio is of the order of 6×10^{-3} , the excitation spectra of Figure V.12 show the B' and B bands, and the A' and A bands, to be of comparable intensity. Thus the efficiency of luminescence of the dimer centre must be approximately 100 times that of the monomer centre.

In Figure V.10 and V.11 the A band shape changes little as the emission energy increases. The point of inflection at the A band peak (4.14 eV) was observed by Matsui (1967) and although no clear explanation was given, the inflection was interpreted by the present author in the light of the experimental arrangement used. The technique was to view the crystal luminescence in a direction perpendicular to the direction of excitation, and to mount a large square sample with its face perpendicular to the exciting beam. At high absorption coefficients, for example in the A band at 4.14 eV, the exciting beam would be absorbed predominantly in a thin surface layer of the crystal. This thin layer would be off the axis of the analyser monochromator, and could result in a distortion of the excitation band shape.

The present experimental arrangement, using a 45° crystal orientation, avoids this problem, since the source of luminescent emission is always mounted on the axis of the

analyser monochromator. The fact that the point of inflection is still observed suggests that a different explanation is required.

At the higher excitation energies of Figure V.11b, the curves are more bell-shaped over the peaks than are the curves of Figure V.10b. This suggests that the envelope consists of two overlapping bands, the relative intensity of which changes as the emission energy varies. The small variation in the position of the envelope is apparently random, but is about twice as large as the estimated experimental error of ± 4 Angstrom, and may also imply internal structure of the A band.

Over the emission range where the B and C bands of Figure V.12a decay and the B' band rises, Figure V.12b shows similar drastic changes in the shape of the low energy envelope. The A excitation band decays, and is replaced at slightly lower energy by the A' band.

In Figure V.13, data showing the shape of the excitation bands for emissions contained solely within the high energy emission region are presented somewhat differently from the previous three figures, so that the peak movements can be investigated. For various emission energies, part (a) shows the high energy B' band; part (b) shows the same curves all normalized to an identical peak height; and part (c) shows, for the same emissions, the low energy A' bands normalized to

the same peak height. Both the high and low energy excitation bands are symmetrical and do not show internal structure as the emission energy varies. In addition, the relative displacement among the curves in Figure V.13b is the same as that in Figure V.13c, suggesting that a systematic error within the range ± 4 Angstrom is associated with the wavelength scale of each graph, in agreement with the estimate made in Chapter IV. The small shoulder at 4.91 eV (2520 A) on the high energy side of the B' band in Figures V.13a and V.13b may be the C' band, but is more likely a small residue from the B band. If it were the C' band it would be expected to increase along with the B' band, as the emission energy increases.

FIGURE 10A PLOTTING INTERVAL - EVERY 1 PRINT(S)
 GRAPH 1 (*) GRAPH 2 (+) GRAPH 3 (X) GRAPH 4 (.) GRAPH 5 (I)

EMISS/EXCIT ENERGY (eV) 2.76 2.82 2.88 2.95
 EMISS/EXCIT WAVELENGTH (Å) 4500 4200 4000 3970
 TEMPERATURE (DEG. C) 97. 97. 97. 97.

DATA SCALED BUT NOT NORMALIZED

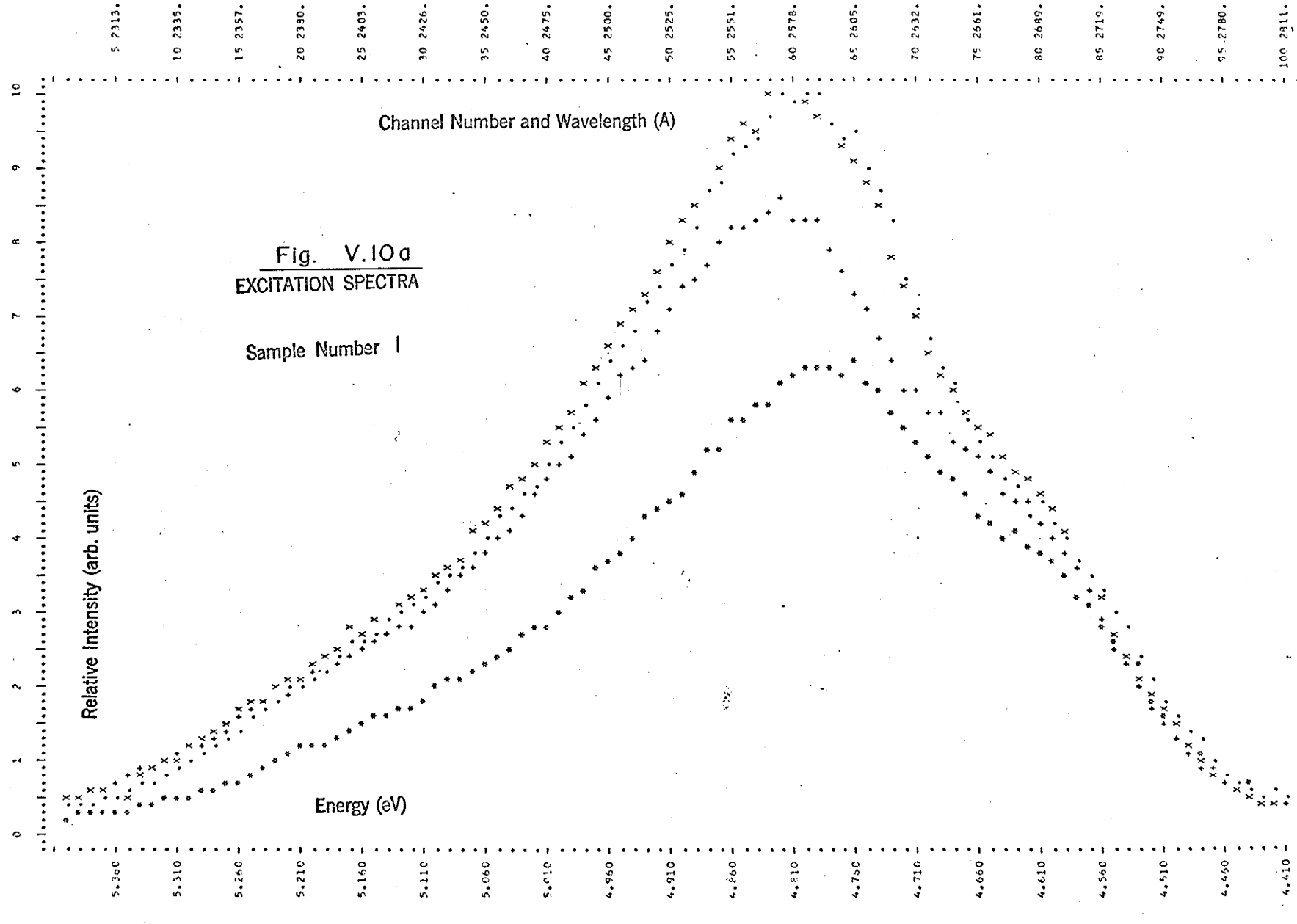


FIGURE 108 PLOTTING INTERVAL - EVERY 1 POINT(S)

	GRAPH 1 (*)	GRAPH 2 (**)	GRAPH 3 (X)	GRAPH 4 (.)	GRAPH 5 (I)
EMISS/EXCIT ENERGY (E.V.)	2.76	2.82	2.88	2.95	
EMISS/EXCIT WAVELENGTH (A)	4500	4400	4300	4200	
TEMPERATURE (DEG. X)	97.	97.	97.	97.	

DATA NORMALIZED AND SCALED

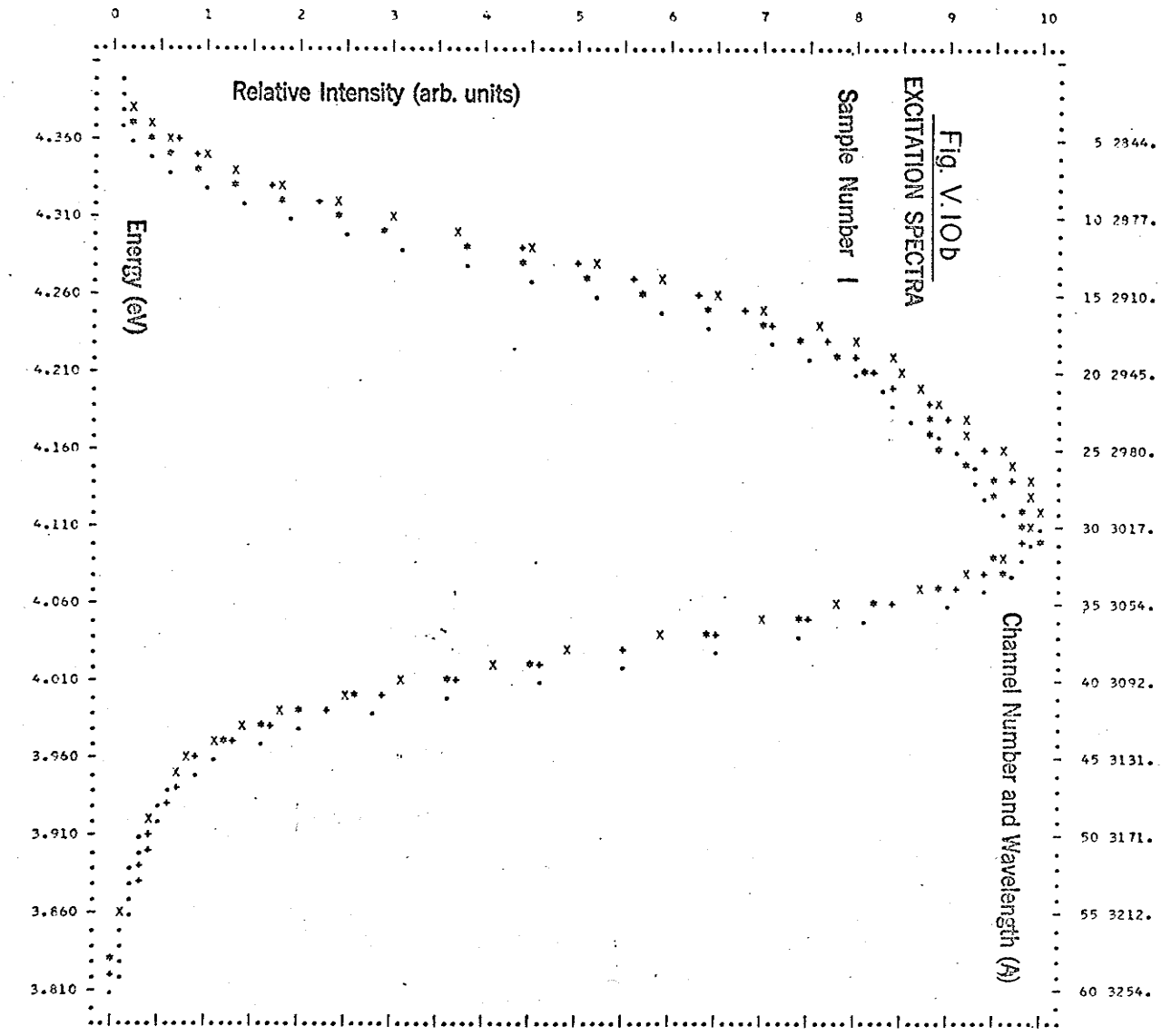


FIGURE 11A PLOTTING INTERVAL - EVERY 1 POINT(S)
 GRAPH 1 (*) GRAPH 2 (+) GRAPH 3 (X) GRAPH 4 (.) GRAPH 5 (I)

EMISS/EXCIT ENERGY (E.V.)	7.95	3.02	3.10	3.14	3.26
EMISS/EXCIT WAVELENGTH (Å)	4200	4100	4000	3900	3800
TEMPERATURE (DEG. K)	97.	97.	97.	97.	97.

DATA SCALED BUT NOT NORMALIZED

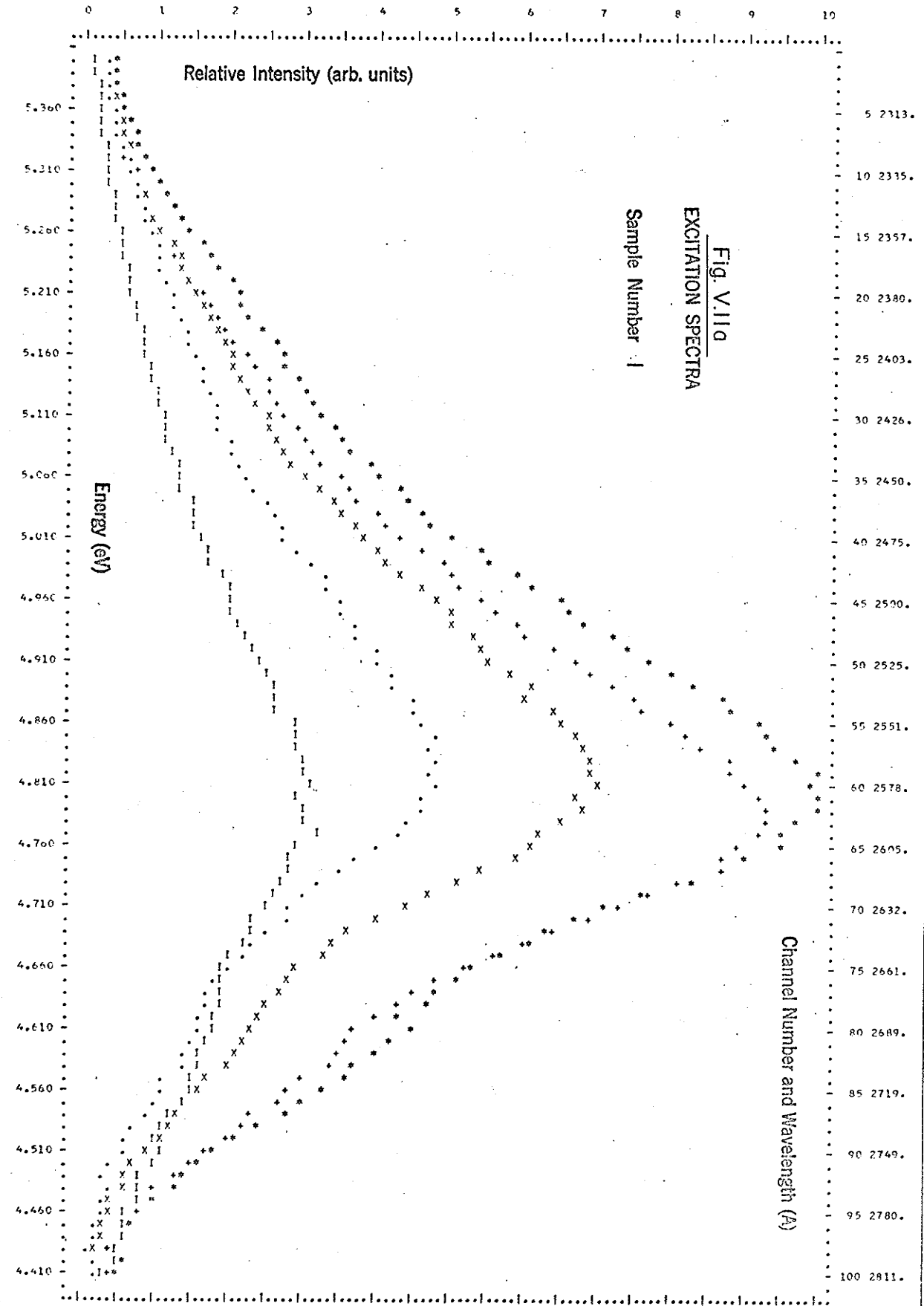


FIGURE 118 PLOTTING INTERVAL - EVERY 1 POINT(S)

	GRAPH 1 (*)	GRAPH 2 (+)	GRAPH 3 (X)	GRAPH 4 (.)	GRAPH 5 (I)
EMISS/EXCIT ENERGY (E.V.)	2.95	3.02	3.10	3.18	3.26
EMISS/EXCIT WAVELENGTH (Å)	4200	4100	4000	3900	3800
TEMPERATURE (DEG. K)	97.	97.	97.	97.	97.

DATA NORMALIZED AND SCALED

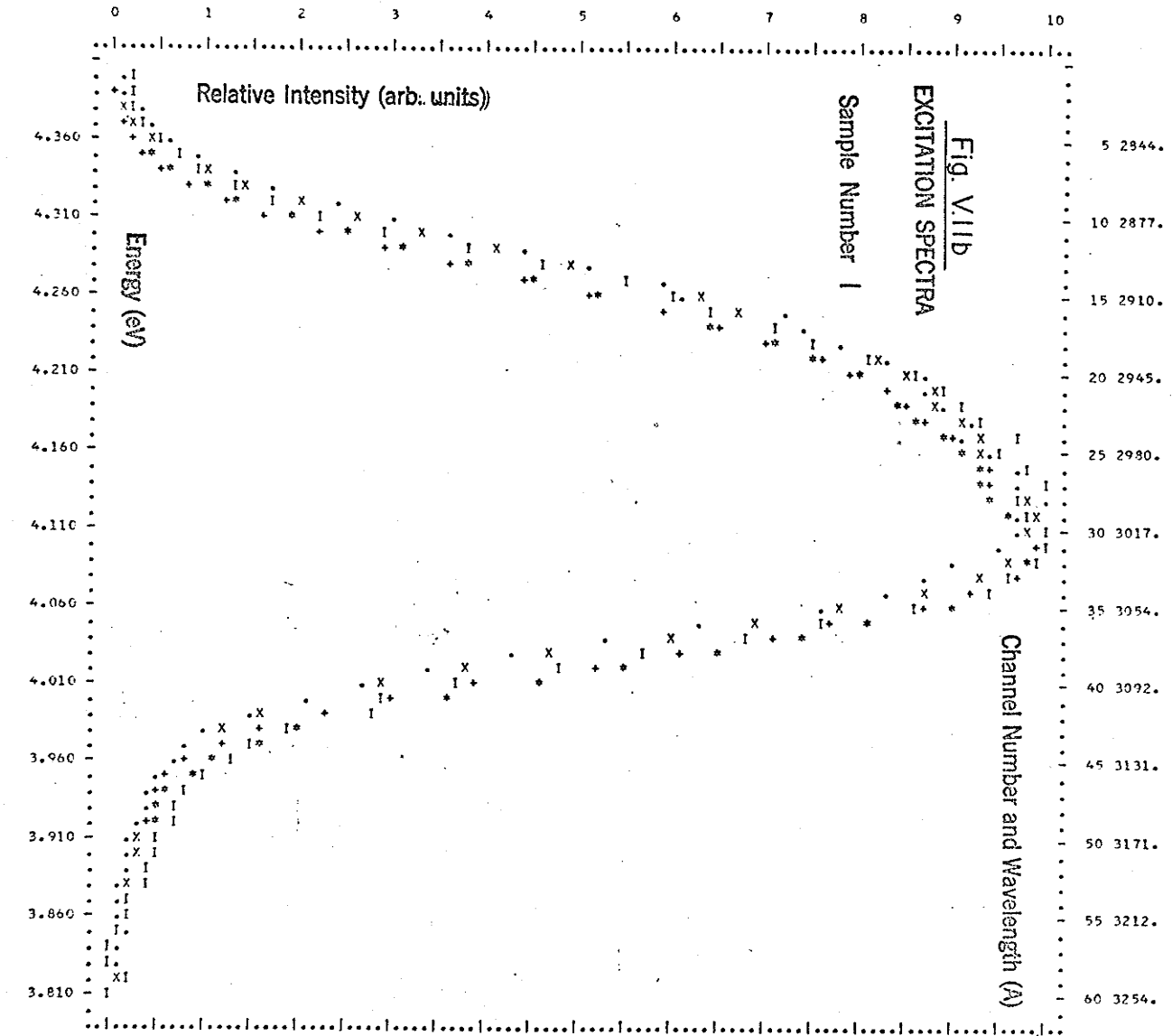


FIGURE 3.13 ELECTRIC FIELD - EVERY 1 POINT(S)
 GRAPH 1 (A) GRAPH 2 (A) GRAPH 3 (V) GRAPH 4 (A) GRAPH 5 (I)

WISSECHT ENERGY (eV)	3.26	3.95	3.44	3.54	3.59
WISSECHT WAVELENGTH (Å)	3800	3700	3600	3500	3450
TEMPERATURE (DEG. K)	97.	97.	97.	97.	97.

DATA SCALED OUT NOT NORMALIZED

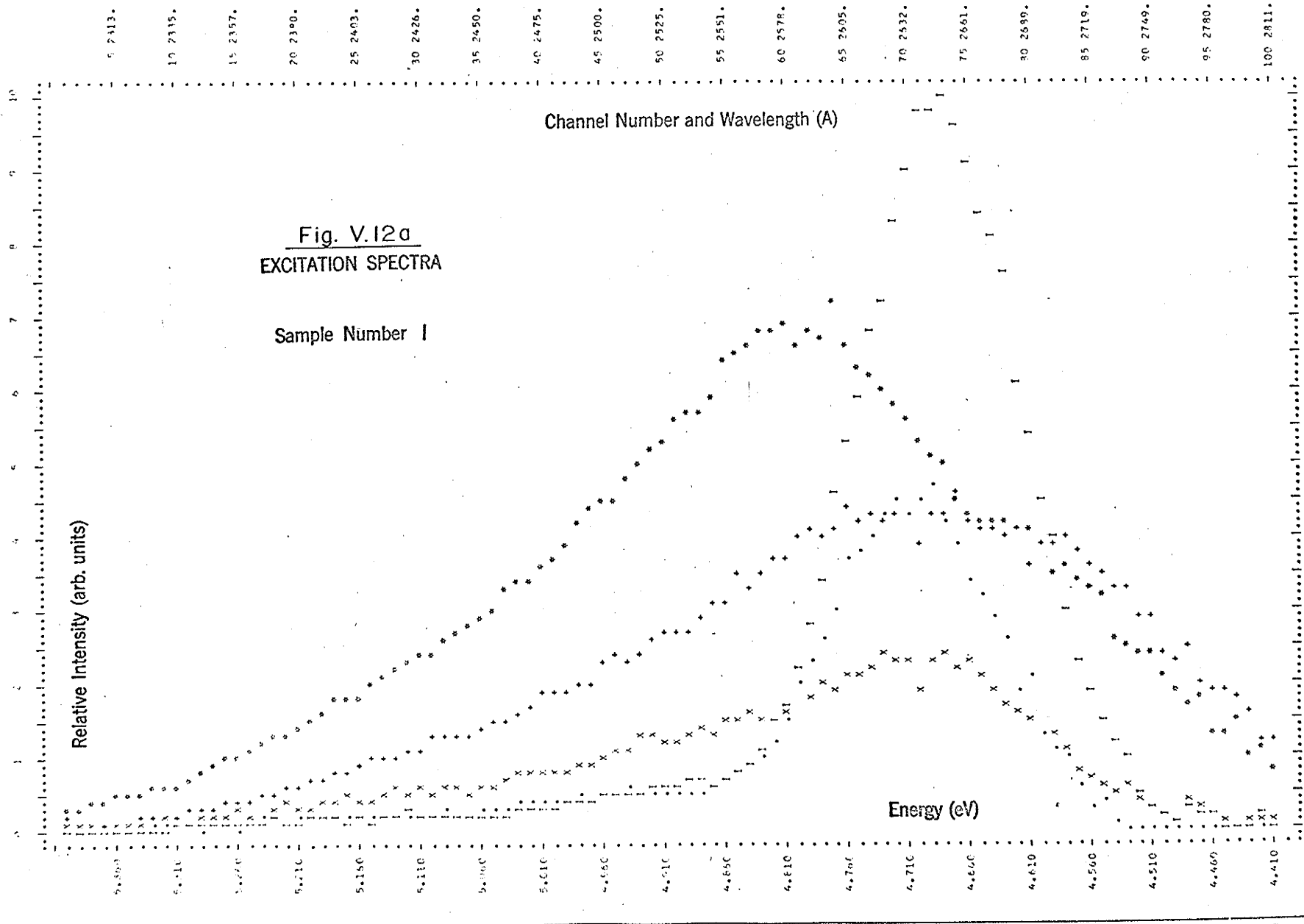


FIGURE 12B

PLOTTING INTERVAL - EVERY 1 POINT(S)

GRAPH 1 (+)	GRAPH 2 (+)	GRAPH 3 (X)	GRAPH 4 (+)	GRAPH 5 (I)
3.26	3.35	3.44	3.54	3.59
3000	3700	3600	3500	3450
97.	97.	97.	97.	97.

EMISS/EXCIT ENERGY (E.V.)
 EMISS/EXCIT WAVELENGTH (A)
 TEMPERATURE (DEG. K)

DATA NORMALIZED AND SCALED

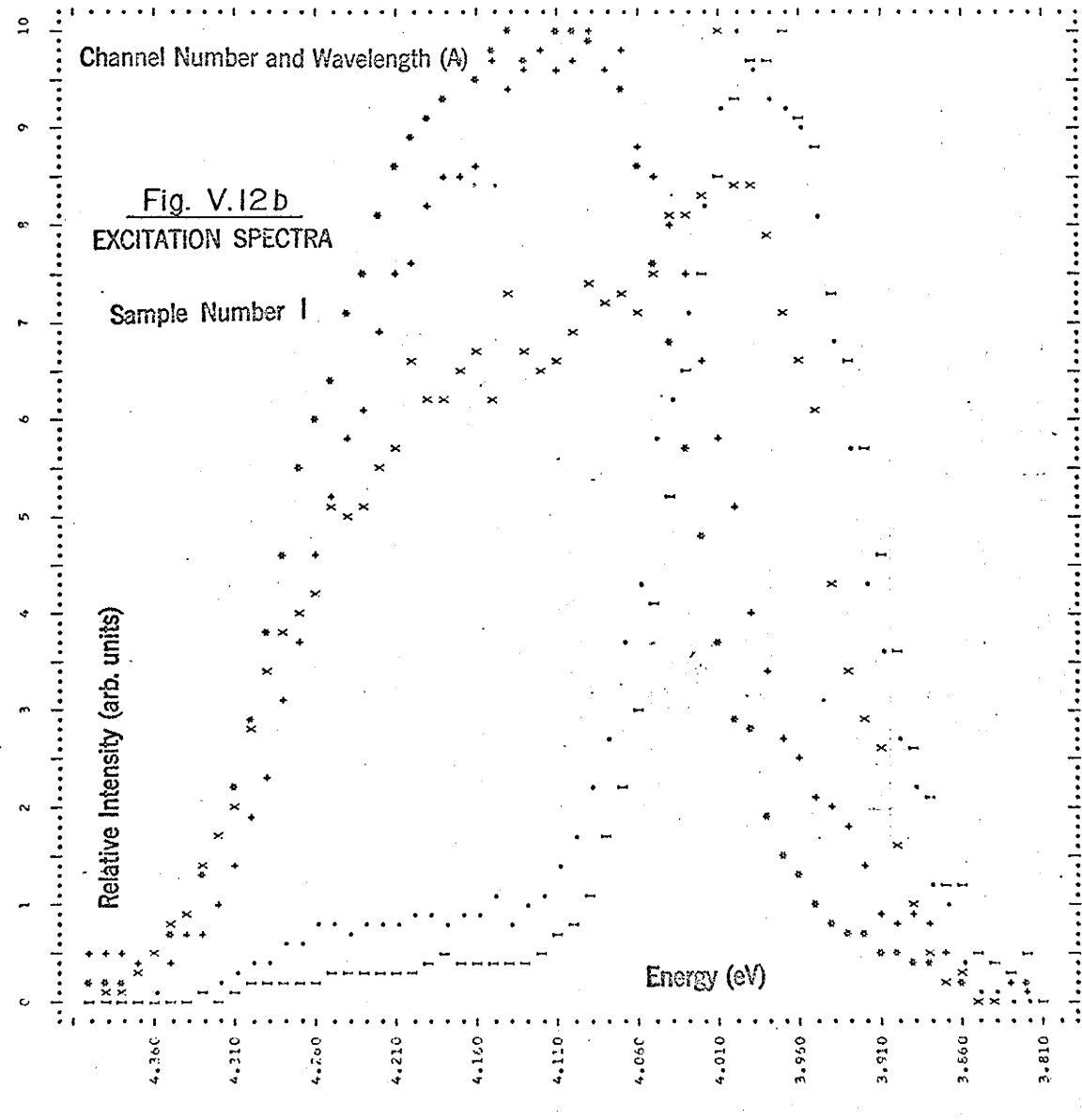
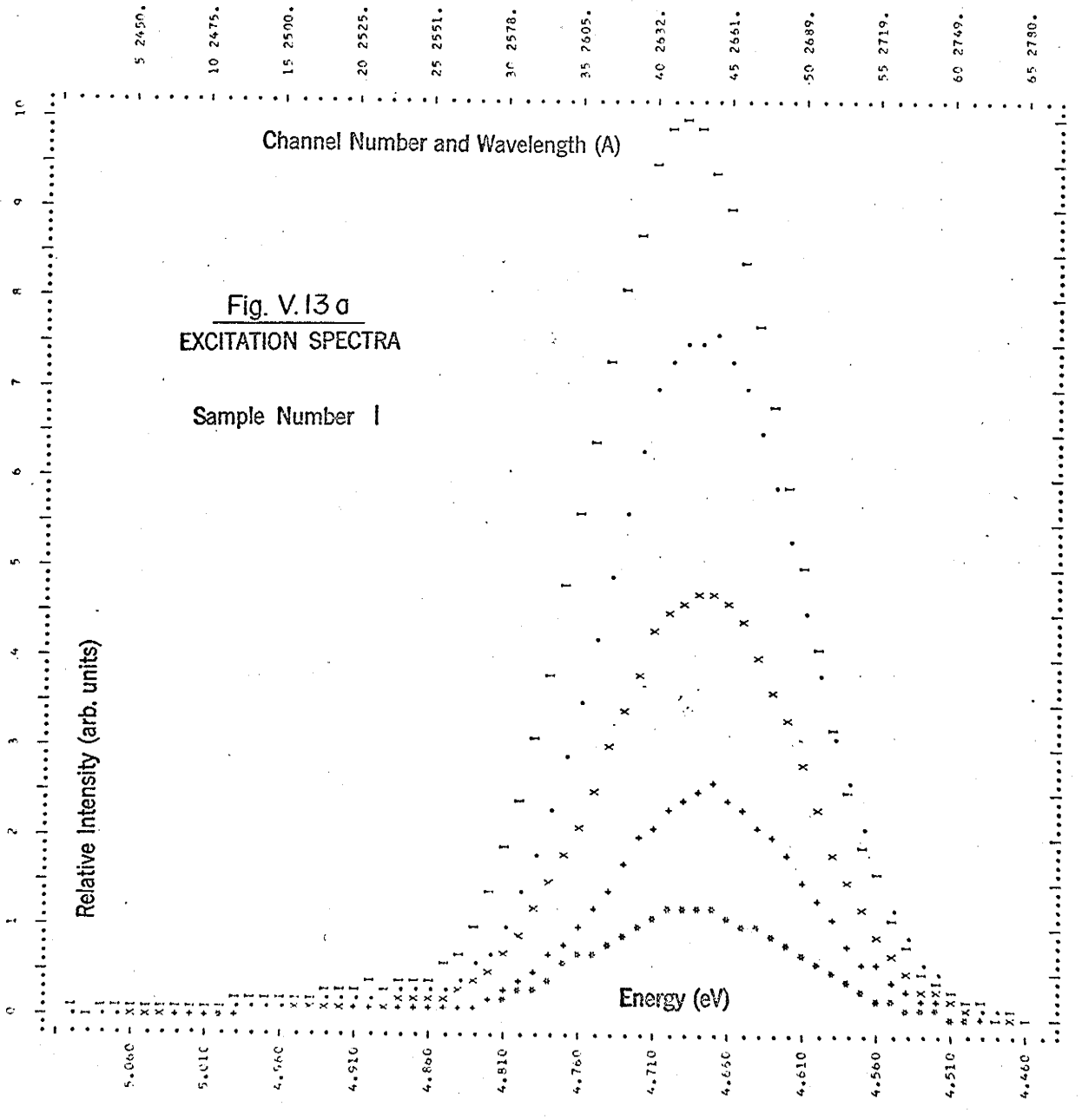


FIGURE 13A

PLOTTING INTERVAL - EVERY 1 POINT(S)
 GRAPH 1 (+) GRAPH 2 (+) GRAPH 3 (X) GRAPH 4 (.) GRAPH 5 (I)

EMISS/EXCIT ENERGY (E.V.) 3.59 3.65 3.70 3.76 3.81
 EMISS/EXCIT WAVELENGTH (A) 3450 3400 3350 3300 3250
 TEMPERATURE (LOG₁₀ K) 97. 97. 97. 97. 97.

DATA SCALED BUT NOT NORMALIZED



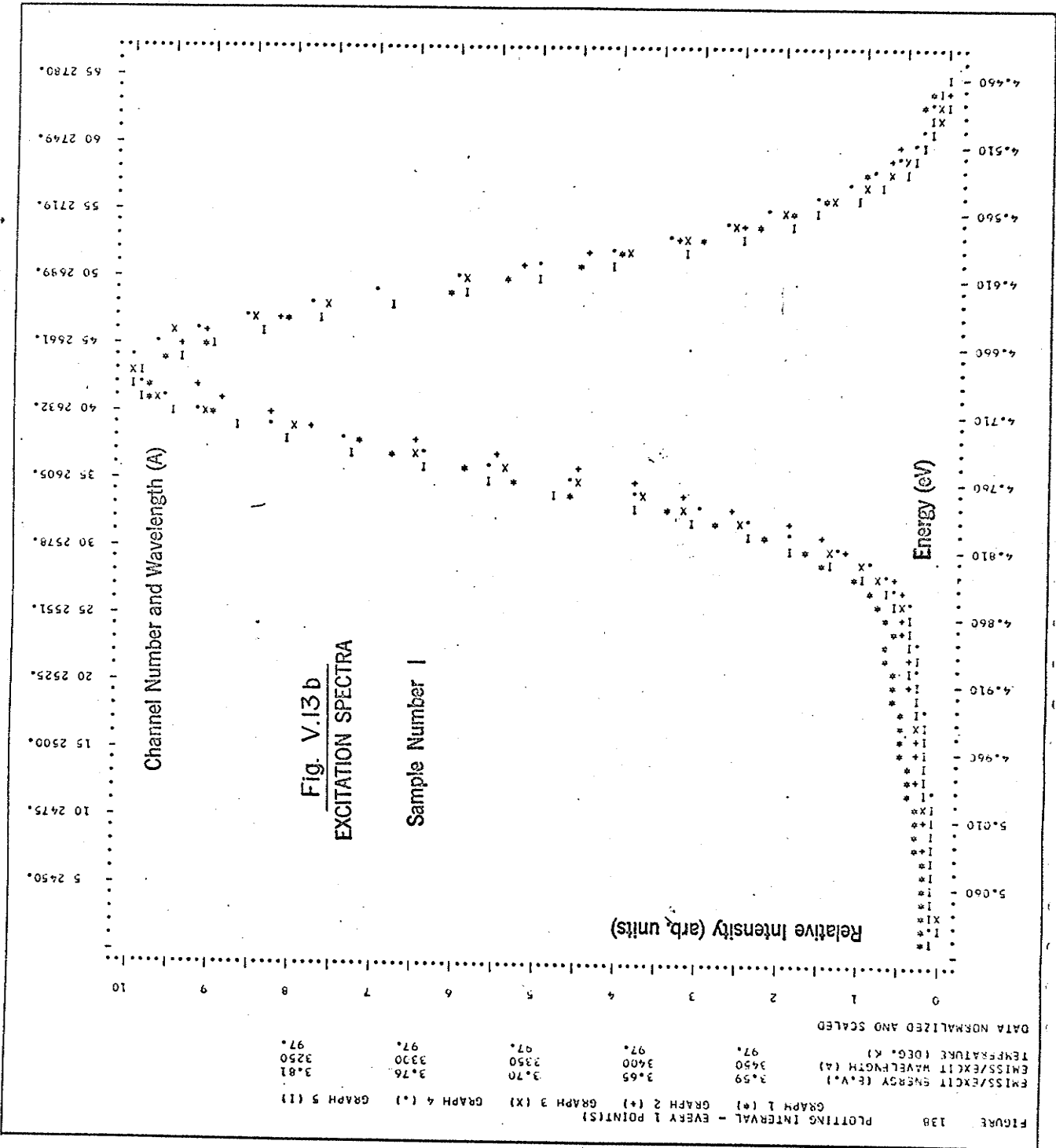
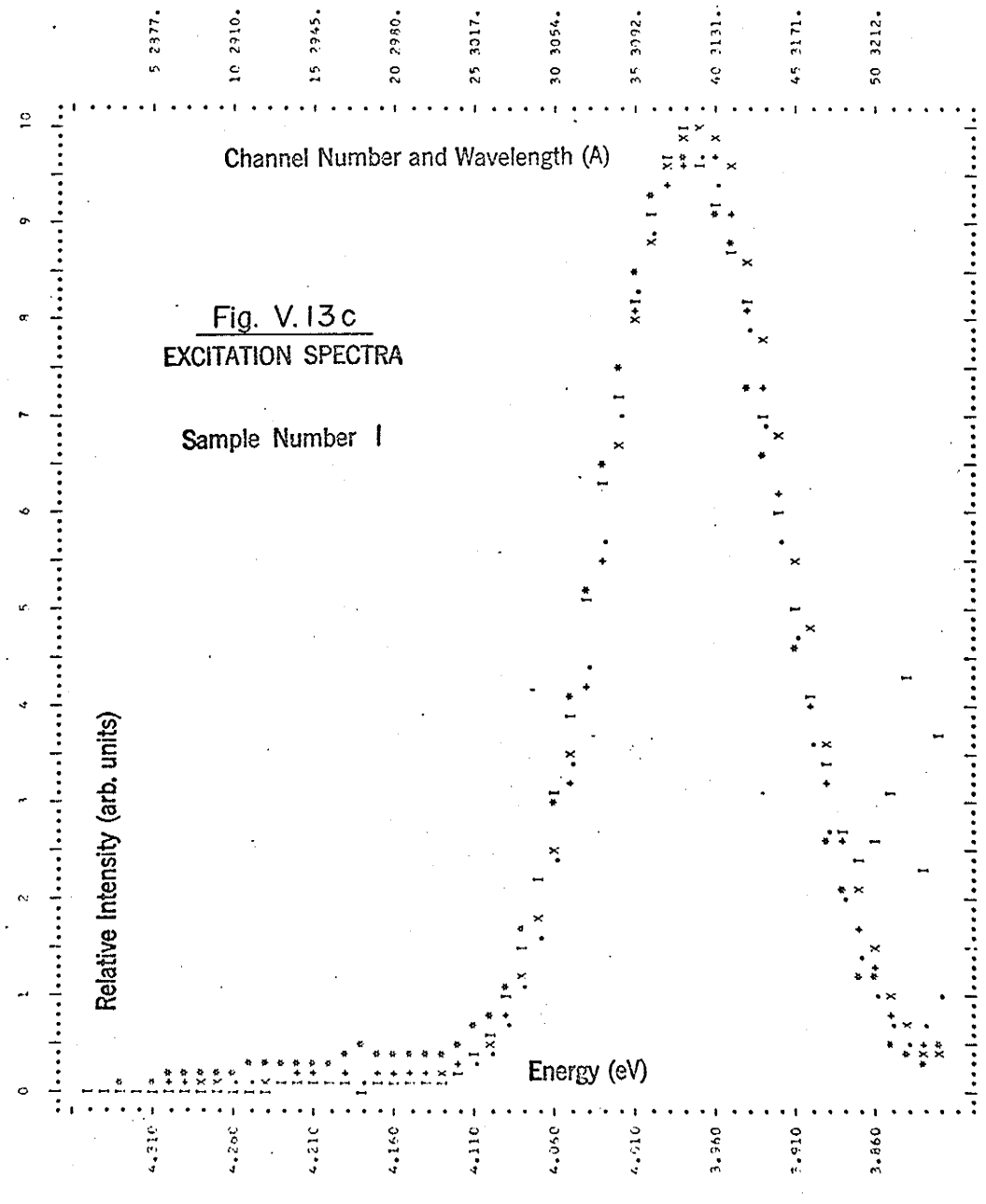


FIGURE 13C PLOTTING INTERVAL - EVERY 1 POINT(S)
 GRAPH 1 (*) GRAPH 2 (+) GRAPH 3 (X) GRAPH 4 (.) GRAPH 5 (I)

EMISS/EXCIT ENERGY (E.V.) 3.59 3.55 3.70 3.76 3.81
 EMISS/EXCIT WAVELENGTH (A) 3450 3400 3250 3300 3250
 TEMPERATURE (DEG. K) 97. 97. 97. 97. 97.

DATA NORMALIZED AND SCALED



(D) Room Temperature Excitation Spectra

Figures V.14 and V.15 show the excitation spectra of NaI(Tl) Sample #1 at room temperature. The selected emission energies range from 2.70 eV (4600 Å) to 3.65 eV (3400 Å), covering both the emission envelopes.

Excitation spectra characteristic of emissions within the low energy envelope are shown in Figure V.14. Two unsymmetrical excitation envelopes are seen, the smaller between 5.1 eV (2430 Å) and 4.4 eV (2820 Å) and the larger between 4.4 eV (2820 Å) and 3.7 eV (3350 Å). Both envelopes are considerably broader than their low temperature counterparts previously shown in Figures V.1 and V.2. As the emission energy increases, the height of the low energy A excitation band in Figure V.14 rises markedly, prior to a smaller decay. Its shape does not appear to change drastically.

Although the high energy excitation envelope of Figure V.14 indicates neither resolved bands nor pronounced shoulders, it is possible to infer internal structure from its change in shape as the emission energy varies. The high energy side of the envelope rises sharply and then falls only slightly, as did the A band. Thus by analogy with the low temperature data the presence of the monomer B and C bands under the high energy envelope is expected. The extreme low energy side of the envelope behaves differently in that after a sharp initial rise it falls almost to its original height. Since this change occurs to the low energy side of the position of the B'

band, it is again associated with a centre other than those due to the Tl^+ impurity.

In Figure V.15, as the emission energy increases, the broad A excitation band decreases slightly, and then remains steady whilst the narrower A' band rises on its low energy side, at 3.90 eV (3180 Å).

The broad high energy excitation envelope shows a small decay of both shoulders as the emission energy increases, together with the rise of the B' band at 4.58 eV (2710 Å).

In comparing the data taken at room temperature with that taken at liquid nitrogen temperature, the following points are evident:-

(1) The low temperature band positions are at higher energies than are their room temperature counterparts.

Band	Liq. N ₂ Temp.	Room Temp.
A	4.14 eV (2990 Å)	4.12 eV (3010 Å)
B	4.80 eV (2580 Å)	--
C	5.12 eV (2420 Å)	--
A'	3.98 eV (3120 Å)	3.90 eV (3180 Å)
B'	4.68 eV (2650 Å)	4.58 eV (2710 Å)

(2) The widths of the bands (full width at half maximum) are smaller at liquid nitrogen temperature than at room temperature.

Band	Liq. N ₂ Temp.	Room Temp.
A	0.26 eV	0.3 eV
B	0.3 eV	--
C	0.3 eV	--
A'	0.14 eV	0.19 eV
B'	0.16 eV	--

(3) Emissions that at low temperatures are excited only by the dimer bands are at room temperature excited by both dimer and monomer bands. Compare, for example, Figures V.3 and V.4 with Figure V.15.

FIGURE 14

PLOTTING INTERVAL - EVERY 2 POINT(S)

EMISS/EXCIT ENERGY (E.V.)	2.70	2.82	2.95	3.10	3.26
EMISS/EXCIT WAVELENGTH (A)	4600	4400	4200	4000	3800
TEMPERATURE (DEG. K)	296.	296.	296.	296.	296.

DATA SCALED OUT NOT NORMALIZED

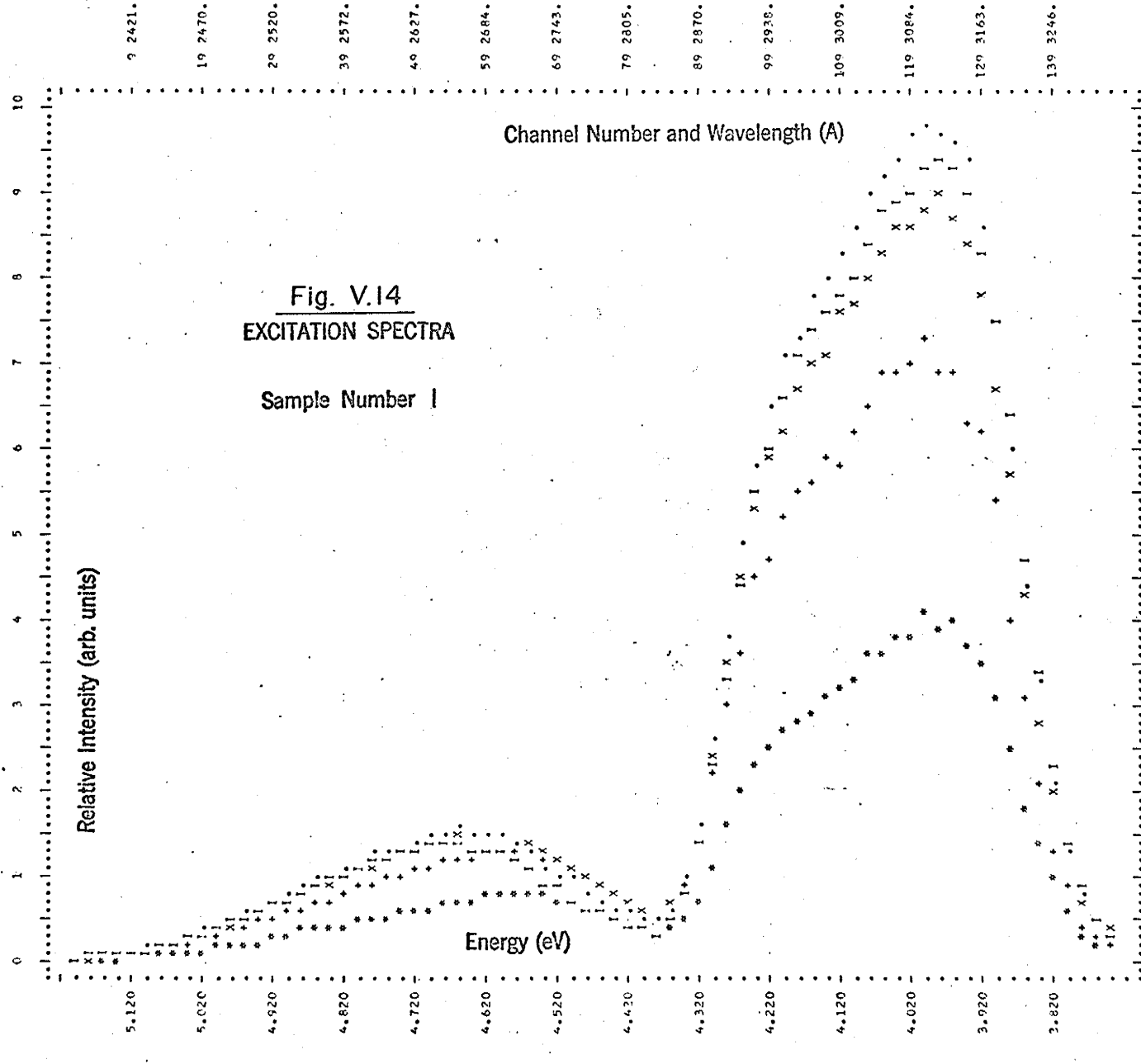


FIGURE 15 PULSING INTERVAL - EVERY 2 POINT(S)
 GRAPH 1 (*) GRAPH 2 (+) GRAPH 3 (X) GRAPH 4 (.) GRAPH 5 (I)

EMISS/EXCIT ENERGY (E.V.) 3.26 3.44 3.54 3.65
 EMISS/EXCIT WAVELENGTH (A) 9800 9600 9500 9400
 TEMPERATURE (CELS. C) 296. 296. 296. 296.
 DATA SCALED BUT NOT NORMALIZED

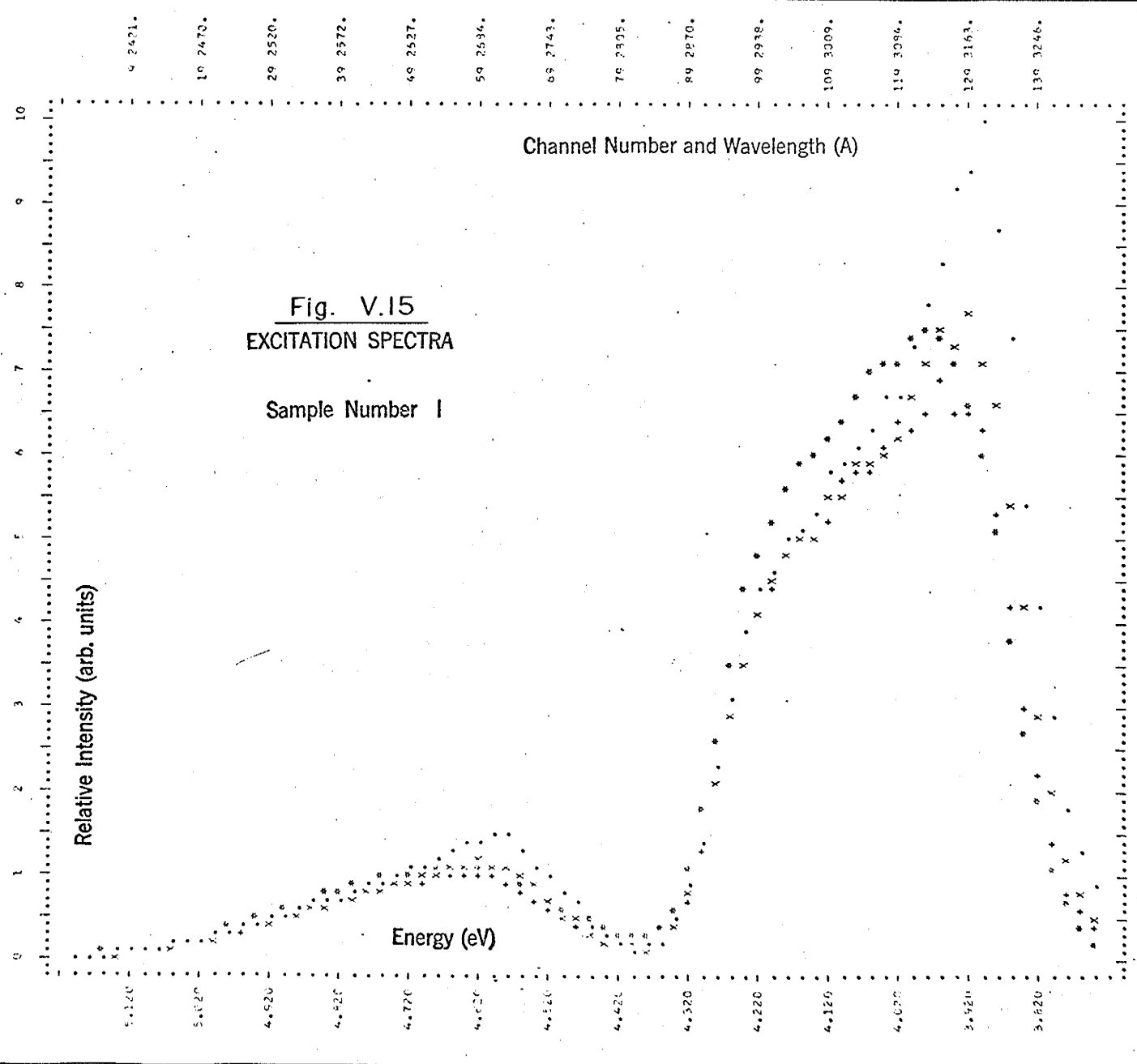


Fig. V.15
 EXCITATION SPECTRA
 Sample Number 1

(E) Room Temperature Excitation Envelope Shapes

The excitation curves of Figures V.14 and V.15 are redrawn in Figures V.16 and V.17. Parts (a) of each figure show the high energy envelopes normalized so that the largest peak fills the diagram, with the smaller peaks scaled accordingly. Parts (b) and (c) of each figure show the high and low energy envelopes respectively, each curve normalized to the same peak height. Figures V.16a and V.17a show more clearly than Figure V.14 the movement of the high energy excitation envelope towards higher energy as the emission energy varies from 2.70 eV (4600 Å) to 3.26 eV (3800 Å). The variation in height of the shoulders, suggested in Figure V.14, is confirmed in Figure V.16a. Figure V.16b shows that the envelope movement results from an increase in the B band and a decrease in the I' band to the low energy side of the B' band position at 4.58 eV (2710 Å). The low energy excitation envelope, however, indicates virtually no change in shape over this range of emissions.

For emissions at higher energies, between 3.26 eV (3800 Å) and 3.65 eV (3400 Å), the low energy excitation envelope changes shape quite drastically, as shown again in Figure V.17c. The A band progressively decays, whilst the A' band rises on its low energy side. For a similar range of emission energies, Figures V.17a and V.17b show the high energy excitation envelope becoming increasingly narrower

and moving towards lower energies, as the B and C bands decay and the B' band grows.

FIGURE 16A PLOTTING INTERVAL - EVERY 1 POINT(S)
 GRAPH 1 (+) GRAPH 2 (+) GRAPH 3 (X) GRAPH 4 (.I) GRAPH 5 (I)

EMISS/EXCIT ENERGY (eV, I) 2.70 2.82 2.95 3.10 3.26
 EMISS/EXCIT WAVELENGTH (A) 4600 4400 4200 4000 3900
 TEMPERATURE (DEG. K) 296. 296. 296. 296. 296.

DATA SCALED BUT NOT NORMALIZED

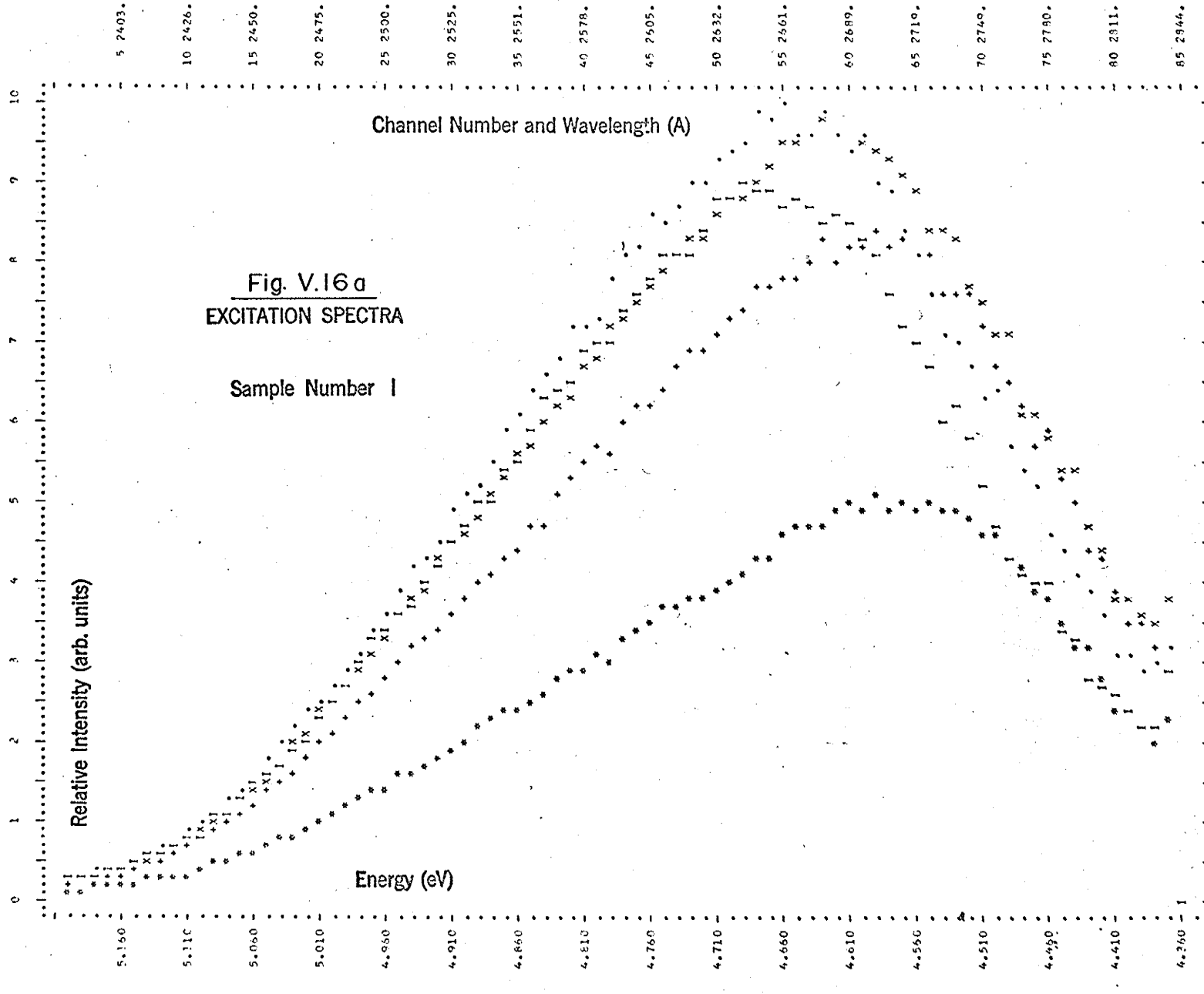
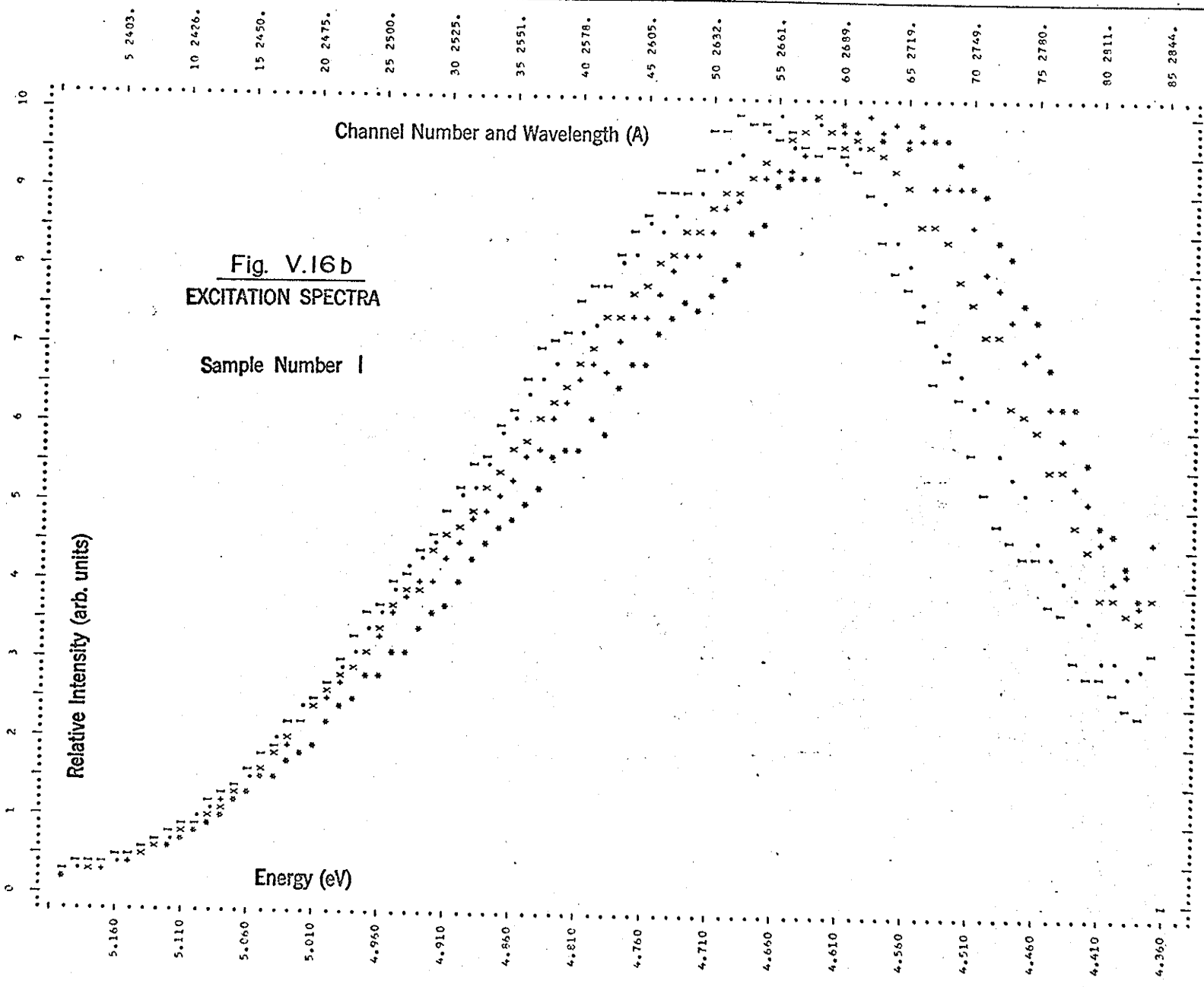


FIGURE 168 PLOTTING INTERVAL - EVERY 1 POINT(S)
 GRAPH 1 (*) GRAPH 2 (+) GRAPH 3 (X) GRAPH 4 (.) GRAPH 5 (I)

EMISS/EXCIT ENERGY (E.V.) 2.70 2.82 2.95 3.10 3.26
 EMISS/EXCIT WAVELENGTH (A) 4600 4400 4200 4000 3800
 TEMPERATURE (DEG. K) 296. 296. 296. 296. 296.

DATA NORMALIZED AND SCALED



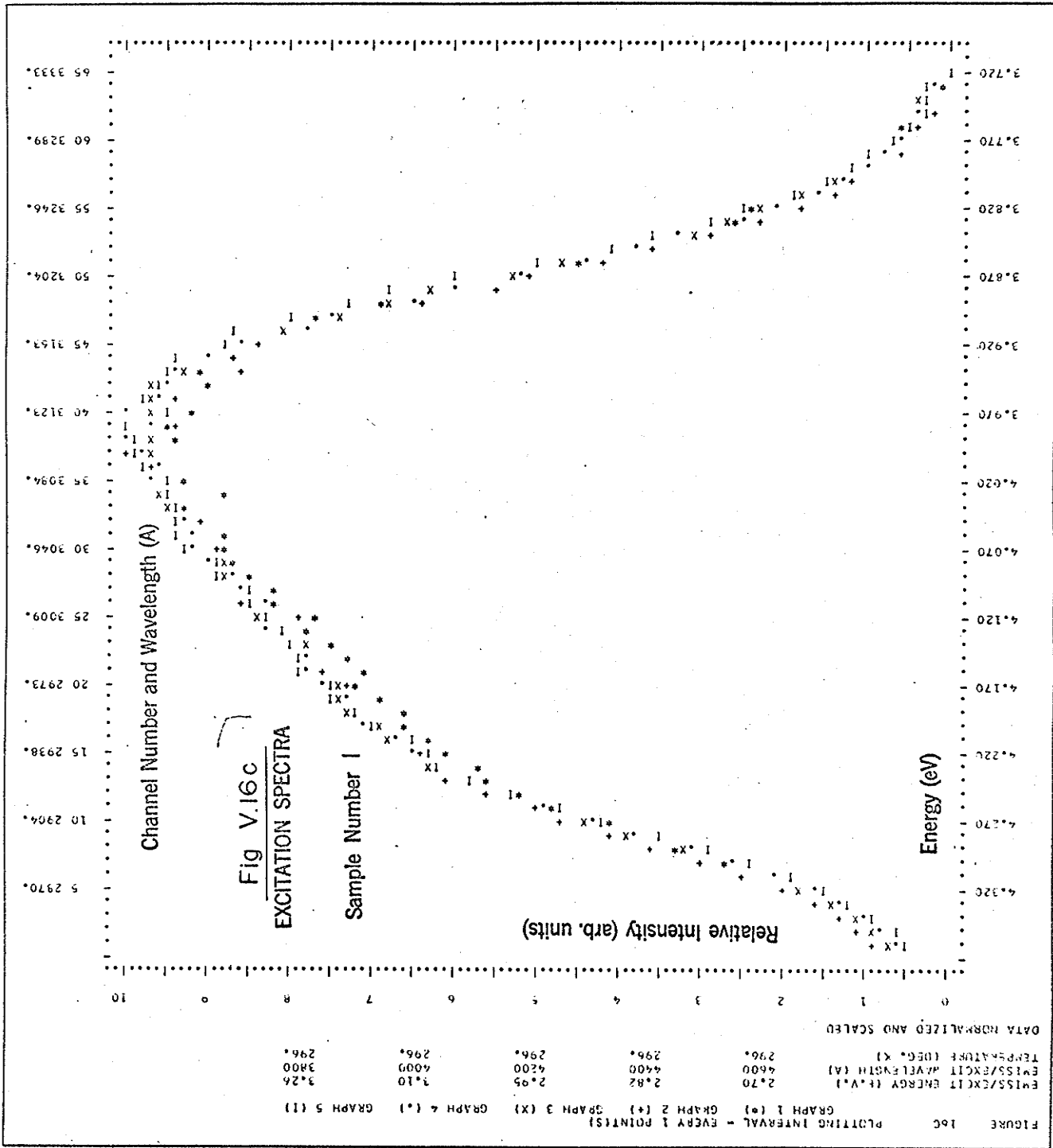
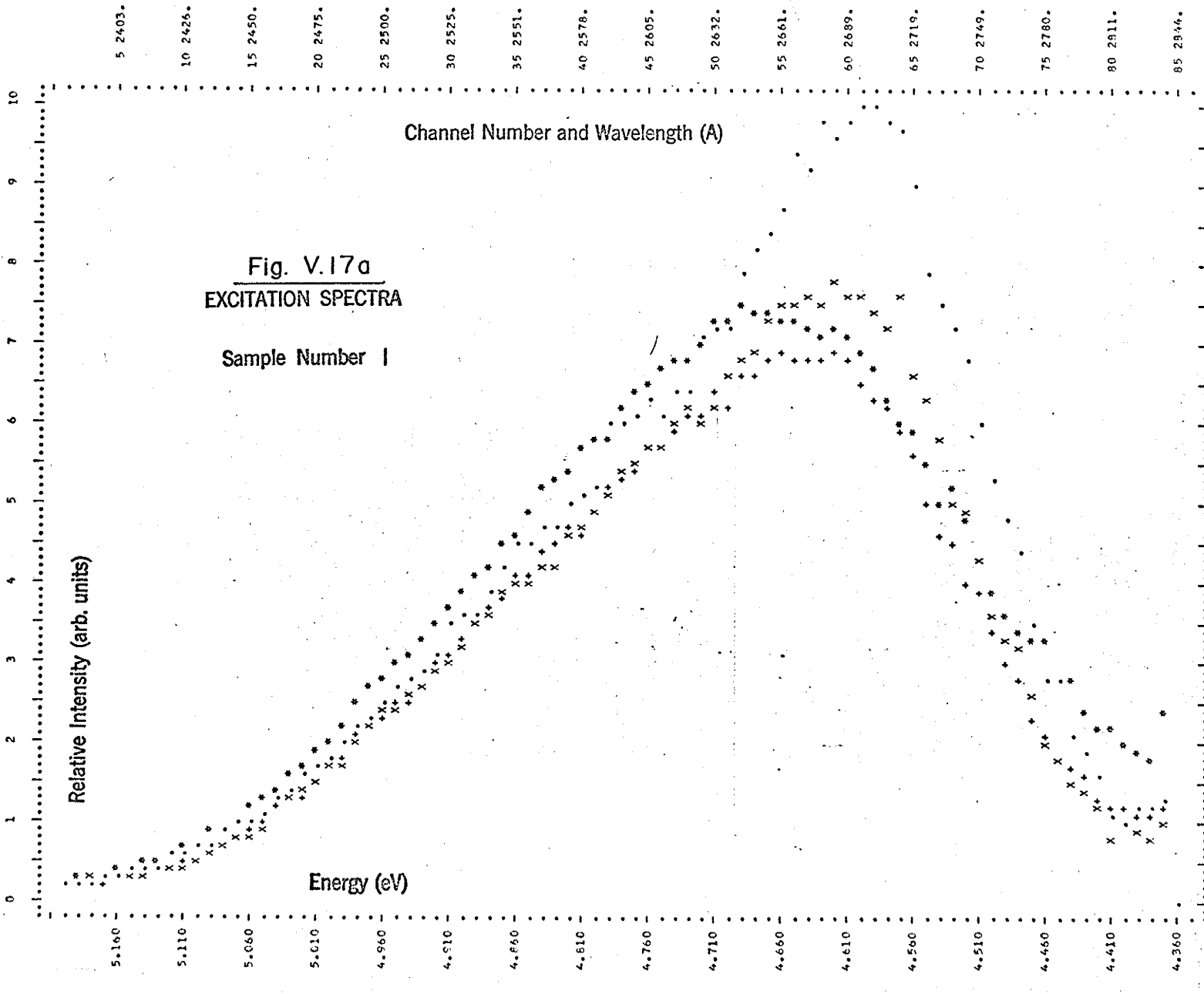
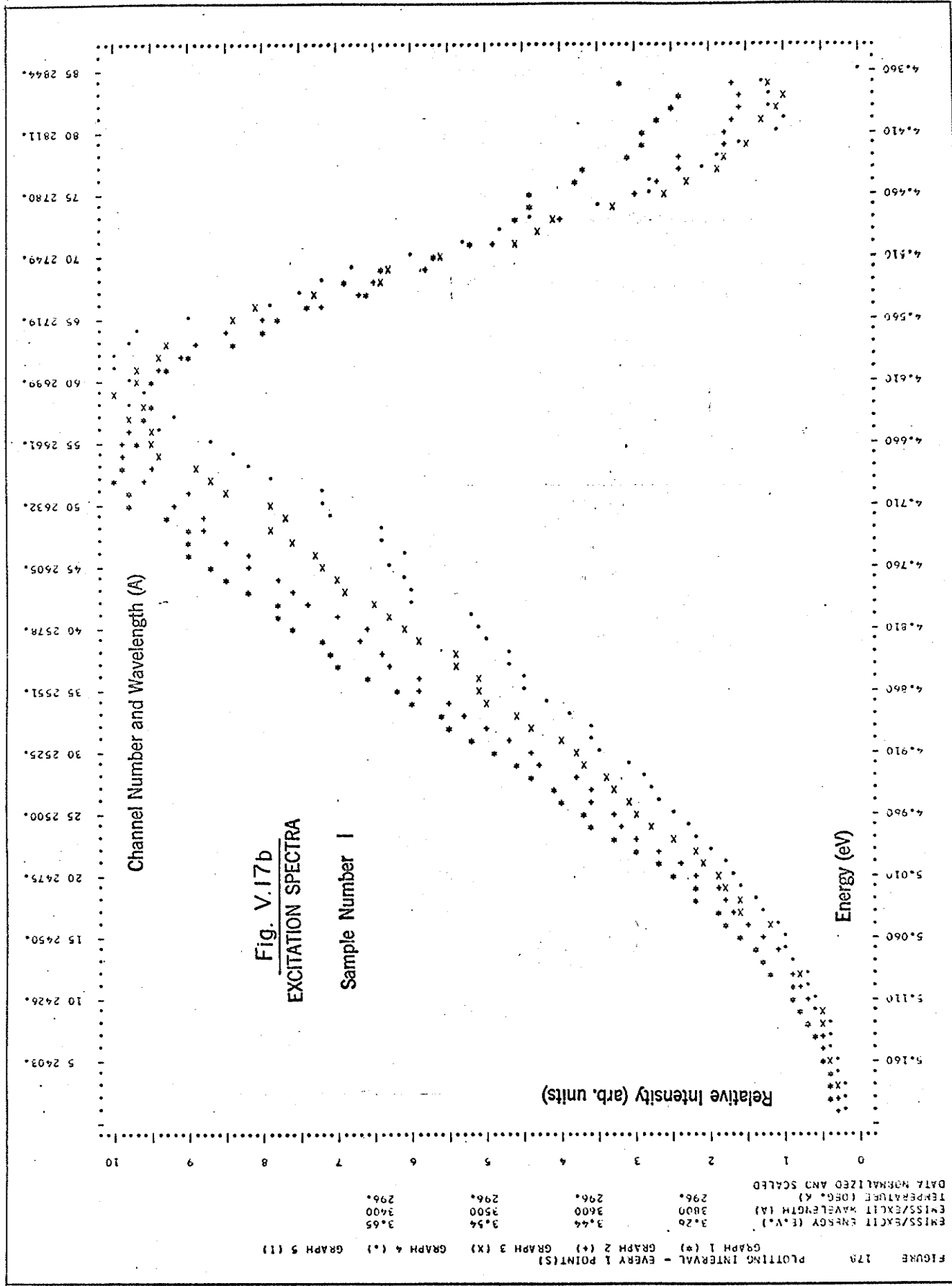


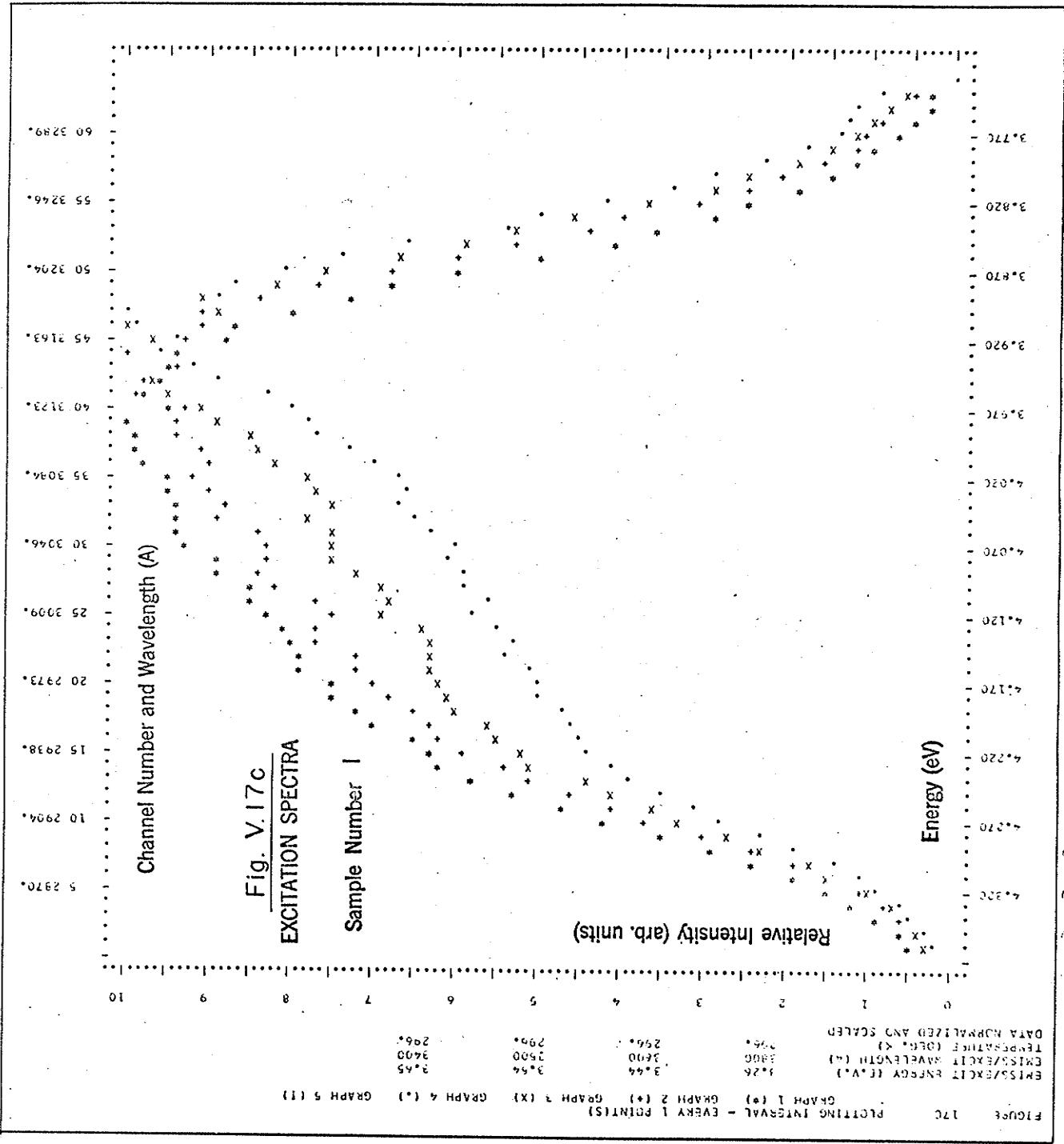
FIGURE 17A PLOTTING INTERVAL - EVERY 1 POINT(S)
 GRAPH 1 (*) GRAPH 2 (+) GRAPH 3 (X) GRAPH 4 (.) GRAPH 5 (I)

ENISS/EXCIT ENERGY (E.V.) 3.26
 ENISS/EXCIT WAVELENGTH (A) 3600
 TEMPERATURE (DEG. C) 296.
 DATA SCALED BUT NOT NORMALIZED

3.44 3.54 3.65
 3600 3500 3400
 296. 296. 296.







(F) Temperature Dependence of the Excitation Envelope

Figure V.18 shows the excitation spectrum that led to emission at 2.88 eV (4300 Å), at various temperatures of NaI(Tl) Sample #3. As expected, two excitation envelopes are seen, at about 4.1 eV (3020 Å) and 4.7 eV (2640 Å) respectively. Both move toward lower energies as the temperature rises, in accord with previously reported data: simultaneously, the peak heights of both envelopes increase up to about 213°K and then decay once more.

The detailed temperature variation of the full width at half maximum of the low energy A excitation band of Sample #3 is shown in Figure V.19, for emission at 2.88 eV (4300 Å). This emission energy was chosen since the excitation spectra indicate that the dimer centre plays little part in its excitation.

The extrapolated band width at absolute zero ($L(0)$) is 0.330 ± 0.005 eV. A straight line constructed to pass through the origin is asymptotic to the experimental curve, and its slope is 0.0226 ± 0.0004 eV $^{\circ}\text{K}^{-\frac{1}{2}}$. Thus from Equation III.29 the vibration frequency ν_g associated with the ground state is $\nu_g = (8.9 \pm 0.9) \times 10^{12}$ cycles/sec, and from Equation III.17 the mean number of vibrational quanta absorbed (\bar{s}) is 80 ± 20 .

Matsui (1967) performed a similar calculation for a NaI(Tl) sample containing 0.006 mole% of Tl^+ and obtained widely different results as below:-

$$L(0) = 0.155 \text{ eV}$$

$$\nu_g = 4.78 \times 10^{12} \text{ cycles/sec.}$$

$$s = 62$$

To the author's knowledge, the experimental curve from which the above results of Matsui were derived has not been published. Similar data related to the emission bands, however, suggests that the curve was defined by only three data points.

FIGURE 18 PULSING INTERVAL - FIVEEY 1 POINT(S)
 GRAPH 1 (+) GRAPH 2 (+) GRAPH 3 (X) GRAPH 4 (.) GRAPH 5 (I)

EMISS/FACIT ENERGY (E.V.)	2.88	2.88	2.88	2.88	2.88
EMISS/FACIT WAVELENGTH (μ)	4300	4300	4300	4300	4300
TEMPERATURE (DEG. K)	54.	151.	213.	250.	277.

DATA SCALED BUT NOT NORMALIZED

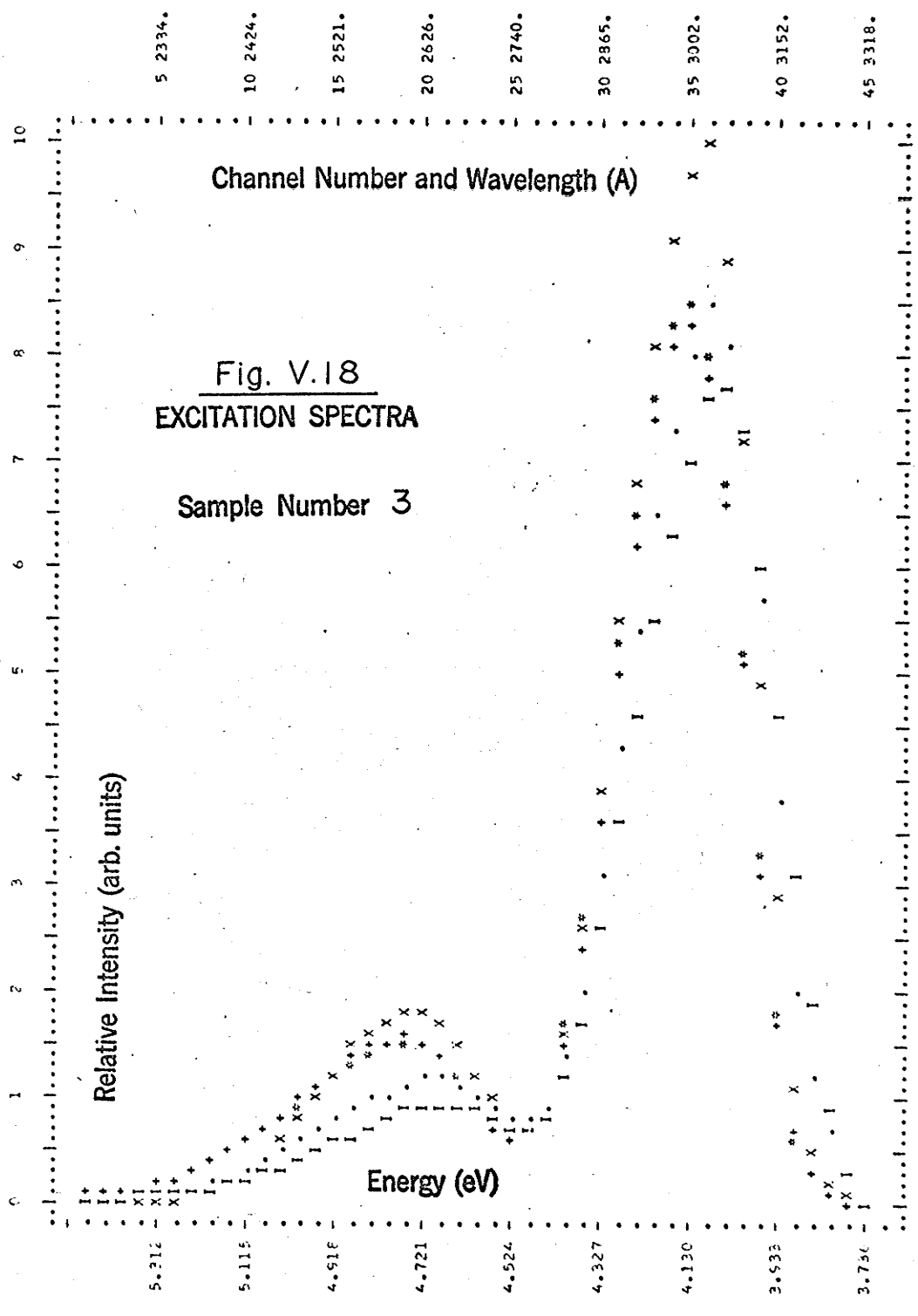
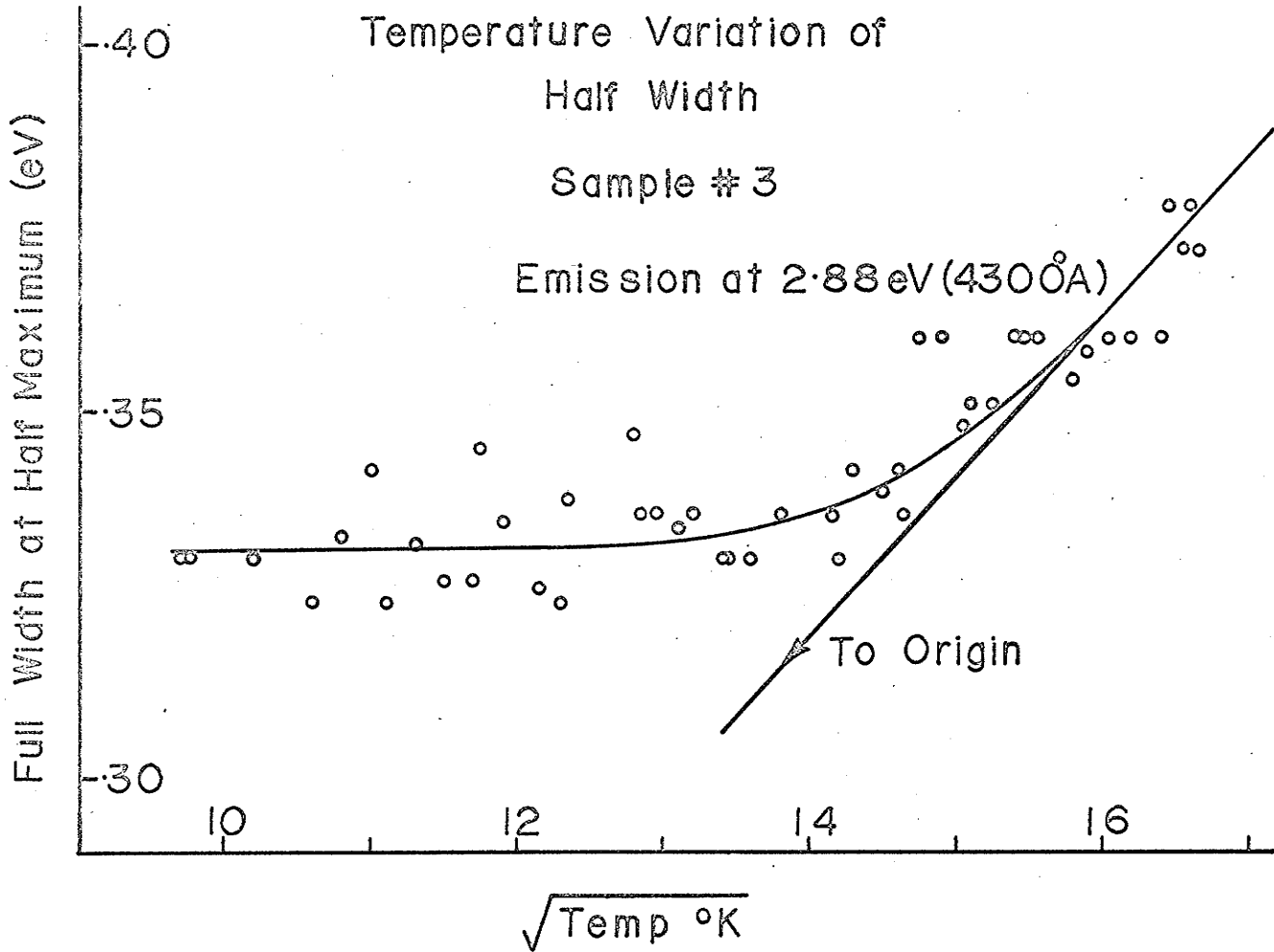


Fig.V.19



(G) Low Temperature Emission Spectra

Figures V.20 to V.24 show the emission spectra of NaI(Tl) Sample #1 at temperatures between 95° and 98° Kelvin, and excited by light of various wavelengths.

The extreme high energy peaks (marked T.P.) of Figure V.20 are not luminescent emission envelopes but transmission peaks, and are due to the light from the irradiation monochromator being scattered within, and transmitted through, the sample. The design of the crystal mount prevented direct scatter of the incident light into the analyser monochromator. Because of the nonuniform absorption of light in the region of 4.00 eV (3100 Å) by the crystal, the transmission peaks intensity in that region does not coincide with the quoted excitation wavelength.

Excitation at energies between 3.94 eV (3150 Å) and 4.13 eV (3000 Å), covering both the A' and A excitation bands, produces two broad and unsymmetrical emission envelopes (Figure V.20), the broader at about 2.88 eV (4300 Å) and the other at about 3.80 eV (3260 Å). As the excitation energy steps across the A' band and into the A band, the high energy emission envelope increases initially and then decreases, whilst the low energy emission envelope increases markedly and then remains steady.

Figure V.21 shows that for excitations within the A band, from 4.13 eV (3000 Å) to 4.35 eV (2850 Å), the high

energy emission envelope is all but absent, and the unsymmetrical low energy envelope decreases.

The behaviour of the high energy envelope shown in Figure V.22 for excitation in the range 4.35 eV (2850 Å) to 4.77 eV (2600 Å) is similar to that of Figure V.20 in that it too rises and then falls. As the excitation energy steps across the high energy part of the A band and across the B' band, the peak height of the low energy emission envelope at first decreases and then increases steadily, whilst the peak position moves from about 2.82 eV (4400 Å) to 2.88 eV (4300 Å). The peak movement and the asymmetry of the envelope together suggest the presence of another band in the left hand side of the low energy envelope. There is also evidence for an emission band at about 3.28 eV (3780 Å), but its intensity is insufficient to produce all the broadening of the low energy emission envelope.

Figures V.23 and V.24, for excitation in the range 4.77 eV (2600 Å) to 5.64 eV (2200 Å) spanning the B and C bands, show the rapid decay of the high energy emission, and the steady decrease of the low energy envelope with an apparent slight shift towards higher energy in its peak position. The 3.31 eV (3750 Å) band is not fully resolved from the main low energy envelope.

In Figures V.25 to V.29 are shown the emission spectra for a different sample (NaI(Tl) Sample #2). Again the crystal

temperature was between 95° and 98° K., and the excitation was by light at the indicated wavelengths.

Although the spectra of the two samples agree in general outline, the following differences are noted:-

(i) The ratios of the heights of the high to low energy emission envelopes are different for the two samples, as may be seen by comparing Figure V.25 with Figure V.20, Figures V.27 and V.28 with Figure V.22, and Figure V.29 with Figure V.23.

(ii) The high energy emission envelopes of Figures V.25, V.27, and V.29 appear to be comprised not of single bands, but of several overlapping and unresolved bands. The arrows indicate fine structure peaks that occur on more than one graph.

(iii) The low energy emission envelope for Sample #1 is distorted from the pure Gaussian on its high energy side more than is the corresponding curve for Sample #2. This may be seen by comparing Figure V.26 with Figure V.21, Figures V.27 and V.28 with Figure V.22, and Figure V.29 with Figure V.23.

In Figures V.27 and V.28 the small emission band at 3.31 eV (3750 Å) is again noted.

The previous low temperature emission data shows that the high energy emission envelope is excited only by light within the A' and B' bands, and is thus associated with the $(\text{Tl}^+)_2$ dimer centre. The low energy emission envelope, however, is excited by light within the bands of both the monomer and dimer centres.

A direct comparison of three samples used is afforded by Figure V.30, showing the emission spectrum of each crystal at low temperature and excited by light at 4.68 eV (2650 Å) from the B' band. The three curves are normalized at the peak height of the low energy envelope, and graphically show that the intensity ratio of the high to low energy envelopes varies among the samples. This most probably is explained by the difference in dimer/monomer ratios, which results from a variation in Tl^+ concentration among the three samples. Returning to Figures V.27 and V.28, the small emission band at 3.31 eV (3750 Å) is again seen under excitation from the I' band on the low energy side of the B' excitation band. Thus, in accord with the excitation data, the 3.31 eV band is associated with emission from a centre unrelated to the monomer or dimer centres.

Van Sciver (1960), in studying the luminescent and reflection spectra of NaI crystals grown under various conditions, observed an emission band at 3.31 eV (3750 Å) which he attributed to a stoichiometric excess of I_2 . This

emission was excited at 83°K. by two bands at 4.85 eV (2560 Å) and 5.47 eV (2270 Å), both of which lie on the high energy side of the I' excitation band. Also, the emission was absent in crystals doped with Tl⁺: thus it seems unlikely that the 3.31 eV emission and I' excitation band seen in the present study are due to a stoichiometric excess of I₂.

Another possible explanation for the 3.31 eV (3750 Å) emission band, is that it results from a centre consisting of several Tl⁺ ions in near neighbour positions; that is, an aggregate centre. Such a centre could explain an excitation band on the low energy side of the B' band, but would require the presence of an additional band on the low energy side of the A' band. An "aggregate A excitation band" was not observed; neither was any emission at 3.31 eV seen when samples were excited at energies below the B' band.

Further, since aggregate centres would occur predominantly at high Tl⁺ concentrations, the pronounced 3.31 eV band of Sample #3 in Figure V.30 would require that Sample #3 have a higher Tl⁺ concentration than the other two samples. Such is not the case, as seen from the relative heights of the high energy dimer emission bands. It is concluded that the 3.31 eV (3750 Å) emission band results from a centre that is presently unidentified.

FIGURE 20 PLOTTING INTERVAL - EVERY 2 POINT(S)
 GRAPH 1 (*) GRAPH 2 (+) GRAPH 3 (X) GRAPH 4 (.) GRAPH 5 (I)

EMISS/EXCIT ENERGY (E.V.)	3.94	4.00	4.06	4.13
EMISS/EXCIT WAVELENGTH (Å)	3150	3100	3050	3000
TEMPERATURE (DEG. K)	98.	98.	98.	98.

DATA SCALED BUT NOT NORMALIZED

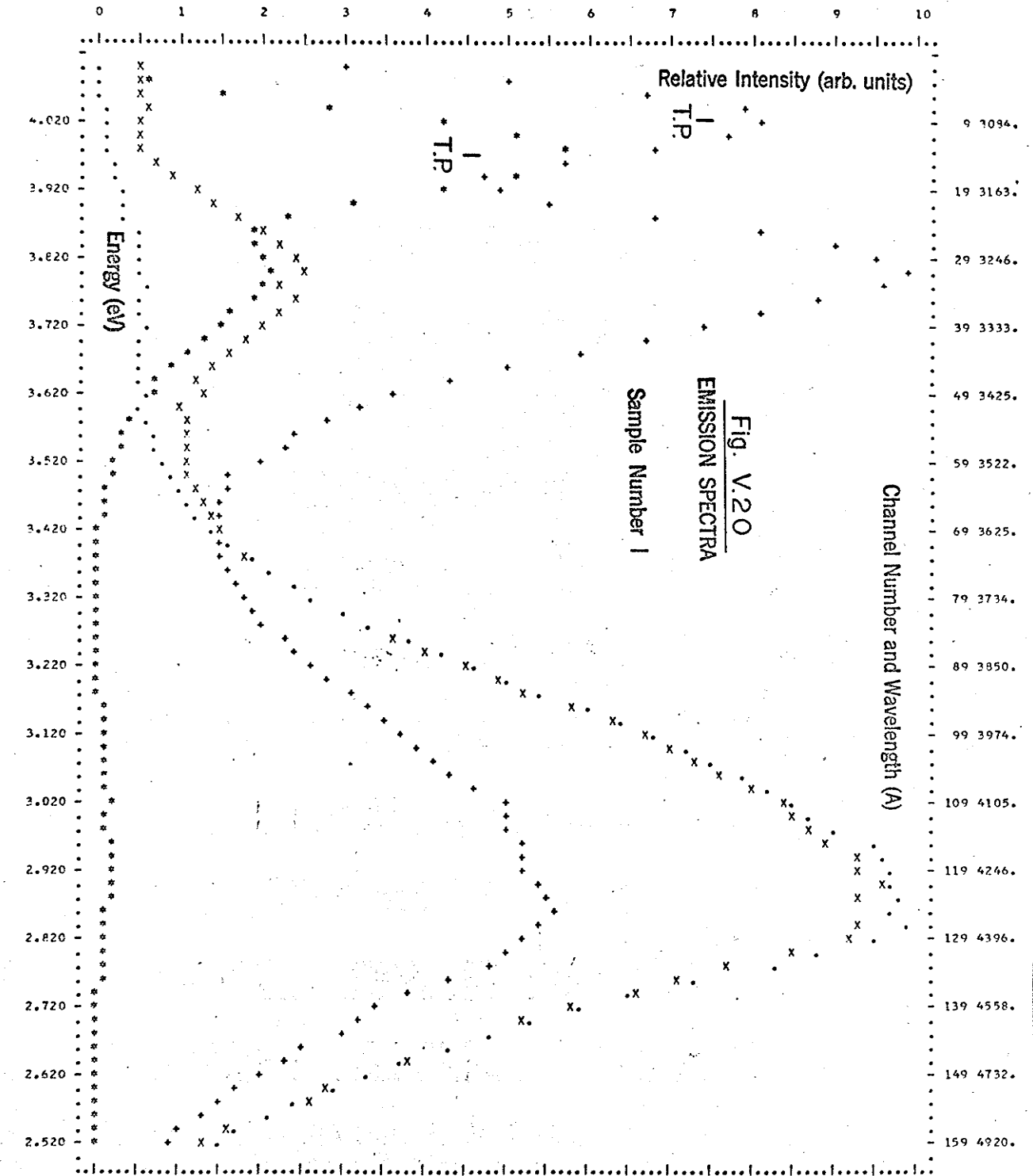


FIGURE 21 PLOTTING INTERVAL - EVERY 2 POINT(S)
 GRAPH 1 (*) GRAPH 2 (+) GRAPH 3 (X) GRAPH 4 (.) GRAPH 5 (I)

EMISS/EXCIT ENERGY (E.V.) 4.13 4.20 4.28 4.35
 EMISS/EXCIT WAVELENGTH (A) 3000 2950 2900 2850
 TEMPERATURE (DEG. K) 98. 98. 98. 98.
 DATA SCALED BUT NOT NORMALIZED

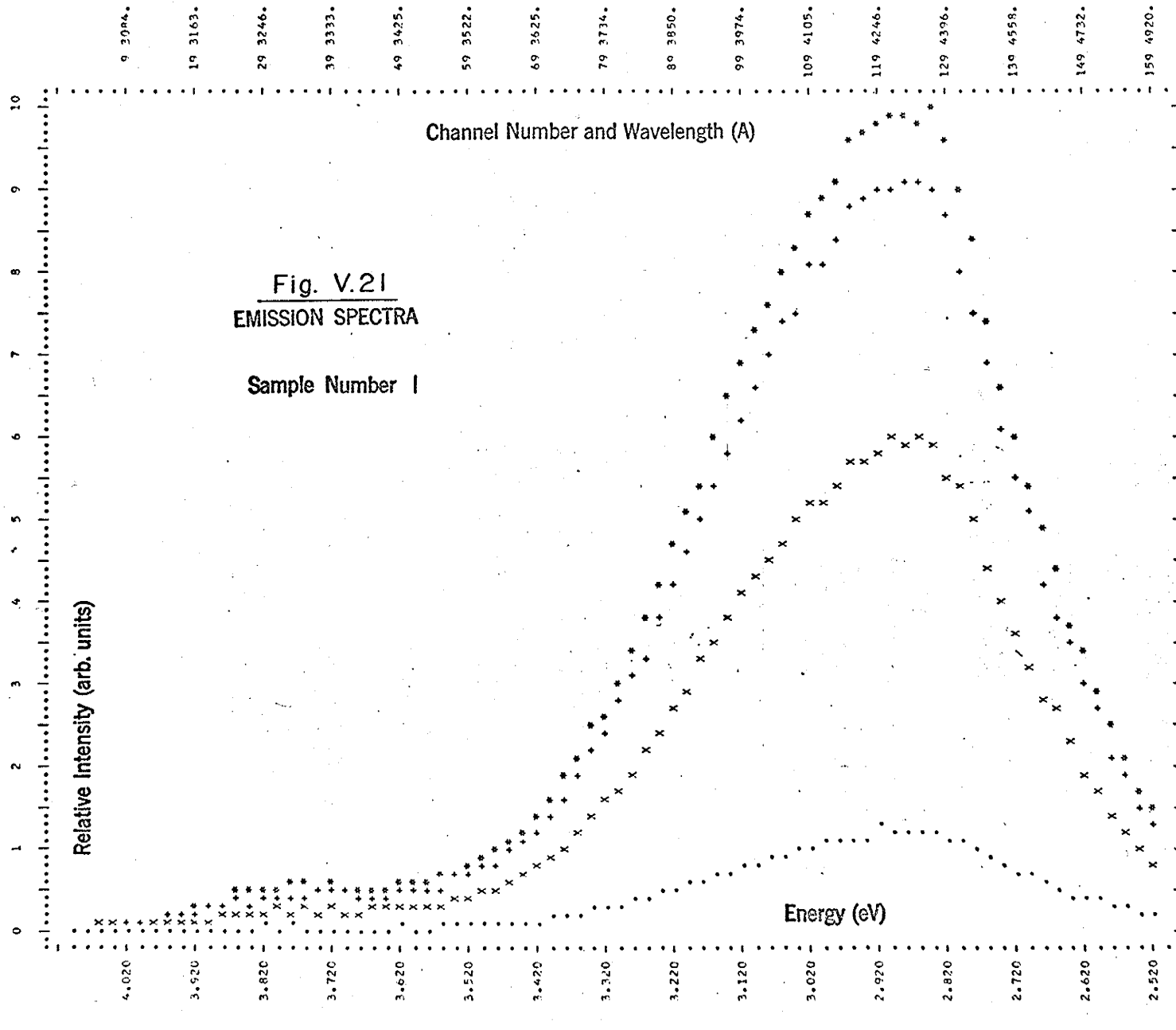


FIGURE 22 PLOTTING INTERVAL - EVERY 2 POINT(S)

GRAPH 1 (*)	GRAPH 2 (+)	GRAPH 3 (X)	GRAPH 4 (o)	GRAPH 5 (I)
4.35	4.51	4.59	4.68	4.77
2850	2750	2700	2650	2600
98.	98.	98.	98.	98.

DATA SCALED BUT NOT NORMALIZED

